GEORG-AUGUST-UNIVERSITÄT
GÖTTINGEN

Fakultät für
Physik

Master's Thesis

Charakterisierung von Low Gain Avalanche Detektoren

Characterisation of Low Gain Avalanche Detectors

prepared by

Marike Schwickardi

from Höxter

at the II. Physikalischen Institut

Thesis number: II.Physik-UniGö-MSc-2019/06

Thesis period: 15th April 2019 until 15th October 2019

First referee: Prof. Dr. Arnulf Quadt

Second referee: Priv.Doz. Dr. Jörn Große-Knetter

Zusammenfassung

Der Large Hadron Collider (LHC) der europäischen Organisation für Teilchenphysik in Genf (CERN) wird seinen Betrieb in den Jahren 2024-2026 unterbrechen, um zu einer höheren Luminosität (HL-LHC) aufgerüstet zu werden, damit zukünftig Proton-Proton-Kollisionen mit eine Schwerpunktsenergie von $\sqrt{s} = 14$ TeV bei einer Luminosität von $5 - 7 \cdot 10^{34}$ cm^{-2}s^{-1} erreicht werden. ATLAS, eines der beiden Allzweckexperimente am LHC, muss aufgerüstet werden, um den neuen Anforderungen der größeren Luminosität gewachsen zu sein. Unter anderem ist das ATLAS-Upgrade geplant, um den High Granularity Timing Detector (HGTD) einzuführen, der Ankunftszeit-Informationen von Tracks und Vertices liefern soll.

In dieser Arbeit wurde die neuartige Siliziumdetektortechnologie der Low Gain Avalanche Detectors (LGAD) für den HGTD untersucht. LGADs sind Siliziumsensoren mit einer integrierten Ladungsmultiplikationsschicht, die eine Verstärkung von typischerweise 10 bis 50 bieten. Aufgrund der Kombination aus hohem Signal-Rausch-Verhältnis und kurzer Signalanstiegszeit bieten dünne LGADs eine gute Zeitauflösungen. LGADs mit einer aktiven Dicke von etwa 50 µm wurden bei Hamamatsu Photonics hergestellt. Ihr Leckstrom, ihre gesammelte Ladung und der Abstand zwischen den aktiven pads ($IP_{50\%}$) wurden für zwei verschiedene Multiplikationsschicht-Implantationsdosen untersucht, hier bezeichnet als “Typ 3.1“ und “Typ 3.2“ sowie vor und nach Bestrahlung mit Neutronen von $1.5 \cdot 10^{15}$ $n_{eq}cm^{-2}$. Durch IV-Charakterisierung wurden niedrige Ströme pro Pad im Sub-nA-Bereich für nicht bestrahlte Sensoren und Ströme unter 5 µA nach Bestrahlung gemessen, welche die HGTD-Anforderungen erfüllen. Zusätzlich wurde eine gute Homogenität über 15×15 Matrizen in Bezug auf Strompegel und Durchbruchspannung gemessen und eine gute Ausbeute über alle 15×15 Matrizen vom “Typ 3.1“ und “Typ 3.2“ erhalten. Die Verstärkung zeigte die erwartete Abnahme bei einer festen Spannung für eine höhere Fluenz aufgrund von Akzeptorentfernung in der Multiplikationsschicht. Für die Sensoren vom “Typ 3.1“ beträgt die Verstärkung 5 und für den “Typ 3.2“ beträgt sie 15, bei 100 V. Für die bestrahlten Sensoren vom “Typ 3.2“ zeigt die Verstärkung die erwartete Abnahme aufgrund niedrigerer Akzeptorkonzentrationen in der Multiplikationsschicht auf etwa 4 bei 450 V. Die gemessenen $IP_{50\%}$-Werte liegen um 45 µm über den vom Hersteller für die unbestrahlten Sensoren “Typ 3.1“ und “Typ 3.2“ angegebenen Nennwerten. Der niedrigste gemessene Wert beträgt für beide etwa 80 µm, was einem Füllfaktor von 88,5% entspricht. Nach Bestrahlung sinkt die $IP_{50\%}$ auf 40 µm bei 350 V.

Abstract

The Large Hadron Collider (LHC) at the European Organization for Particle Physics (CERN), Geneva, will interrupt its operation in 2023 to be upgraded to high luminosity (HL-LHC) and provide proton-proton collisions with a centre of mass energy of $\sqrt{s} = 14$ TeV at a luminosity of $5 - 7 \cdot 10^{34}$ cm^{-2}s^{-1}. ATLAS, one of the two general-purpose experiments at the LHC, will have to be upgraded to meet the new requirements given by the larger luminosity. Among other things, the ATLAS upgrade is planned to introduce the High Granularity Timing Detector (HGTD) that will provide timing information of tracks and vertices.

In this thesis, the novel Silicon detector technology of Low Gain Avalanche Detectors (LGAD) for HGTD was investigated. LGADs are Silicon sensors with an integrated charge multiplication layer that provide a gain of typically 10 to 50. Due to the combination of high signal-to-noise ratio and short signal rise time, thin LGADs provide good time resolution. LGADs with an active thickness of about 50 µm were manufactured by Hamamatsu Photonics. Their leakage current, accumulated charge and distance between the active pads ($IP_{50\%}$) were investigated for two different multiplication-layer implantation doses, here referred to as "Type 3.1" and "Type 3.2" and before and after irradiation with neutrons of $1.5 \cdot 10^{15}$ $n_{eq}cm^{-2}$. IV characterization measured low currents per pad in the sub-nA range for unirradiated sensors and currents below 5 µA after irradiation that meet HGTD requirements. Besides, good homogeneity over 15×15 arrays was measured in terms of current level and breakdown voltage, and a good yield was obtained over all 15×15 arrays of "Type 3.1" and "Type 3.2". The gain showed the expected decrease at a fixed voltage for a higher fluence due to acceptor removal in the multiplication layer. For the sensors of "Type 3.1", the gain is five and for the "Type 3.1" it is 15, at 100 V. For the irradiated sensors of "Type 3.2", the gain shows the expected decrease due to lower acceptor concentrations in the multiplication layer to about four at 450 V. The measured $IP_{50\%}$ values are around 45 µm about that of the manufacturer for the unirradiated sensors "Type 3.1" and "Type 3.2" specified denominations. The lowest measured value for both is about 80 µm, which corresponds to a fill factor of 88.5 %. After irradiation, the $IP_{50\%}$ drops to 40 µm at 350 V.

Contents

Terminologies

Abbreviation	**Meaning**
CERN	European Particle Research Center
LHC	Large Hadron Colider
HGTD	High Granularity Timing Detector
HL-LHC	High Luminosity LHC
LGAD	Low Gain Avalanche Detector
IV	Current-Voltage
TCT	Transient Current Technique
HPK	Hamamatsu Photonics
CNM	Centro Nacional de Microelectrónica
SM	Standard Model of Particle Physics
QFT	Quantum Field Theory
LEP	Large Electron-Positron Colider
PS	Proton Synchrotron
SPS	Super Proton Synchrotron
ID	Inner Detector
IBL	Insertable B-Layer
SCT	Semiconductor Tracker
TRT	Transition Radiation Tracker
EM	Electromagnetic
ITk	Inner Tracker
MIP	Minimum-Ionising Particle
e-h pair	Electron-Hole pair
IP	Inter Pad Gap
SE	Slim Edge
SNR	Signal to Noise Ration
UBM	Under Bump Metallisation
1D	One Dimensional
2D	Two Dimensional

Particles

Abbreviation	Particle
H	Higgs Boson
γ	Photon
W	Charged Boson of the Electroweak Force
Z	Neutral Boson of the Electroweak Force
g	Gluon
l	Lepton
e	Electron
μ	Muon
τ	Tau Lepton
ν	Neutrino
q	Quark
t	Top Quark
b	Bottom Quark
c	Charm Quark
s	Strange Quark
u	Up Quark
d	Down Quark

1 Introduction

Particle physics aims at explaining the fundamental particles in Nature and their interactions. The Standard Model of Particle Physics, which is presented in Chapter 2, describes all known elementary particles and three of the four fundamental interactions and is one of the most successful theories in science that explains the behaviour of the known fundamental particles. While it is a very successful and thoroughly tested description of particle physics and even further substantiated by the discovery of the Higgs Boson [1–3], it still does not describe all effects that are observed. Other theories aim at filling these gaps, but ultimately experimental validations are required to select and test viable extensions or alternatives to the Standard Model. For those tests of the Standard Model, the Large Hadron Collider (Lhc) at Cern, the European Organisation for Nuclear Research, was built [4]. It continues to define the frontier of particle physics by reaching unprecedented energies and interaction rates, therefore allowing the experiments to explore new regions of physics. One of the experiments located at the Lhc is the Atlas detector, which is described in Chapter 3. The innermost part of the Atlas detector, the Pixel Detector, provides high precision tracking required for momentum and vertex measurements close to the interaction point. It consists of semiconductor pixel detector modules, which are explained in Chapter 4.

The High Granularity Timing Detector (HGTD) [5], described in Chapter 3, is a proposed sub-detector system for the Atlas Experiment. It is planned to be installed inside the Atlas Experiment before the start of the High Luminosity Lhc (HL-Lhc) in 2024, which will increase the number of proton-proton collisions per time unit by a factor of five. In order to build the HGTD, Low Gain Avalanche Detectors (LGAD) were selected, which are described in Chapter 5. In this thesis, for the characterisation of the LGAD sensors, laboratory measurements were performed, like IV characterisation and Transient Current Technique measurements, presented in Chapter 6 and Chapter 7. Sensors from Hamamatsu Photonics with different design properties were tested. By alternating different design parameters, the influence on the sensor behaviours could be deduced. Measurements of various sensors were performed in the period in October 2018 until September

2019 with the main focus on the homogeneity, the feasibility of large sensors in sufficient sizes ($\approx 2 \times 2$ cm^2), fill-factor and radiation hardness. Radiation hardness is one of the most critical parameters of the HGTD. It is crucial that the detector can withstand the harsh environmental conditions during the lifetime of the HL-LHC running. At the end of the HL-LHC, the maximum neutron-equivalent fluence at a radius of 120 mm, is expected to reach 6.8×10^{15} $n_{eq}cm^{-2}$ [5]. With the replacement of the sensors two to three times, the radiation is planned to be limited to 2.5×10^{15} $n_{eq}cm^{-2}$.

2 The Standard Model of Particle Physics

In this chapter, an overview over the fundamentals of particle physics will be provided. The elementary particles and their properties are presented in the context of the Standard Model.

The Standard Model of Particle Physics (SM) reflects the current knowledge of elementary particles and the interactions between them [6–8]. It successfully describes physical phenomena on scales below 1 fm. A side from gravity, all fundamental forces are included in the SM, which was presented in the 1970s. Historically, the SM was developed from separate theories for the electromagnetic, weak and strong force, which are described in a relativistic and local gauge-invariant Quantum Field Theory (QFT) [9, 10]. With this, a function that describes all elementary particles and forces that were observed in the laboratory to date — except gravity, was formulated: The Lagrangian. It is characterised by a $\mathrm{SU(3)_C} \times \mathrm{SU(2)_L} \times \mathrm{U(1)_Y}$ gauge symmetry.

The Standard Model contains 16 particles and their respective antiparticles and eight gluons, which are divided into fermions, with half-integer spin, and bosons, with integer spin. They are graphically represented in Figure 2.1. Gauge bosons, which mediate the forces, are spin-1 particles. The photon (γ) is the massless, neutral charged gauge boson that mediates the electromagnetic force. The $W^{\pm}$ with a mass of (80.375 ± 0.023) GeV [11] have either a positive or negative electric charge of one elementary charge and are each other's antiparticles. The Z^0 with a mass of (91.1876 ± 0.002) GeV [11] is not charged. The Z and W bosons are the mediators of the weak force. The eight massless gluons that carry colour charge are the mediators of the strong force. Additionally, the spin-0 Higgs boson is an elementary particle in the SM, produced by the quantum excitation of the Higgs field [1–3].

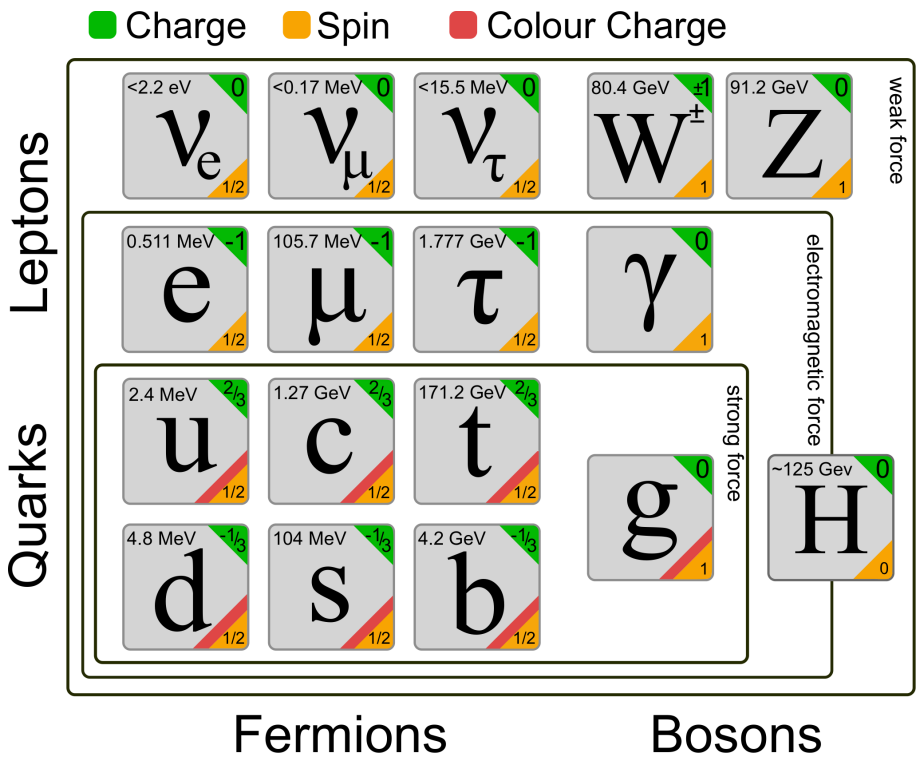

Figure 2.1: A graphical representation of the particles in the Standard Model of Particle Physics. The number in the upper right corner gives the electric charge and the number on the lower right corner indicates the spin of the particle. On the top left, the mass of the particle is given. A red strip on the right bottom corner indicates whether the particle carries colour charge. Values taken from [11].

Fermions are divided into leptons and quarks, which are arranged in three generations, as shown in Figure 2.1. The mass of the fermion increases with increasing generation. Particles from the second and third generation can decay into lower generation particles through a W boson, due to their higher mass compared to the first generation. Leptons exist either as charged or uncharged particles. While the charged leptons interact via the electromagnetic force as well as the weak force, the uncharged leptons, which are called neutrinos, can only interact via the weak force and therefore rarely interact with other particles. As a consequence, it is rather laborious to detect neutrinos. It should be noted, however, that in the Standard Model, the lepton family number is an approximately conserved quantity of the weak interaction. Therefore, for every decaying charged lepton of a generation, a neutrino of the same generation must be generated. However, the lepton family number is notably not conserved in neutrino oscillation. The muon has a lifetime of 10^{-5} seconds, the tau one of 10^{-13} seconds, while particles from the first generation are stable and participate in the formation of massive stable matter.

Quarks have an electrical charge of $\frac{+}{2}3$ or $-\frac{1}{3}$ in units of the elementary charge and carry colour charge. They carry one of three colours, namely red, green and blue. The colouring scheme is inspired by the additive colour mixing theory from optics. Colour charge is the reason quarks can interact via the strong force, which couples quarks together to form protons, neutrons, and other hadron particles. The fact that they carry colour charge gives quarks a unique feature called confinement, which causes that colour charged particles cannot be isolated and therefore cannot be observed on their own, such as quarks and gluons. Instead, they form colour neutral hadrons.

3 The Large Hadron Colider

Given the High Luminosity upgrade of the CERN Large Hadron Collider (HL-LHC) and the therefore planned upgrade of the ATLAS detector, the current situation of the Large Hadron Collider and the ATLAS detector is recapitulated and the upgrade plans discussed.

3.1 The Large Hadron Colider

The Large Hadron Collider (LHC) was built in the existing ring tunnel of the European particle physics research centre CERN, in which the Large Electron-Positron Collider (LEP) was installed until its closure in 2000. The official commissioning of the LHC was on 10th September 2008, but due to a technical defect, operations had to be stopped after a few days. It could be repaired, within about a year the LHC was restarted on 20th November 2009.

The LHC is a synchrotron in a 26,659 m long underground ring with a tunnel tube about 3.8 m in diameter and is located at approximately 100 m underground [12]. The accelerator ring is not exactly circular, but consists of eight straight and eight curved sections which alternate. The tunnel accommodates two adjacent radiant tubes, including magnets and cooling devices, in which two proton beams circulate in opposite directions. The two beam tubes intersect at four points, where particle collisions take place. At the intersections, the four LHC-based experiments are located: the ATLAS Experiment, the CMS Experiment, the LHCb Experiment, and the ALICE Experiment.

Several pre-accelerators are part of the accelerator chain, which is shown in Figure 3.1. The protons are first accelerated in a linear accelerator and then in the two ring accelerators PS and SPS to an energy of 450 GeV. Afterwards, the protons are introduced in opposite directions into the two vacuum tubes of the LHC. The protons are bundled in 2808 packets of about 10^{11} particles each, which move through the accelerator in a time interval of 25 ns. The luminosity achieved in Run 2 is $2{\times}10^{34}$ cm^{-2}s^{-1} [13, 14].

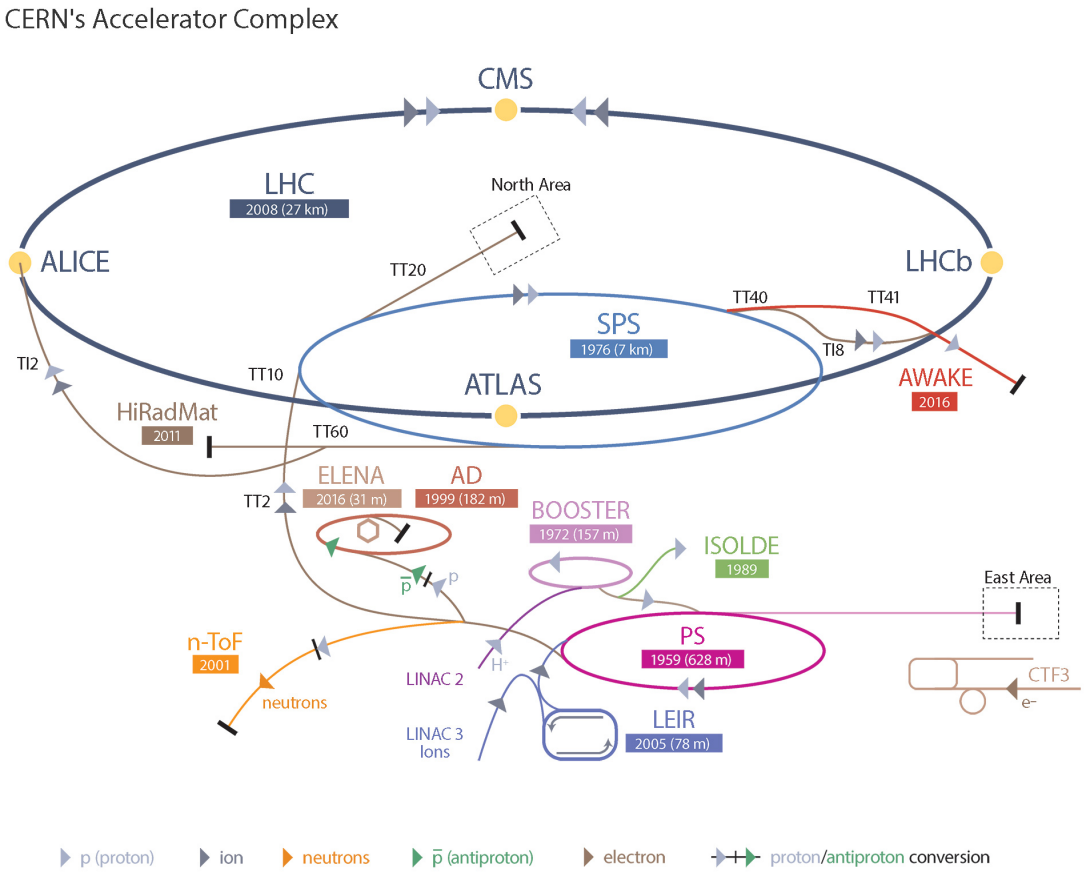

Figure 3.1: The accelerator chain towards the LHC at the CERN side. Copyright: CERN

3.2 The Atlas Experiment

The ATLAS Experiment, shown in Figure 3.2, is the biggest detector of all the experiments at the LHC and is one of the two multi-purpose experiments at the LHC [15]. It is about 44 m long and 25 m high and is built in a layered design that covers nearly the full solid angle around the collision point. Each layer has its particular purpose for the detection of the decay products of the collisions, with all of the detector components subdivided between a barrel and an end-cap part to provide maximum coverage.

The innermost layer is the tracker unit, which is enclosed in a solenoid magnet. The next layer is given by the electromagnetic and then the hadronic calorimeters. The outer layer is given by the muon chambers, which are also equipped with a toroidal magnet [16].

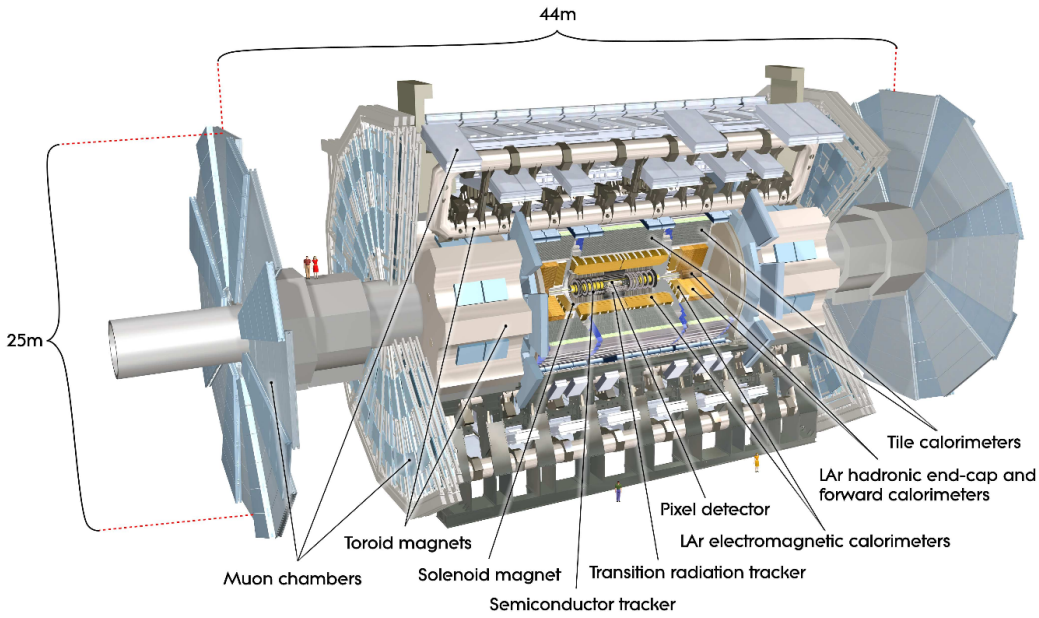

Figure 3.2: The ATLAS detector with all subsystems. Copyright: CERN.

3.2.1 Inner Detector

The Inner Detector (ID), shown in Figure 3.3, is designed to measure the direction, track, momentum, vertices and charge of electrically-charged particles produced in each proton-proton collision. For this purpose, the ID is placed as close as possible to the interaction point. It consists of four layers, which are the Insertable B-Layer (IBL), the Silicon Pixel Detector, the Semiconductor Tracker (SCT) and the Transition Radiation Tracker (TRT) [17, 18]. The IBL was added after the first run of the LHC to improve b-tagging and redundancy. b-tagging indicates the identification of b-hadrons in jets. The methods for b-tagging are based on the unique features of b-jets to distinguish them from jets containing only lighter quarks. It relies on the sufficient lifetime of the order of 1.5 ps of b-hadrons, which leads to a measurable flight length path of typically a few millimetres before the subsequent decay into lighter hadrons [19]. Therefore, hadrons that contain b-quarks decay inside the detector rather than escape. b-tagging is essential for many physics analyses, like Higgs boson researches or top mass measurements. The advent of precision silicon detectors has made it possible to identify particles that originate from a different vertex, where the bottom quark was formed, and thus indicating the likely presence of a b-jet [20]. The whole ID is located in a vessel with a length of about 7 m and a radius of 1.15 m. The ID is cooled to keep the noise low, for reasons based on the properties of silicon sensors as explained in Section 4.3, except for the TRT, which

is operated at room temperature. To measure the momentum, a strong magnetic field is applied parallel to the beam, by a central solenoid magnet that provides a 2 T magnetic field. Charged particles are thereby bent by the Lorentz force, which acts perpendicularly to their motion and the field on them and forces them on a curved trajectory. With the bending radius of this trajectory, the transverse momentum p_T is determined. The overall momentum resolution, including TRT, is $\sigma_{\mathrm{p_T}}/p_{\mathrm{T}} = 0.05\ \%p_{\mathrm{T}}$.

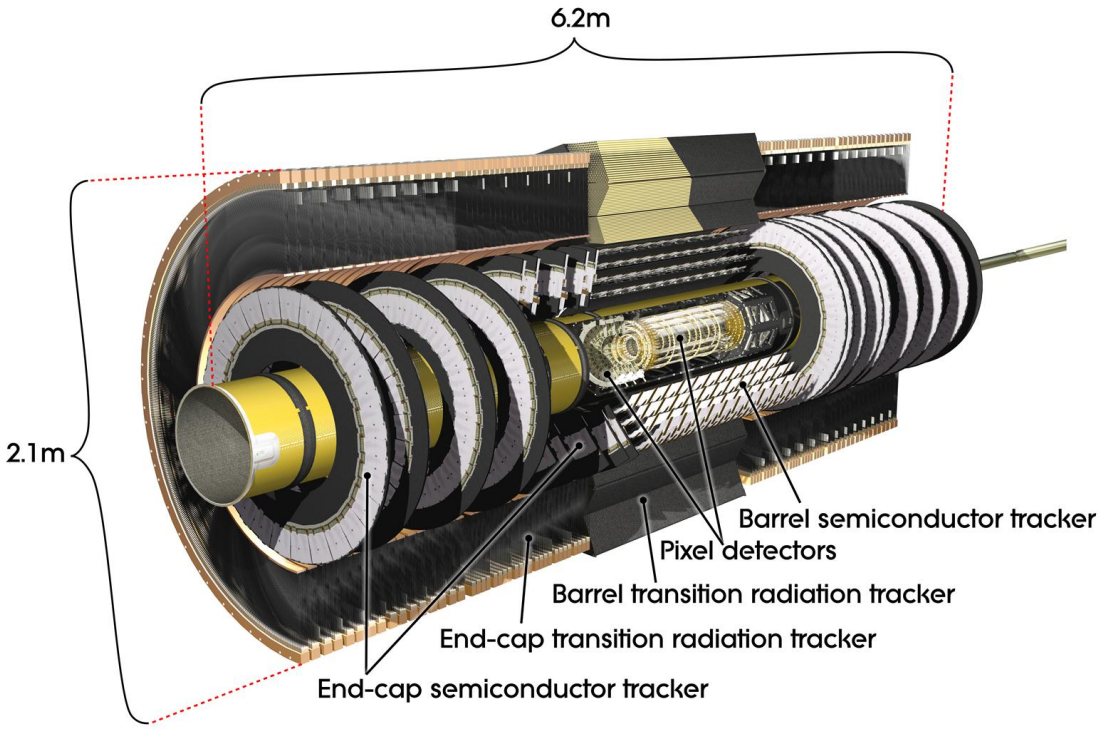

Figure 3.3: Cut-away image of the ATLAS Inner Detector. Copyright: CERN

The Insertable B-Layer (IBL) was built to cope with high radiation and occupancy. It is the first large scale application of 3D sensors and CMOS 130 nm technology [21, 22]. The layer of silicon pixel modules has a pixel pitch of 250×50 µm^2 at a radius of 33 mm from the beamline and covers a pseudorapidity range of $|\eta| \leq 2.9$. Pseudorapidity η is a parameter to express angles with respect to the axis of the colliding beams. It has the value 0 for particle trajectories that are perpendicular to the beam, and positive or negative values for those at an angle to the beam.

The next layer is the silicon Pixel Detector, which mostly determines the impact parameter resolution and the ability of the Inner Detector to find short-lived particles such as B-Hadrons. The impact parameter is a combination of a transverse coordinate, which

gives the signed distance to the z-axis, and a longitudinal coordinate, which gives the z-coordinate of the track at the point of closest approach to the global z-axis. Here, the z-axis is analogue to the beam axis. Impact parameters are one of the most essential criteria for reconstructed track selection and therefore, the impact parameter resolution is vital for correct track selection. The Pixel Detector consists of three layers located at a radius of 50.5 mm, 88.5 mm and 122.5 mm away from the interaction point with a pixel size of 50×400 µm^2. In the end-caps, three disks are installed on each side, which are at 495 mm, 580 mm, and 650 mm from the centre with the same pixel size as in the barrel region. The spatial resolution is 10 µm in the transverse plane and 115 µm in z-direction for barrel and end-cap [15].

The next layer is the Silicon Microstrip Detector System (SCT), which is designed to provide eight precision measurements per track in the intermediate radial range, contributing to the measurement of momentum, impact parameter and vertex position [23]. It consists of silicon strip detectors, which were chosen because the SCT has to deal with a lower track density. Therefore it was designed with a lower granularity than the pixel detector layer and the strips have a pitch of 80 µm. The spatial resolution is 17 µm in the transverse plane and 580 µm in z direction for barrel and end-cap. In the barrel part are four layers between 299 mm and 514 mm from the interaction point and in the end-caps are nine layers on each side, extending the structure up to approximately 2.7 m on each side of the collision point. To obtain a better 2D resolution, strips are located back to back with a stereo angle of 40 mrad [17].

The last layer of the ID is the Transition Radiation Tracker (TRT), which was designed to help with the identification of particles, such as the distinction between electrons and charged pion [15]. The TRT is a gaseous detector, using Xe and CO_2. It is constructed out of polyamide straw tubes of 4 mm diameter containing the gas. A tungsten wire is located in the middle to collect the generated signal. Between the tubes, radiator material is placed. If particles pass by, they will emit transition radiation when transversing the boundary surface. This radiation ionises the gas, which is measured and used to identify electrons and pions. The spatial resolution is 130 µm. In the barrel part, the tubes are 554 mm to 1082 mm away from the interaction point. In the end-caps, they are located outside the SCT end-cap.

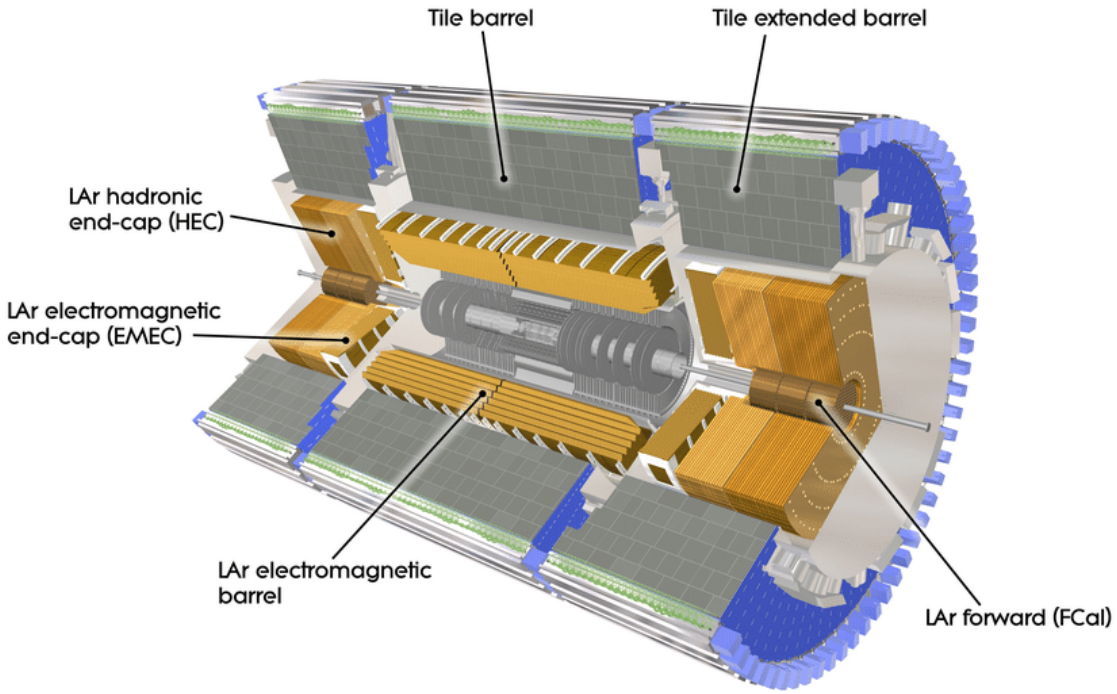

Figure 3.4: A closer view on the ATLAS calorimeters. Copyright: CERN

3.2.2 Calorimeter

The ID is enclosed by the electromagnetic calorimeter and the hadronic calorimeter, both shown in Figure 3.4. The calorimeter in the ATLAS detector measures the energy and direction of particles leaving the ID. For this purpose, the particle energy is completely deposited in the detector. The calorimeter is segmented for spatial resolution. Since different particles interact in a different way with matter, the calorimeter is divided into the electromagnetic and hadronic calorimeter.

Electromagnetic Calorimeter

In the electromagnetic (EM) calorimeter, mostly electrons and photons are absorbed, while hadrons and muons pass through it. The ATLAS electromagnetic calorimeter is built as a sampling calorimeter, which means layers of passive absorber alternate with active detector layers [24]. The active material in the EM calorimeter is liquid argon (LAr) and the absorption material is lead. The shower inside the calorimeter is created by ionisation of the liquid from an incoming photon or an electron, which creates electron-positron pairs that also react with the absorber material. These free electrons will drift towards an anode under an applied electric field, creating an amplified signal.

Hadronic Calorimeter

The hadronic calorimeter surrounds the electromagnetic calorimeter. It is split in a barrel part and an end-cap part [25]. Additionally, the forward calorimeter is located around the beam pipe and enclosed by the hadronic end-cap calorimeter. The barrel part is split into two sections, with one section that is located behind the EM-calorimeter and the other above the end-cap wheels. Both parts are built with steel as the absorber material and scintillating tiles as the active readout material. In contrast to the barrel part, the end-cap wheels use liquid argon and copper as active material and absorber, respectively. The thickness is ten interaction lengths, which is a characteristic of a material related to the energy loss of high energy particles electromagnetically interacting with it. Finally, the forward calorimeter is subdivided into three parts. In the first one, copper is used as the absorber material, while in the other two tungsten is the material of choice. For all three parts, liquid argon is used as the active material. Here again, the spatial extension corresponds to ten interaction lengths.

3.2.3 Muon Chamber

Since muons are minimum ionising particles, they can penetrate through the ID and calorimeter and therefore a separate detector unit is built to enhance the measurement of their momentum and identify them, shown in Figure 3.5. For this purpose, a magnetic field is applied by a strong toroidal magnet, to create a curved trajectory. In the central area of the ATLAS detector, eight superconducting solenoids generate a magnetic field in a large volume with an integrated bending force of three to eight Tm. The toroidal system contains more than 70 km of superconducting cable and has a nominal current of 2×10^4 A with a stored energy of more than one GJ [26].

Most of the muon detectors consist of long gas-filled drift tubes under high pressure with an anode wire, which is stretched parallel to the cylinder axis. Again, the locations at which the particles pass the tubes are registered by the ionisation of the drift chamber gas. From the measurement of the drift time, the coordinates can be measured with an accuracy of about 100 µm.

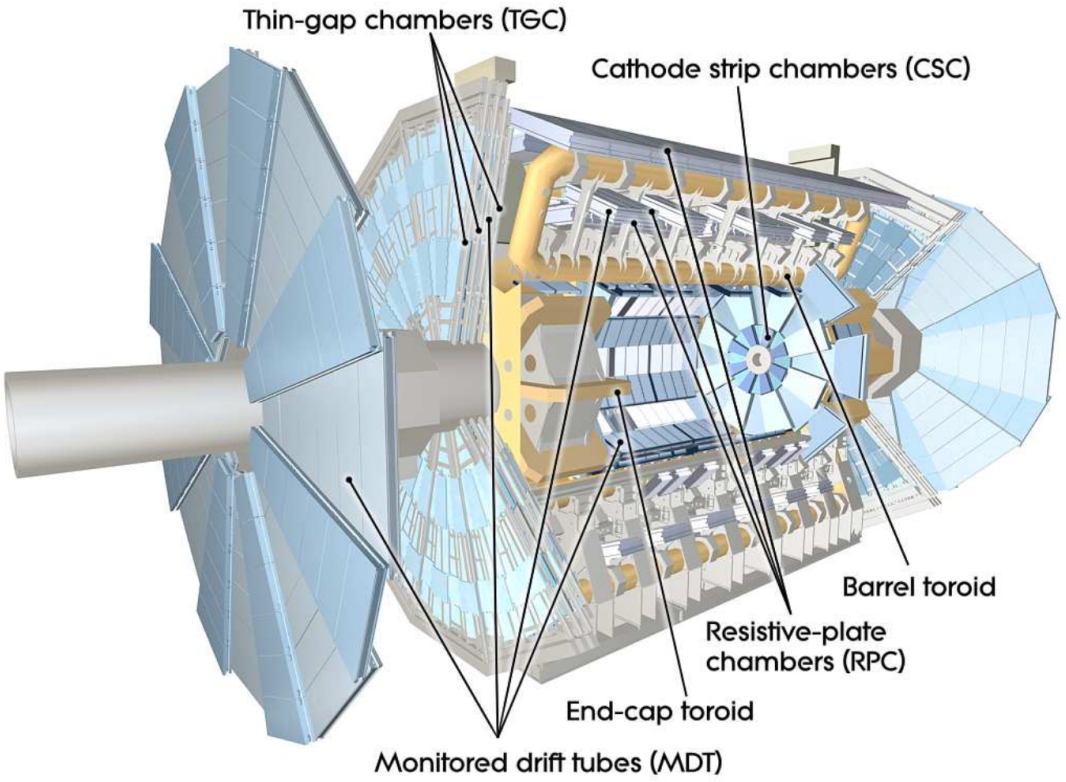

Figure 3.5: The muon system of the ATLAS detector. Copyright: CERN

3.3 The High Luminosity LHC and its Consequences on the Atlas Detector

To improve the sensitivity of searches for physics beyond the SM and higher-precision measurements of, for example, the properties of the Higgs boson, an upgraded programme of the LHC for 2024 is planned: The High-Luminosity LHC (HL-LHC) [27]. With this upgrade, the instantaneous luminosity, which gives the number of particles flowing through a surface in an interval of time, should be enlarged by a factor of five and thereby enable the experiments to increase the number of collisions that occur in a given amount of time. Therefore more data can be gathered and rare processes can be observed. The start of the measurements with the HL-LHC is planned for the middle of 2026. This enlarged luminosity affects the detectors greatly due to event pile-up, which is the superposition of several events during one bunch crossing. In the nominal operation scheme, the interaction region will have a Gaussian spread of 45 mm along the beam axis and a pile-up of around 200 simultaneous proton-proton-interactions on average ($< \mu >= 200$), corresponding to an average interaction density of 1.8 collisions/mm.

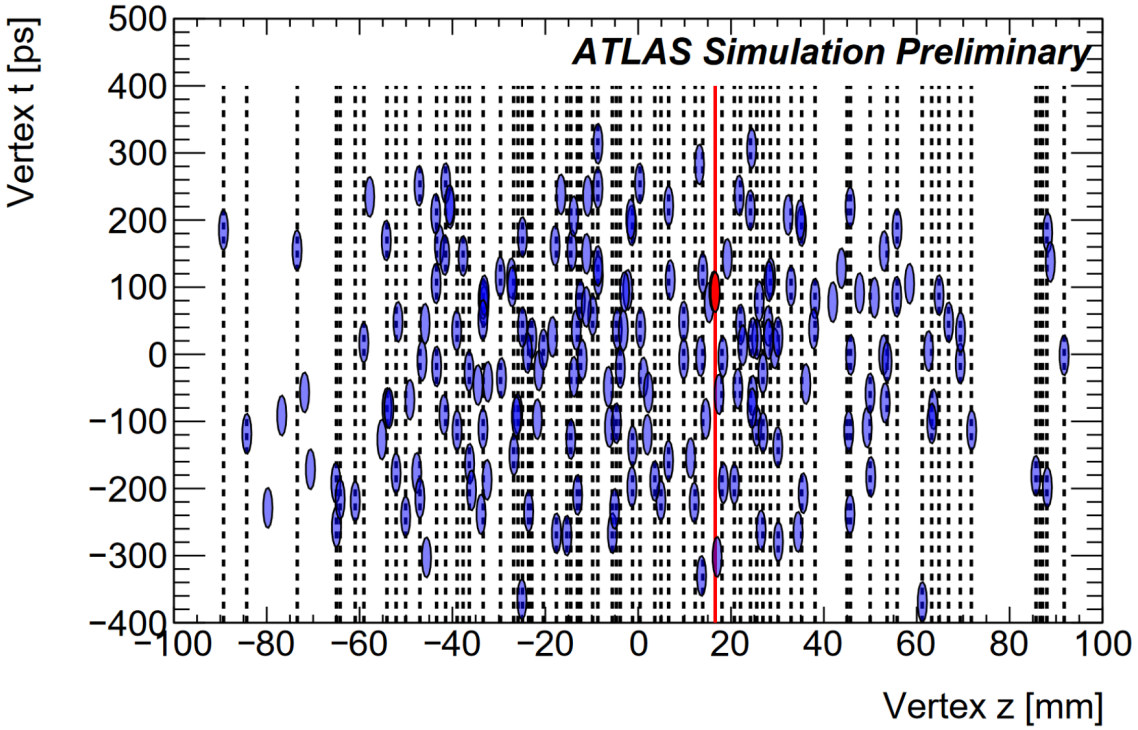

Figure 3.6: Visualisation in the zt-plane of an event with a hard scatter (red ellipse) with about 200 pile-up interactions (blue ellipses) superimposed. The dashed vertical lines represent the position of reconstructed vertices [5].

The substantial increase of pile-up is one of the main experimental challenges for the HL-LHC. For this purpose, a new Inner Tracker (ITk) is planned for the ATLAS Experiment. The vertex resolution of the ITk decreases for high η. Therefore additional measures are planned for improved vertex resolution for high η. A new technique to mitigate the effects of pile-up is the use of high-precision timing measurements to distinguish between collisions occurring close to each other in space, but well-separated in time, as shown in Figure 3.6. A High-Granularity Timing Detector (HGTD) is therefore proposed for the ATLAS Phase-II upgrade [5]. The HGTD is based on the Low Gain Avalanche Detector technology (LGAD), which is further explained in Section 5. The HGTD covers the forward region, since for good spatial separation of the HL-LHC collision vertices, σ_{z_0} should be significantly better than the inverse of the average pile-up density, 600 µm. Figure 3.7 shows the rejection of pile-up jets for the ITk in combination with the HGTD and without it. However, in the forward region the resolution exceeds the limit by a sizable factor, reaching 3 mm for particles with low transverse momentum at $|\eta| \approx 4$. As a result, the ITk by itself cannot associate such forward tracks to the correct vertices in an unambiguous way.

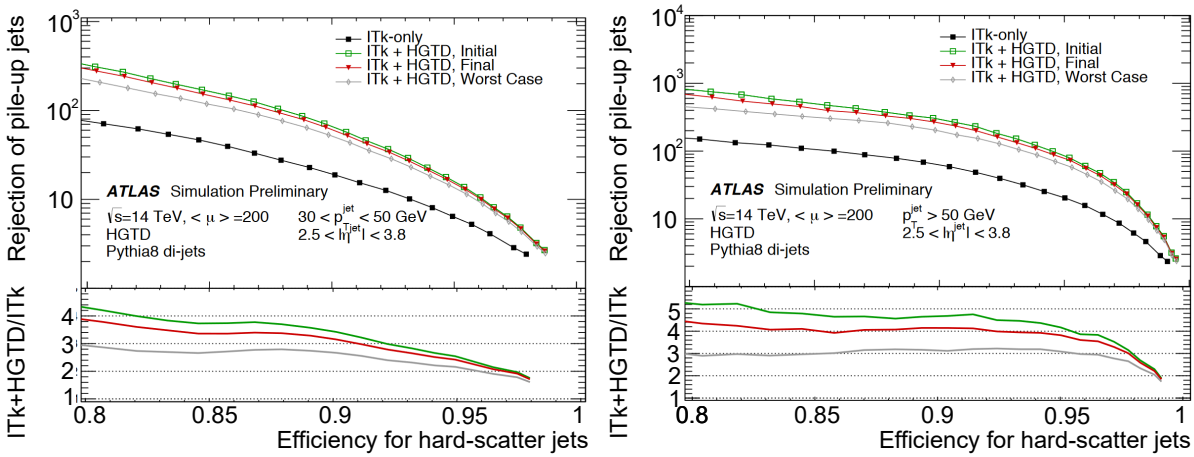

(a) Jets with $30 < p_{\mathrm{T}} < 50$ GeV. (b) Jets with $p_{\mathrm{T}} > 50$ GeV.

Figure 3.7: Pile-up-jet rejection as a function of hard-scatter jet efficiency in the $2.4 < |\eta| < 4.0$ region, for the ITk-only and ITk and HGTD scenarios with different time resolutions [5].

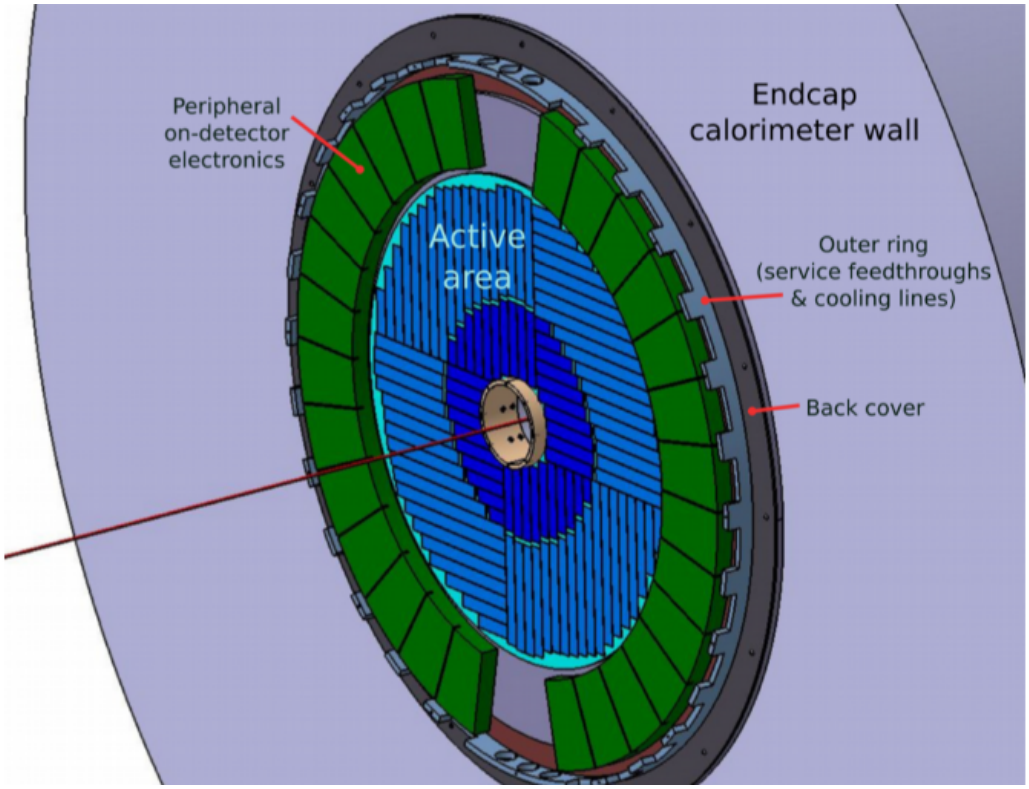

Figure 3.8: Overview of the HGTD. The active area has two sensor placement densities, coloured in dark and lighter blue. The area closer to the beam, coloured in dark blue, has a higher sensor placement density. The green part shows the placement of peripheral on-detector electronics [5].

The HGTD is planned to consist of two circular disks placed in between the ITk and the end-cap of the calorimeter at 3.5 m distance of the interaction point, with an active area of 120 mm $< R <$ 640 mm, corresponding to $2.4 < |\eta| < 4.0$, and a thickness of 75 mm. Figure 3.8 shows the HGTD with the active area. Inside the main vessel of each end-cap are two cooling disks. On each side of the disks, narrow rectangular staves are placed with sensor modules. The disks with the staves are structured along R to measure traversing particles with an average of three hits at $R < 320$ mm and two at $R > 320$ mm. This is achieved by placing each module with a certain overlap between the front and back of the cooling disk. Both sides of the cooling disk are covered with identical $20{\times}40$ mm^2 modules consisting of LGAD sensors, which are further explained in Chapter 5, that are connected via bump-bonds to an ASIC, called ALTIROC, and flex circuits for readout purposes.

The HGTD is designed to measure tracks from minimum-ionising particles (MIPs) with a timing resolution of 30 ps, which will improve the pile-up mitigation up to $|\eta| < 4$. It is planned to measure the timing information for nearly all primary vertices and a timing determination for charged particles in the region of $2.4 < |\eta| < 4.0$. The main features for the HGTD are the precision time measurement capability, which among other things enhance the performance for tagging jets as well as b-tagging. Additionally, a luminosity measurement can be performed and ways to use it for the trigger system are discussed in the ATLAS collaboration.

4 Principles of Silicon Particle Detectors

4.1 Fundamental Properties of Silicon

Most high-resolution particle tracking detectors in high energy physics are made out of silicon. Silicon is one of the most widely spread element after oxygen, since the earth's crust consists of about 28 % silicon. It oxidises rapidly in contact with oxygen and therefore is usually present as silicon-oxide or in other compounds, which must first be processed to obtain pure silicon. Because the processes for producing high purity silicon are well controlled industrially, it can be produced relatively inexpensively in large quantities.

Besides the good availability and the high purity achieved, other properties of silicon make it an attractive material for particle detectors, explained in the further chapter.

Due to the dense periodic arrangement of the atoms in the crystal lattice of the silicon, the energy levels of the individual atoms are so close together that they can be combined into energy bands. Valence electrons are bound to individual atoms in the valence band, whereas electrons in the conduction band can move freely in the atomic lattice. The bands are separated by an energy gap, which is the bandgap. In metals, these two bands overlap, which explains their high conductivity. In contrast, insulators have a large gap (> 3 eV). The gap in semiconductors is usually less than 3 eV, so that atoms can be ionised even at lower energies and thus free mobile charge carriers in the sensor arise. Silicon has a bandgap of 1.12 eV and is hence a semiconductor.

The basic operating principle of silicon detectors is that electron-hole pairs are created due to incident ionising radiation. The created charge carriers induce a signal while drifting toward the electrodes due to an electric field, which is described by the Ramo-Theorem [28, 29].

4.2 Energy Loss of Particles

Particles with different properties interact with the detecting materials differently. Consequently, the different layers in the ATLAS Experiment, presented in Chapter 3, are needed. All detector signals depend on the deposited energy of the interacting particles.

4.2.1 Charged Particles

For heavy charged particles[1], the primary process of energy loss is ionisation in the energy range relevant for particle physics [30]. The mean energy loss of ionisation per distance, normalised with the density of the material, also called stopping power, is mathematically described by the Bethe-Bloch-equation (Equation 4.1). Ionisation describes the process of scattering of bypassing particle with the electrons of the absorber material, whereby an electron gets pushed out of the atom and accordingly a free electron and a hole are created in the semiconductor.

$$-\left\langle \frac{\mathrm{d}E}{\mathrm{d}x} \right\rangle = Kz^2 \frac{Z}{A} \left[\frac{1}{2} \ln \frac{2m_e c^2 \beta^2 \gamma^2 T_{\max}}{I^2} - \beta^2 - \frac{\delta(\beta\gamma)}{2} \right] \tag{4.1}$$

Here $\mathrm{d}E/\mathrm{d}x$ describes the energy loss in $\mathrm{eV(g/cm)^{-2}}$. K is a constant that equals $4\pi N_{\mathrm{Av}} r_{\mathrm{e}}^2 m_{\mathrm{e}} c^2$, with the Avogadro constant N_{Av}, the Bohr radius r_e, the electron mass m_e and the speed of light c [31]. Additional variables used are the charge of a traversing particle z in units of the elementary charge, the atomic number of the medium Z, the atomic mass of the medium A, the rest energy of the electron $m_e c^2$, the velocity of the traversing particle $\beta = v/c$, the Lorentz factor $\gamma = 1/\sqrt{1-\beta^2}$, the mean excitation energy of the medium I with 137 eV for silicon and the density correction δ. $T_{\max}$ is the maximum possible momentum transfer given by [32]

$$T_{\max} = \frac{2m_e c^2 \beta^2 \gamma^2}{1 + 2\gamma m_e/M + (m_e/M)^2},$$

with M the mass of the traversing particle. For lower energies, the $1/\beta^2$-term is dominant, while for high energies the function rises logarithmically. In between, the function has a minimum at $\beta\gamma \approx 3$. The trend of the curve is shown in Figure 4.1. Due to the flat rise, particles with $\beta\gamma$ around three are called minimum ionising particles (MIP), until radiated loss becomes dominant. The energy transfer in single collisions is, in most cases, larger than the minimum energy needed to create an electron-hole pair, i.e. the bandgap. Therefore, kinetic energy is transferred to the electron, which then loses energy in photon

[1] here, heavy means with a mass larger than the electron mass ($M >> m_e$)

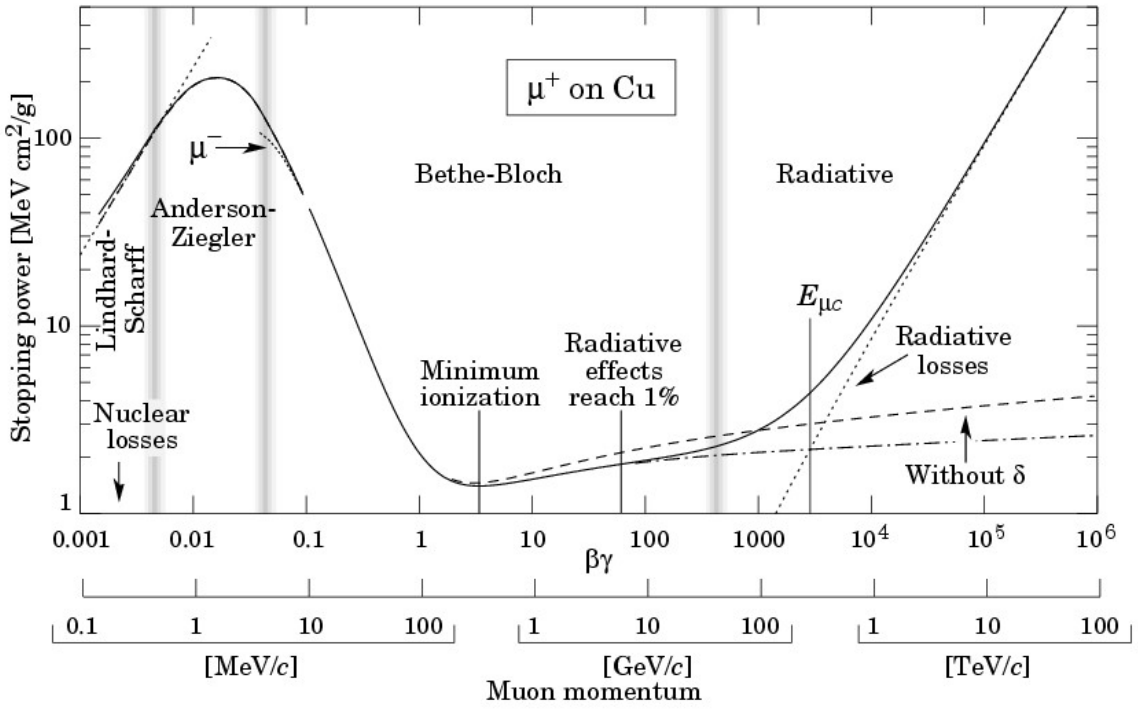

Figure 4.1: The trend of the curve for the Bethe-Bloch-equation: the stopping power against $\beta\gamma$ on a logarithmic scale [11].

excitation and ionisation. On average 3.6 eV are required per produced e-h pair [32].

For light charged particles, such as electrons, the Bethe-Bloch-equation is not valid. Certain effects have to be taken into account, such as electrons being indistinguishable from the shell electrons of the material, and due to the low mass of electrons, a significant energy loss due to bremsstrahlung is added.

4.2.2 Photons

Photons show a different behaviour in their interaction with matter compared to charged particles. They do not interact with matter by ionisation. Instead, the most important mechanisms of interaction are the photoelectric effect, Compton scattering, and pair-production. As a consequence of this kind of interactions a photon that interacts with matter is removed from the incident beam [33].

As shown in Figure 4.2, the cross-section of these processes depends on the energy of the photon. For a photon in the energy range of 0 to 100 keV, the photoelectric effect is dominant. In this process, an electron is emitted by absorbing a photon, whose energy is

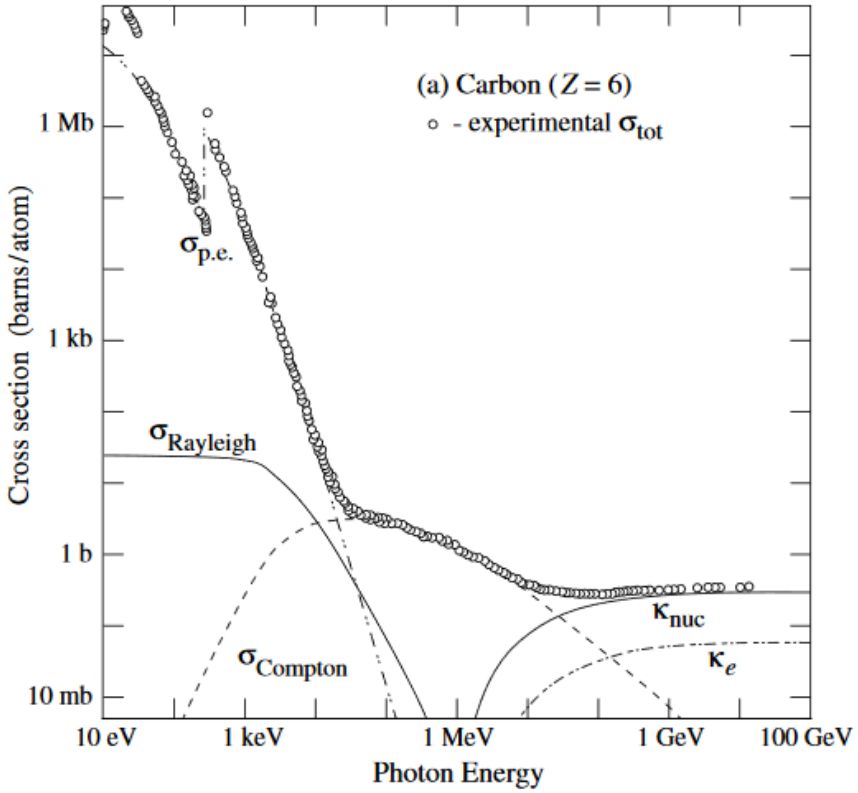

Figure 4.2: Cross-section of photons as a function of the energy for the corresponding interaction effects [11].

larger than the binding energy of the electron in the atom. The rest of the photon energy contributes to the kinetic energy of the electron. For photon energies between 100 keV and 10 MeV the Compton effect is most probable. The photon scatters on a quasi-free electron and transfers parts of its energy to the electron. For photons with even higher energies, pair production becomes the dominant process. With a photon energy that is slightly above 1 MeV, an electron-positron pair can be produced.

A photon beam is characterised by its intensity. For a beam of photons that passes through matter, the intensity of the beam decreases exponentially with the thickness of the passed material, here labelled with x [33]:

$$I(x) = I_0 \mathrm{e}^{-\mu x}, \tag{4.2}$$

with the initial intensity I_0 and the material-specific and energy-dependent mass attenuation coefficient μ.

4.3 pn-Junction

In order to measure the ionisation signal, a semiconductor bulk can be prepared to collect and process the deposited charge. To build a sensor, a junction of differently doped silicon is used. Doping refers to the process of introducing foreign atoms into the silicon lattice, where the n-type material is doped with donor atoms that have one additional valence electron and the p-type is doped with acceptor atoms that have one valence electron less than the material. Typical elements used for silicon are gallium, aluminium, indium or boron as p-type dopants and phosphorus or arsenic for n-type materials. Pn-junctions are then used as basic building blocks for semiconductor detectors [34].

A basic diode structure with a pn-junction is the foundation for all further sensors. Because the concentrations of charge carriers, here electrons and holes, between both materials differ, the holes diffuse towards the n-region and vice versa, which then recombine. This leads to fixed space charges in the junction region that are depleted of free charge carriers, which generates an electric field, shown in Figure 4.3. The electrical field causes a drift current counteracting the diffusion current. In thermal equilibrium, this causes a built-in voltage V_{bi} [32]:

$$V_{\mathrm{bi}} = \frac{kT}{q} \ln \frac{N_{\mathrm{A}} N_{\mathrm{D}}}{n_{\mathrm{i}}^2} \tag{4.3}$$

with the number of acceptors N_{A} and the number of donors N_{D}. k is the Boltzmann constant and T the temperature. q is the charge and n_{i} is the intrinsic carrier concentration of 1.45×10^{10} cm^{-3} at 300 K in silicon. The intrinsic depletion region generated by the electric field $E = qV_{\mathrm{bi}}$ caused by the built-in voltage would be too small to be used for charge collection. Therefore, an external voltage is applied to deplete the bulk of free charge carriers and generate an electric field in the full sensor volume. The voltage

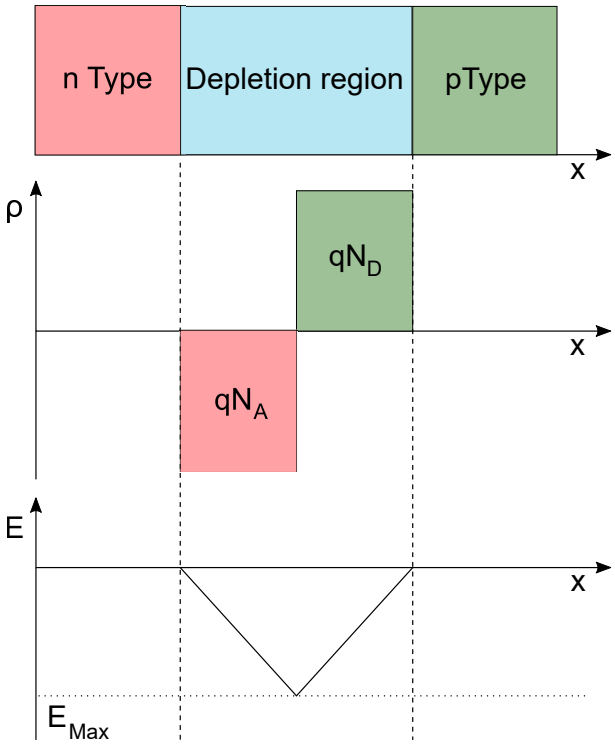

Figure 4.3: A schematic drawing of a pn-junction, with the depleted zone between n- and p-region coloured in blue. The electrical field in dependence on the N_{D} and N_{A} concentration is shown.

applied depends on the thickness of the sensor. The depletion depth d can be calculated by [32]

$$V_{\text{dep}} = \frac{d^2 \cdot qN_D}{2\epsilon_0\epsilon_r} - V_{\text{bi}}. \tag{4.4}$$

V_{bi} is normally neglected, because it is small. The signal behaviour of the sensor depends on the applied voltage, since the depletion width and the electric field depend on it. A

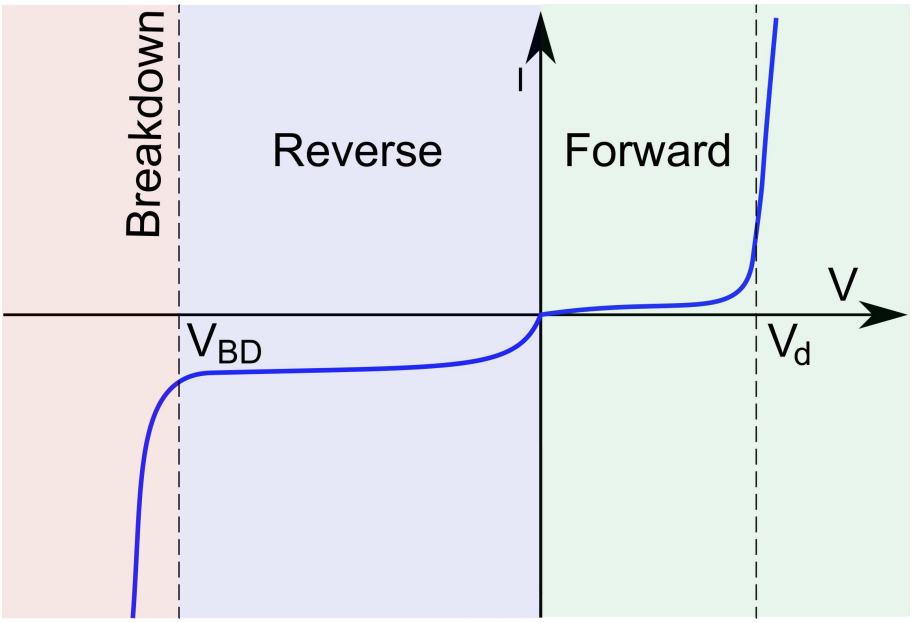

Figure 4.4: Qualitative example of the current behaviour for a diode in dependence of the applied voltage. The three main areas of operation are shown. In green, the forward-biased region is marked, in blue the reverse-biased region and in red the breakdown region. V_{BD} labels the breakdown voltage and V_{d} denotes the voltage in the forward region that is equivalent to the threshold voltage, i.e. the voltage needed to counteract the internal field so that the diode conducts in the forward direction.

silicon detector is operated with reverse bias, hence the leakage current is relevant. This current is dominated by thermally generated e-h pairs, which cannot recombine and are separated due to the applied electric field. The drift of the electrons and holes to the electrodes causes the leakage current [32]:

$$I_{\text{leak}} \propto T^2 \exp\left(-\frac{E_{\text{G}}}{2kT}\right), \tag{4.5}$$

with the temperature T in Kelvin, the bandgap in silicon with $E_G = 1.12\,\text{eV}$ and the Boltzmann-constant k. The rule of thumb is that for every 8 °C of temperature increase, the leakage current doubles. The generated leakage current is proportional to the sensor

volume, since recombination centres in the volume generate leakage current. For a sensor, the leakage current behaviour is measured against the applied external voltage V_{ext}, which is called a current-voltage-curve or IV-curve. The qualitative behaviour of such a curve is shown in Figure 4.4. This curve is an important tool for quality checks for sensors, since the breakdown voltage needs to be high enough to deplete the sensor fully and the noise depends on the I_{leak}. The voltage needed for complete depletion is given by [32]:

$$V_{\text{fd}} = \frac{e}{2\epsilon_0\epsilon_{\text{r}}} N_{\text{eff}} d^2 = \frac{e}{2\epsilon_0\epsilon_{\text{r}}} \left(N_{\text{D}} - N_{\text{A}}\right) d^2, \tag{4.6}$$

with the effective doping concentration $N_{\text{eff}} = N_{\text{D}} - N_{\text{A}}$, the elementary charge e, the vacuum permittivity ϵ_0, the medium's relative permittivity ϵ_{r}, the depletion depth d^2, is the number of acceptors N_{A} and the number of donors N_{D}.

4.4 Radiation damage

4.4.1 Radiation Damage Effects in the Crystal Lattice

Radiation can cause displacement damage to the crystal lattice by elastic coulomb or nuclear scattering between lattice atoms and the incident particle. This displacement causes an empty lattice site (vacancy) and an atom between the regular lattice positions (interstitial), which form together a *Frenkel pair*. If the kinetic energy of the recoil atom is high enough it can displace further atoms and cause thereby cascades and defect clusters.

At non-cryogenic temperatures, which are above 150 K, defects are mobile. Consequently, they can recombine and anneal or combine with other defects, with doping atoms or impurities and this way form stable defects.

Those defects have macroscopic effects, since they introduce energy levels in the band-gap and interact with the dopants. The effect of defect levels on the sensor properties depends on their position in relation to the valence and conduction band. The distance to the bands determines transition probabilities and the position with respect to Fermi level determines occupation of the state. Depending on this position, defect levels can act as donors or acceptors and thereby change the effective doping concentration, or compensate existing donors or acceptors and thereby also change the effective doping concentration. In some cases the defects act as generation centres for electron-hole pairs and increase the leakage current or act as traps and decrease the charge collection efficiency. Therefore, trapping leads to signal degradation.

The transition probability between states depends exponentially on the energy difference. Hence defect levels in the middle of the band-gap have the highest probability for simultaneous emission of a hole into the valence band and an electron into the conduction band. This causes the increase of the leakage current ΔI proportional to volume V and accumulated fluence Φ_{eq} [35]:

$$\Delta I = \alpha V \Phi_{\text{eq}}, \tag{4.7}$$

with the radiation-induced damage rate α, depends on time and annealing temperature.

In summary, radiation defects lead to higher leakage currents and a reduced signal. Caused by the increased leakage current, also the noise increases. Hence, the signal to noise ratio decreases significantly. Additionally, due to the increased leakage current, more powerful cooling systems are needed to compensate for the larger power dissipation. However, the cooling systems increase the inactive material in the detector.

The radiation damage is modelled by the Non-Ionising Energy Loss (NIEL) hypothesis [36]. It aims to scale the radiation damage of any particle fluence to an equivalent of the damage caused by a 1 MeV neutron fluence. The basic assumption of the hypothesis is that any induced displacement-damage $D(E)$ in the material is due to non-ionising energy transfer to the lattice and scales linearly with the amount of energy deposited in the material as

$$D(E) = \frac{A}{N_A} \frac{\mathrm{d}E}{\mathrm{d}x}(E), \tag{4.8}$$

with the energy E of the incident particle, the specific energy loss $\mathrm{d}E/\mathrm{d}x$, the atomic weight of the target material A and the Avogadro constant N_A. However, the NIEL scaling hypothesis should not be regarded as a universal rule. In fact, it can be argued that the real damage depends not only on the integral NIEL value, which summarises all existing reaction channels with their respective recoil energy distributions folded with the efficiency for producing displacements, but it might also depend on the specifics of the energy transfer. Hence, the NIEL hypothesis must be applied with caution. Nevertheless, it is useful to cancel out most of the particle and energy dependences of the observed damage in silicon detectors.

4.4.2 Change of Effective Doping Concentration

Radiation-induced defects can change effective doping concentrations by combining with dopants and this way deactivating them or introducing new levels which act like acceptors or donors [37]. The effective doping concentration change is shown as an example for n-type material since it is more common in literature.

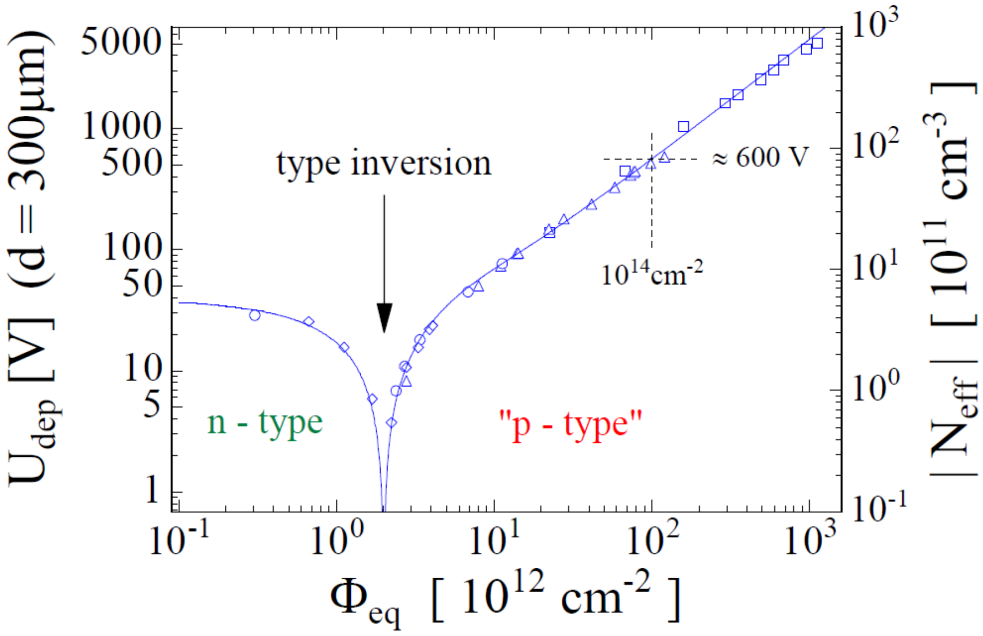

Figure 4.5: Absolute effective doping concentration in dependence of the 1 MeV equivalent fluence [38].

Then the most general form to describe the radiation induced change in the effective doping concentration is [36]

$$N_{\text{eff}} = N_{\text{D},0}e^{-c_{\text{D}}\Phi_{\text{eq}}} + g_{\text{D}}\Phi_{\text{eq}} - N_{\text{A},0}e^{-c_{\text{A}}\Phi_{\text{eq}}} - g_{\text{A}}\Phi_{\text{eq}}, \tag{4.9}$$

with the initial acceptor $N_{\text{A},0}$ and donor concentration $N_{\text{D},0}$, the acceptor c_{A} and donor removal rate c_{D}, and the introduction rate of acceptor-like g_{A} and donor-like defects g_{D}. The change in the effective doping concentration leads to type inversion in the n-type material. The effective doping concentration changes from positive to negative, converting an n-type material into a material with acceptor-like states, similar to p-type material. Figure 4.5 shows the absolute effective doping concentration and the depletion voltage as a function of the fluence. After the donor removal, acceptor-like states dominate. Caused by the change in the depletion voltage, the sensor operation has to be adjusted.

4.4.3 Trapping

Defect states can act as traps for charge carriers. Empty states act as traps for electrons, while filled states act as traps for holes. The release time of the trapped charge carrier depends on the energy difference between trap and valence or conduction band. Therefore, if the trap is too „deep“, the release time is longer than the time constant of the electronics and the charge carrier is lost for the signal. The trapping probability can be described by a time constant τ_{eff}, such that the charge after a drift time t is given by

$$q(t) = q(t_0) \cdot \exp\left(-\frac{t}{\tau_{\text{eff}}}\right) \tag{4.10}$$

From measurements, the conclusion can be drawn that the trapping probability $1/\tau_{\text{eff}}$ scales linearly with the fluence [39]

$$\frac{1}{\tau_{\text{eff}_{\text{e,h}}}} = \beta_{\text{e,h}}\left(t_{\text{anneal}}, T\right) \Phi_{\text{eq}}, \tag{4.11}$$

with annealing time t_{anneal}, temperature T and the temperature-dependent damage parameter for electrons and holes $\beta_{\text{e,h}}$, respectively.

For thin sensors, the effects of trapping are reduced. In a thinner sensor, a higher electric field is established at the same voltage. A better charge collection efficiency after irradiation is a consequence. Furthermore, charge multiplication effects can amplify the signal and a lower collection time decreases the possibility for trapping. Consequently, after irradiation, the signal is larger compared to thicker sensors.

4.4.4 Annealing

The defects caused by radiation are not stable, but can migrate, dissociate or form new and complex defects with other defects or impurities in the crystal lattice. This can lead to annealing of the radiation-induced damage, which does not imply the crystal is becoming perfect again, but a transformation of defects into more stable defects with different electrical properties.

The damage decreases with the annealing time, which depends on the environmental temperature. The leakage current related defects reduce over the duration of the annealing process.

Additional, by annealing of ΔN_{eff} is observed. The change in the effective doping concentration can be expressed by three terms with different annealing behaviour [36]:

$$N_{\text{eff}}(\Phi, T_{\text{a}}, t) = N_{\text{eff},0} - N_{\text{C}}(\Phi) - N_{\text{A}}(\Phi, T_{\text{a}}, t) - N_{\text{Y}}(\Phi, T_{\text{a}}, t), \tag{4.12}$$

with the stable damage term N_{C}, the annealing term N_{A} and the reverse annealing term N_{Y}. After irradiation, the annealing term N_{A} dominates until reaching a minimum, afterwards the reverse annealing term N_{Y} becomes dominant, which can lead to a larger change in effective doping than immediately after irradiation. The progress of the change in the effective doping concentration over time is shown in Figure 4.6. The reverse annealing can be „frozen “ at $T < 0$ °C. The stable damage part gives the smallest change that can be reached. One consequence for the operation of sensors is that the effect of radiation damage strongly depends on temperature even when there is no beam.

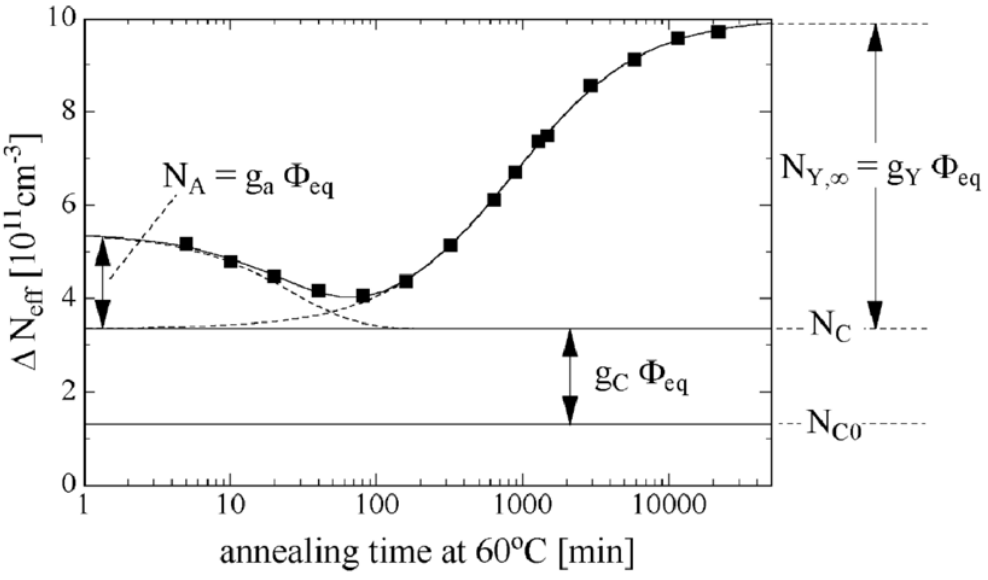

Figure 4.6: Change of the effective doping concentration as a function of annealing time at a temperature of 60 °C showing short-term, long-term annealing and stable damage [36].

One way to improve the behaviour of damage evolution is defect engineering. Impurities in the silicon crystal can change the behaviour of the radiation damage. For example, a high oxygen content in the silicon changes the behaviour of ΔN_{eff}, in particular, the constant term and the reverse annealing term. This has been used by artificially increasing the oxygen content of the silicon. It is currently under study whether other silicon processes can be even better in this respect.

Another aspect of annealing is the annealing of trapping. Opposite annealing behaviour for electron and hole trapping is observed. Hole trapping is increased by approximately 40 % after annealing. However, electron trapping decreases by approximately 20 % after annealing. In both cases, the time constants are around 10 h at 60 °C [40].

4.5 Hybrid Pixel Detectors

To obtain spatial resolved measurements from the sensors, they must be segmented. For this purpose, with planar n-in-p sensors, n^+-implants are placed on the front of the sensor in a lightly doped p-type substrate. In order to read out the individual pixels, a hybrid approach, as used in the ATLAS pixel detector, is used. The peculiarity of hybrid pixel detectors is that they consist of two subcomponents: the sensor and a readout chip. The two are connected in each pixel individually by conductive micro-compounds, so-called bump bonds, shown schematically in Figure 4.7. Under the bump bonds, a metal layer is applied, which is called under-bump metallisation (UBM). The UBM works as a foundation for the bump bonds and allows a stable and viable connection between the sensor and the bump bonds.

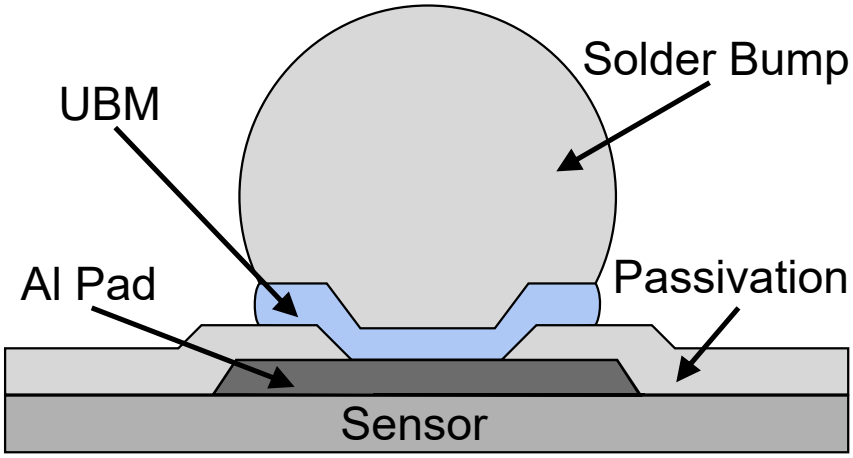

Figure 4.7: Schematic representation of a single hybrid pixel cell with passivation, under-bump metallisation and an unconnected bump-bond.

5 The Low Gain Avalanche Detector

5.1 Sensor Principle

The Low Gain Avalanche Detector (LGAD) is based on a standard n-in-p silicon pixel detector. This technology was pioneered by Centro Nacional de Microelectronica (CNM) Barcelona [41] and was further developed during the last 5 years within the CERN-RD50 community. By now, many other companies are involved in the production of LGADs, like Hamamatsu Photonics (HPK).

The basic structure is a highly doped n^+-electrode with a highly doped p-type region below, which is called the multiplication implant or multiplication layer. As a dopant for the p-type multiplication layer, boron is typically used. Through this structure, a strong electrical field is created near the pn-junction, which accelerates the signal charges in such a way that they create further e-h pairs and thereby enhance the signal. A schematic drawing of the structure and the generated electrical field are shown in Figure 5.1. Between the sensor pads, a no-gain gap is present. The distance is the nominal inter-pad gap (IP). The sensor is surrounded by a guard ring. The guard ring is included in the slime edge (SE), which is the distance from the last pad to the cut edge of the sensor.

As shown in Figure 5.1, the electric field in an LGAD is clearly divided into two distinct zones: the drift volume with rather low values of the electric field strength ($E \sim 30$ kV/cm), but high enough for drift velocity saturation and a thin multiplication zone located within a depth of a few micrometers with a very high field ($E \sim 300$ kV/cm) [42].

A gain factor of ten to fifty is achieved, which strongly depends on the doping concentration and the thickness of the p-type multiplication layer as well as the shape of the profile [43]. The electrical field lines are also affected by the Junction Termination Extension (JTE). The JTE is an n^+-implantation around the multiplication layer that is deeper than the one of the central pad. The field lines are strongly dependent on the JTE and the applied bias voltage. For low voltages, the field lines do not show the ideal shape

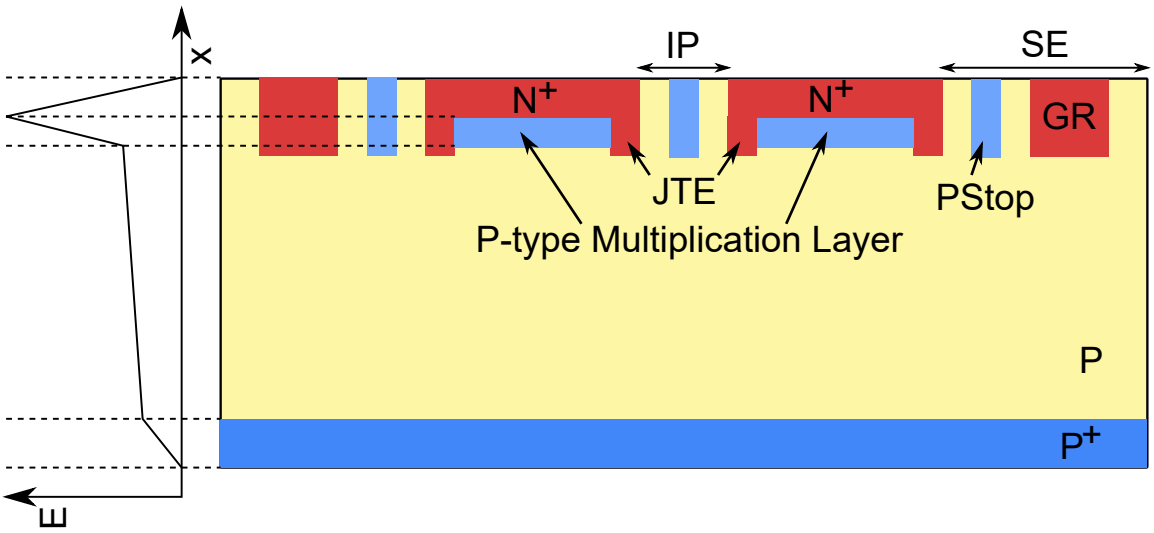

Figure 5.1: Schematic drawing of an LGAD sensor with two pads. The highly p-doped multiplication layer is coloured in light blue. The signal collection electrode is a highly doped n^+-layer. The n^+ JTE surrounds the multiplication layer edge. The low doped p-bulk is shown in yellow. The electric field in dependence on the depth is shown on the left side with a strong field for the junction at the multiplication layer with the electrode.

of going straight from the top to the sensor backside, but are collected around the edge of the multiplication layer. A simulation of the shape of the field lines, with focus on the JTE region are shown in Figure 5.2 for three bias voltages. It is shown in the simulation e.g. for 400 V applied, the field lines approach a more ideal configuration. This effect is reinforced with lower voltages. For 250 V field lies of about 10 µm are affected and for 130 V this extends to about 30 µm. However, these values are approximate and depend on the track direction [44]. More detailed simulations for more realistic doping concentrations and for MIPs passing are needed to understand the sensor behaviour in the no-gain region.

In the classical n-in-p LGAD design, electrons drifting toward the n^+-electrode initiate the multiplication process. Since the total noise in a silicon detector is dominated by the electronic and thermal noise and not by the shot noise, low values of internal multiplication increase the total SNR. This process is therefore different from the use of an external amplifier, where the amplification enhances the signal and the noise equally, without a net improvement [42].

The signals of different types of sensors differ in height or the steepness of the signal, which determines how fast the maximum signal is reached. Thin sensors are used, since the signal steepness mainly depends on the sensor thickness and thin sensors have a faster rising edge than thick sensors. Thereby the timing resolution is improved. However, the

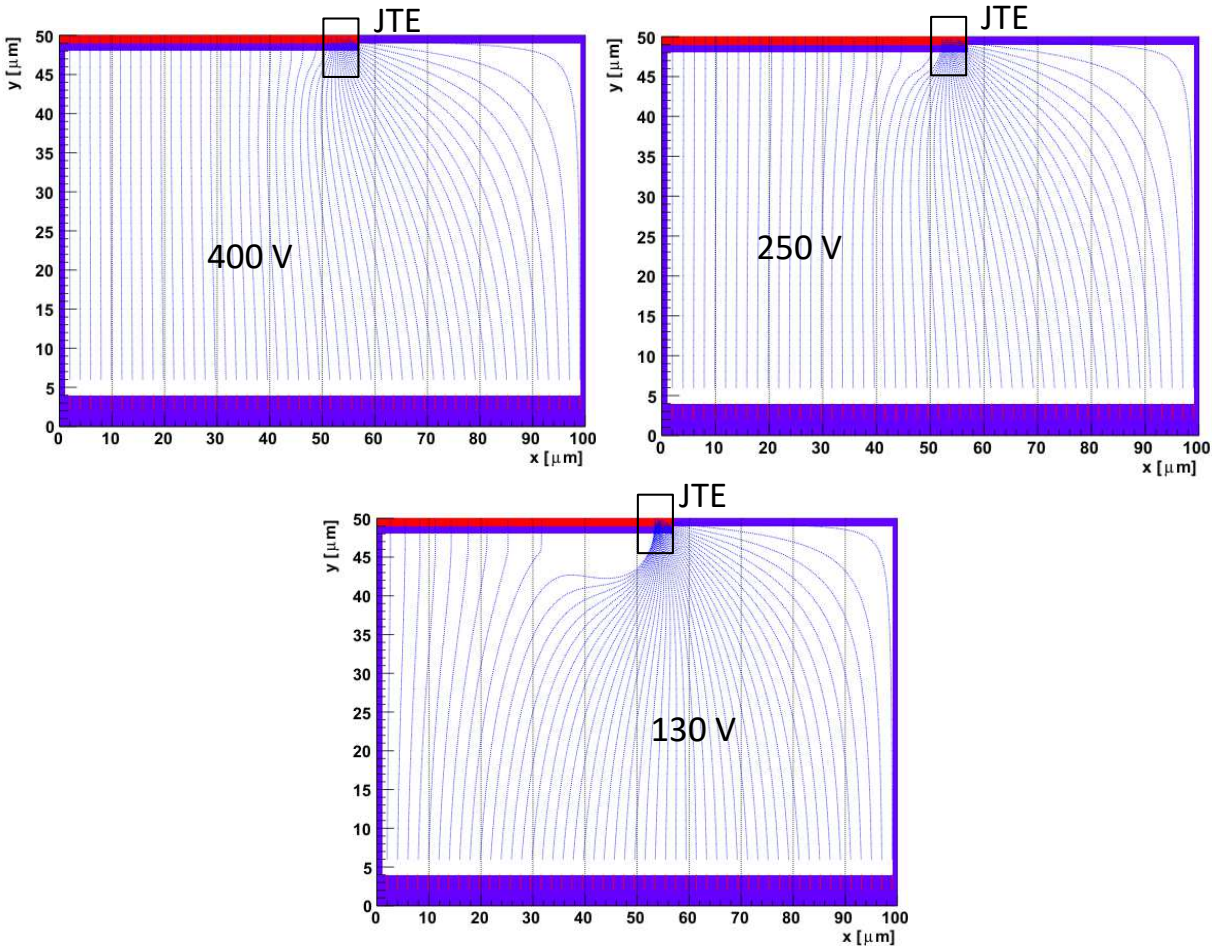

Figure 5.2: Simulations on the influence of the field lines at the JTE for different bias voltages [44]. The simulations were performed for a sensor with a gain layer of 2 µm thickness and a doping concentration of 1×10^{16} cm^{-3} and a doping concentration of 1×15 cm^{-3}.

features of very thin sensors are large capacities and small signals, which then require a gain to generate signals that are large enough to be measured accurately by the read-out electronics. These features also influence the timing resolution, therefore a compromise for the thickness has to be determined. Current experimental testing and simulations indicate that a thickness of ~ 50 µm combined with a gain of ~ 20 provide the best results. Excellent timing resolution can only be achieved if the induced current variations due to non-uniform charge deposition along the particle path, called Landau fluctuations, are minimised and therefore the use of thin devices is required [45].

5.2 Radiation Damage in LGAD Sensors

Irradiation damage in the bulk of the LGAD sensor happens analogue to the radiation damage in silicon sensors without a multiplication layer, as described in Chapter 4, which leads to increased leakage current that can increase the noise. The multiplication layer in an LGAD is impacted by displacement damage leading to a significant decrease in the effective doping concentration in the multiplication layer and with increasing fluence a complete loss of gain can be reached. The cause is the deactivation of boron acceptors in the amplification layer [46, 47]

5.3 Sensor Structure and Production for HGTD

The HGTD sensor parameters and requirements are summarised in Table 5.1. The technology chosen for the HGTD sensors is silicon Low Gain Avalanche Detectors (LGAD) with a baseline active thickness of 50 µm. The thickness was chosen, to obtain the fast rising edge and the therefore improved timing resolution. The granularity is planned to be 1.3 mm ×1.3 mm. This sizing results from a trade off between smaller pads, leading to low occupancy and a small capacitance, thus low electronics jitter, and larger pads, which provide better geometric coverage with large fill factors and less power dissipation from the ALTIROC [5]. The sensor is planned to be of total active size of 39 mm × 19.5 mm with 30×15 pads. The size has been defined to optimise the coverage at the inner radius and to provide a good yield for the sensor production and hybridisation process while keeping the total number of modules equal to 7984 [5]. The final sensor should be bump-bonded to two readout chips (ALTIROC) of 15×15 pads. The inactive edge around the sensor should be less than 500 µm, to maximise the fill factor. The latest developments in HGTD are that the fluence should be limited to 2.5×10^{15} $n_{eq}cm^{-2}$ by replacing the innermost ring two times and an intermediate ring one time. At the end of lifetime, fluences between 1×10^{15} $n_{eq}cm^{-2}$ and 2.5×10^{15} $n_{eq}cm^{-2}$ will be reached, depending on the radius. The maximum leakage current should be less than 5 µA per pad, since that is the ALTIROC leakage current limit, and the applied bias voltage less than 750 V.

The LGAD sensors will be produced in 150 mm wafers, which will be thinned to the total sensor target thickness. The UBM will be deposited on the sensors at wafer level, which is a necessary step before bump-bonding with solder bumps. Afterwards, the wafers will be diced and the sensors will be passed on to hybridization [5].

Topic	Requirement
Granularity	1.3 mm × 1.3 mm
Physical thickness	<300 µm
Active thickness	50 µm
Active size	39 mm × 19.5 mm ≙ 30×15 pads
Inactive edge	<500 µm
Radiation tolerance	5.1×10^{15} $n_{eq}cm^{-2}$
Maximum leakage current per pad	5 µA
Maximum bias voltage	750 V

Table 5.1: Sensor parameters and requirements.[5].

5.4 Sensors for Testing

For this thesis, the sensors provided for testing from Hamamatzu Photonics satisfy the layout requirements of the HGTD. The active thickness was 50 µm, while the total thickness was 300 µm. Additionally, sensors with an active thickness of 35 µm were produced, which are however not covered in this thesis. The layout of a single unit pixel in a sensor for all array sizes was 1.3×1.3 mm^2.

The sensors from HPK are from a shared production between ATLAS and CMS. Sensors with different doping profiles, depth, concentrations, and bulk properties are tested. For testing, sensors are provided as single pads (Figure 5.3), 2×2 (Figure 5.4), 5×5, and 15×15 arrays (Figure 5.5) with HGTD geometry. The sensors are produced with 4 different nominal inter-pad gaps (IP-gaps): 30 µm, 50 µm, 70 µm, and 95 µm, referred to as IP3/5/7/9. Those can be translated into a fill-factor for the HGTD, wherefore the minimal stable IP-gap was determined. Also variations for the slim edge with 200 µm, 300 µm, and 500 µm, referred to as SE 2/3/5 were tested, which as well affect the fill-factor.

The single pad sensors are produced with an opening of 100×200 μm^2 in the Al on the front and 500×1800 μm^2 on the rear, for laser injections. On the front side are two contact areas provided, as shown in Figure 5.3. They are intended for testing purposes and the central round pad for arrays is for the bonding on a PCB with a diameter of 90 µm. The single pad is surrounded with a guard ring, on which several contact pads are provided. The pads are used for IV-measurements and wirebonding. The 2×2 arrays have the same layout on the front as the single pad sensors, shown in Figure5.4. On the rear, the arrays are provided with two opening stripes of 500×3100 μm^2 in the Al. The arrays are surrounded by a guard ring as well. The 15×15 arrays, shown in Figure 5.4, have a size

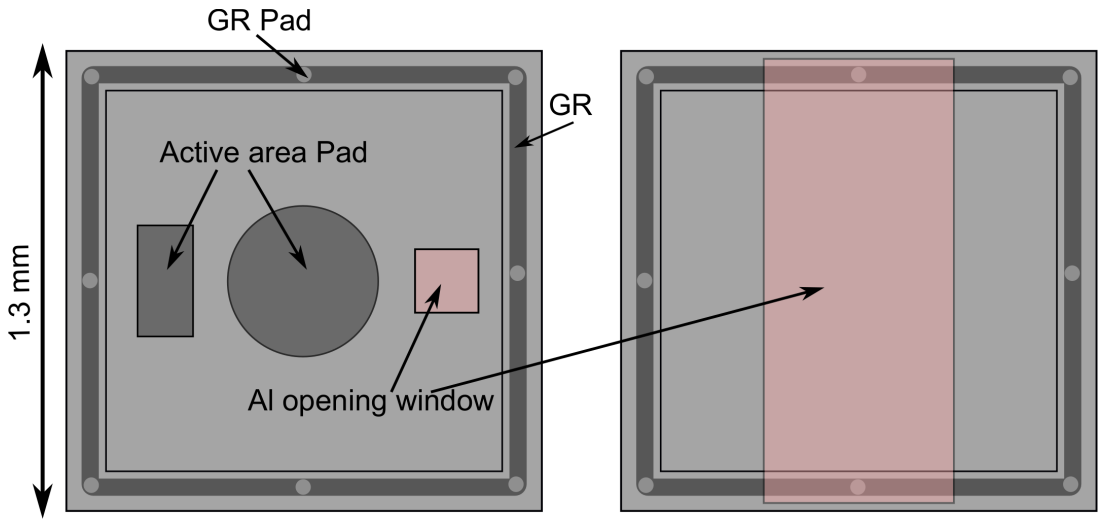

Figure 5.3: Single pad sensor from HPK surrounded by a guard ring with contact pads for probing on the active area and guard ring and an opening in the Al for testing. The opening on the backside is coloured in red. The front of a single pad sensor is shown on the left, the back on the right.

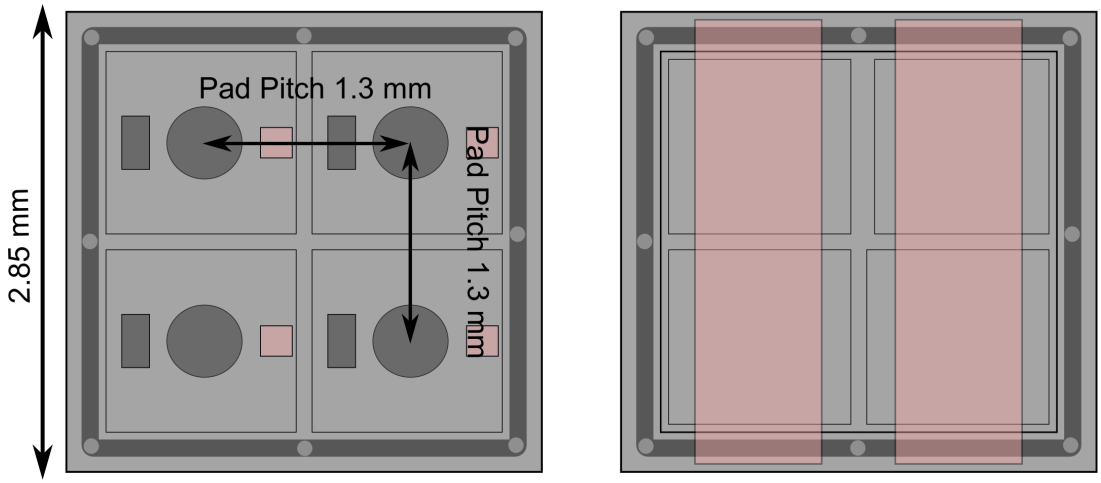

Figure 5.4: 2×2 array from HPK with contact pads for probing on the active area and guard ring and an opening in the Al for testing, marked red. The front of a 2×2 array is shown on the left, the back on the right.

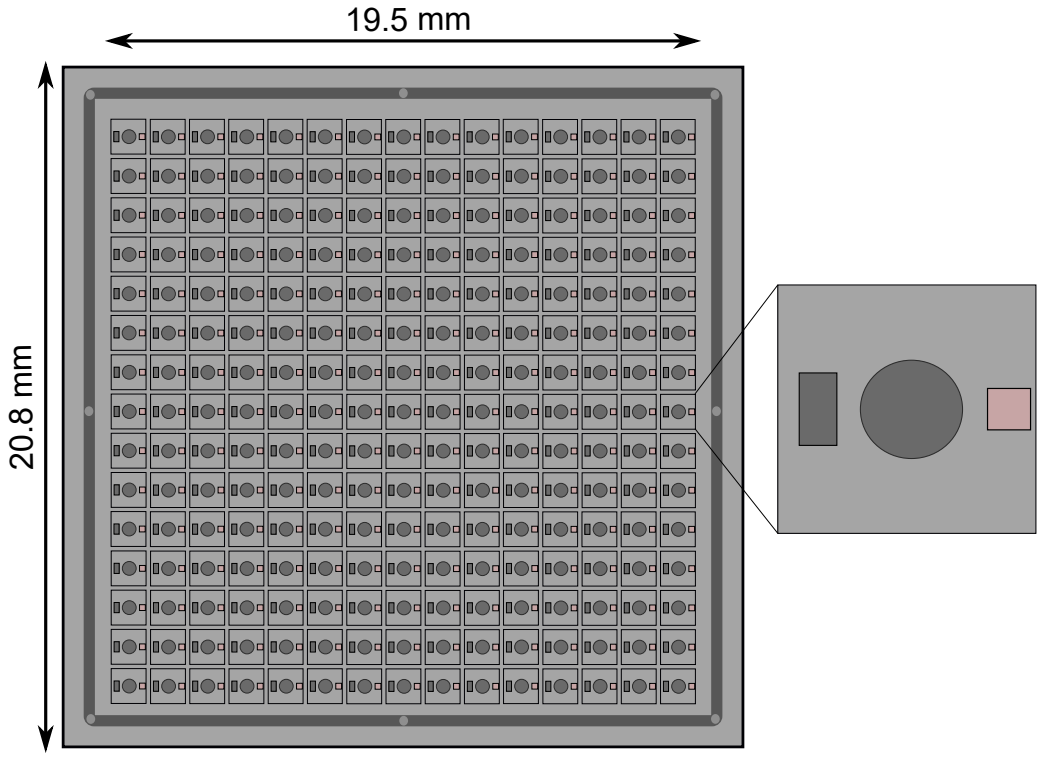

Figure 5.5: 15×15 sensor array from HPK surrounded by a guard ring with contact pads for probing on the active area and guard ring and an opening in the Al for testing. On the right, a single pixel cell is enhanced.

of abound 2×2 cm^2, with a pad pitch of 1.3 mm. The single pixel unit layout is analogue to the single pad sensors. The rear is also equipped with openings in the Al. The 15×15 arrays are also surrounded by a guard ring.

The sensors with an active thickness of 50 µm are provided with two different doping concentrations. However, the exact value are not provided by the supplier. The first, referred to as "Type 3.1", have a gain layer depth of 1.6 µm and a thickness of the high resistivity bulk of 50 µm. The second, referred to as "Type 3.2", have a higher concentration and a deeper doping layer. The gain layer has a depth of 2.2 µm and a thickness of the high resistivity bulk of 50 µm. The properties are summarised in Table 5.2.

Type	Thickness	Gain layer	Bulk
3.1	50 µm	1.6 µm thickness	High resistivity
3.2	50 µm	2.2 µm thickness, deeper doping layer than Type 3.1	High resistivity bulk

Table 5.2: Summery of the different doping layers properties and bulk properties for the provided for the provided prototypes from HPK.

6 Sensor Testing Methodology and Results: Current-Voltage Characteristics

This chapter is devoted to the description and systematic comparison of the current-voltage (IV) characteristics of unirradiated, irradiated and annealed LGAD arrays and single pads. For the LGAD sensor, five aspects were examined: Homogeneity, yield, demonstration of large sensors, fill-factor, and radiation hardness. With the IV-curves information on the homogeneity, the yield, radiation damage and the feasibility of large sensors could obtained. Further measurements on the fill-factor, and radiation damage are presented in Chapter 7.

6.1 Experimental Set-up

A semi-automatic probe-station was employed to measure the leakage current in dependence on the applied voltage. The probe-station provided a light-tight environment to avoid ambient light affecting the measurement through a photocurrent. In the probe-station was a movable chuck to which a high voltage was applied by a Keithley 2410 high voltage source. The chuck was connected to a chiller for cooling and contains a vacuum suction mechanism to secure sensors during measurements. One or more needles, up to 5, were placed on the sensors metallised testing pads. The needles were connected to a Keithley picoamperemeter 6487 or a Keithley 2410 to measure the leakage current for the applied voltage.

Additional devices connected to the program were temperature sensors on the chuck and in the probe-station, as well as a sensor for the relative humidity. The dew-point in the probe-station was calculated in the program to avoid condensation or freezing on the tested sensor when cooled.

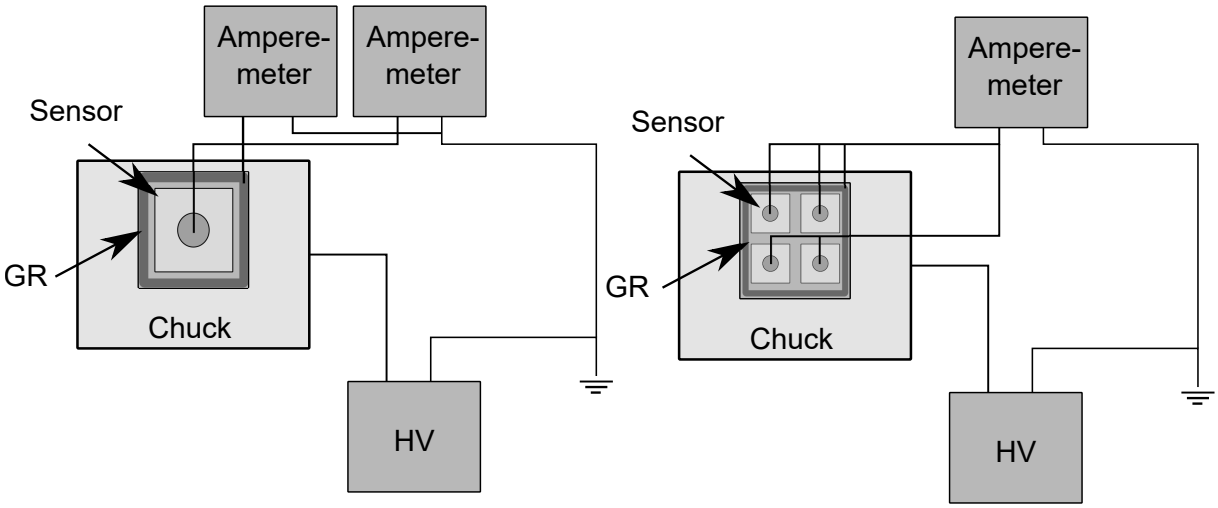

Figure 6.1: Schematic drawing of the measurement set-up in the probe-station with the HV-source and the amperemeter. A single pad sensor with a needle connected to the sensor pad and one needle connected to the guard ring (GR) (left) and a 2×2 array with alls four pads and the guard ring connected to the amperemeter (right).

The voltage was applied to the chuck, through which the sensor was reverse biased. Meaning that the chuck was set to a more negative voltage. The picoamperemeter measured the current drawn through the sensor. The voltage sweep technique was used, measuring in steps of 5 V the leakage current at each step after a wait time of 500 ms.

For measurements on a single pad, two needles were used, shown in Figure 6.1. The first one was connected to the central pad of the sensor, and the second one was connected to the guard ring. Both currents were measured individually at each step with two separate amperemeters. For measurements of 5×5 and 15×15 arrays, the needles were connected to just one pad with one needle. The pad was measured like a single pad with the voltage sweep technique and afterwards, the needle was separated from the sensor and placed on the next pad in the row. The process was repeated for every pad in the row. When the row was finished, the needle was repositioned at the first pad in the second row, starting with the same process as in the previous row. The measurement was continued until all pads on the sensor were measured. For measurements of 2×2 arrays, two different configurations for the needles were used. The first measurement was similar to the process described for the 5×5 and 15×15 arrays. The second used five needles with whom every pad of the array was connected at the same time, and one needle was connected to the guard ring. The combined current of all four pads and the guard ring was measured, which corresponds to the current of 4 pads and the guard ring, shown in Figure 6.1.

6.2 Environmental Studies

Environmental studies were performed, to ensure that the measurement set-up was fully understood and fluctuations in measurement results could be explained or environmental factors could be excluded.

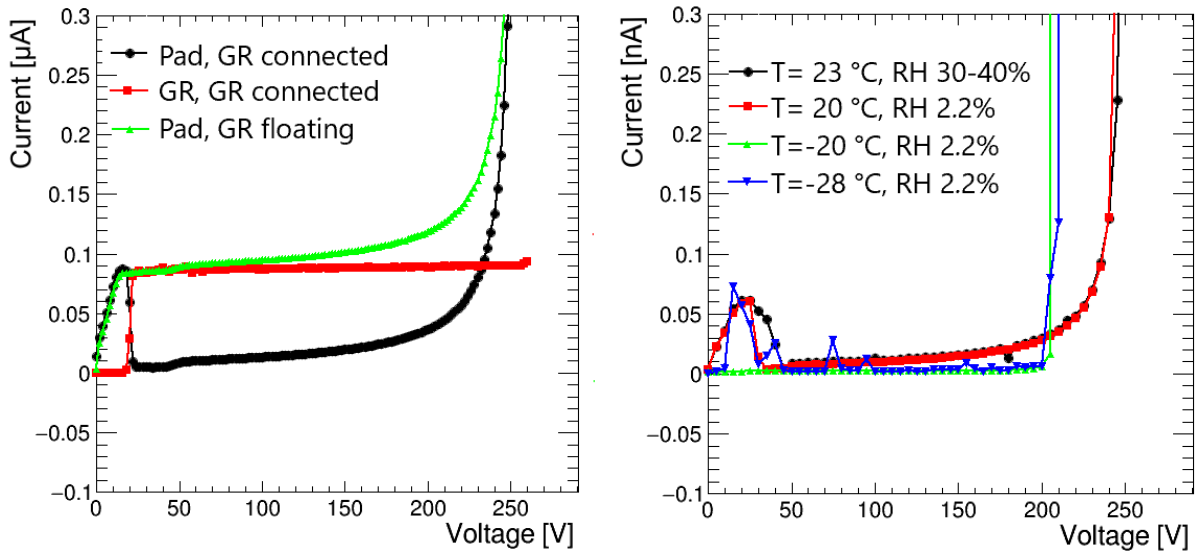

Figure 6.2: IV-curves for the single pad sensor W8-LG1-SE5-P4 of "Type 3.1", with grounded guard ring and floating guarding (left). The same sensor measured at 20 °C and cooled down to -20 °C and -28 °C. Additional measurements for two different relative humidities at 20 °C are shown (right).

For environmental studies, the single pad sensor W8-LG1-SE5-P4 was measured with and without the guard ring (GR) connected to ground. The measurement results are shown in Figure 6.2. The breakdown voltage (V_{BD}) for unirradiated sensors was defined as the voltage at which a current of 1 µA was reached. It was tested whether the connection of the guard ring influenced the V_{BD} for a single pad sensor. The graph shows that the V_{BD} was not affected by the connection of the guard ring. For both configurations the V_{BD} was approximately 250 V. However, the currents measured for the pad varied significantly for the different configurations. For the measurement with guard ring and pad connected, the pad current was 0.4 nA and the guard ring current was 0.9 nA at 80 % of the breakdown voltage. Also, a switch in the pad currents and guard ring current at the start of the measurement was observed. It is still under investigation, whether it was a real effect or an artefact from the measurement set-up — however, the current behaviour with and without the guard ring connected became equal after 20 V. For the measurement without

the guard ring connected, the pad current was 0.12 nA at 80 % of the V_{BD}. Accordingly, the current of the pad without the guard ring connected was roughly the sum of the pad and guard ring current when both were connected, which could be explained by a reach-through effect of the depletion zones. All in all, both measurements indicate low currents in the sub nA range.

Additionally, the influence of the temperature and the relative humidity on the current behaviour of the sensor was tested with the guard ring connected. The temperature dependence of the current level was studied, as shown in Figure 6.2. At 20 °C, the breakdown voltage was at 250 V with a current with a current of 0.04 nA at 80 % of the breakdown voltage. With a decrease in the temperature to -28 °C, the breakdown voltage decreased to 210 V and the current at 80 % of the breakdown voltage decreased to 0.003 nA. The decrease in current was caused by the decrease of thermal leakage current, as explained in Chapter 4.3. The decreased temperature also increased the gain of the multiplication layer in the sensor, hence the earlier breakdown.

Also, the dependence on the relative humidity was studied, shown in Figure 6.2. For a relative humidity of 30-40 %, the measured current at 80 % of the breakdown was 0.04 nA. The humidity was fluctuating during the measurement on the probe-station since the probe-station was not airtight and the flushing with dry air had to be turned off. The measurement at a relative humidity of 2.2 %, which is the lowest reached relative humidity in the probe-station, showed a current of 0.04 nA at 80 % of the breakdown voltage. Therefore, no dependence for the breakdown voltage and the current level on the relative humidity was observed.

The results of the environmental studies were taken into account for the sensor testing and the temperature, as well as the relative humidity, were observed closely for all measurements.

6.3 Studies on the Sensor Properties of "Type 3.1" and "Type 3.2"

Sensors of "Type 3.1" and "Type 3.2" were measured and compared for varying arrays sizes. For the estimation of the systematic uncertainty, a single pad sensor of "Type 3.1" was measured. For each voltage step, the current was measured ten times. The measured standard deviations were independent of the current level at 0.05 nA which is used as an estimate of the systematic uncertainty. However, for most measurements, the uncertainty is not visible in the graphics.

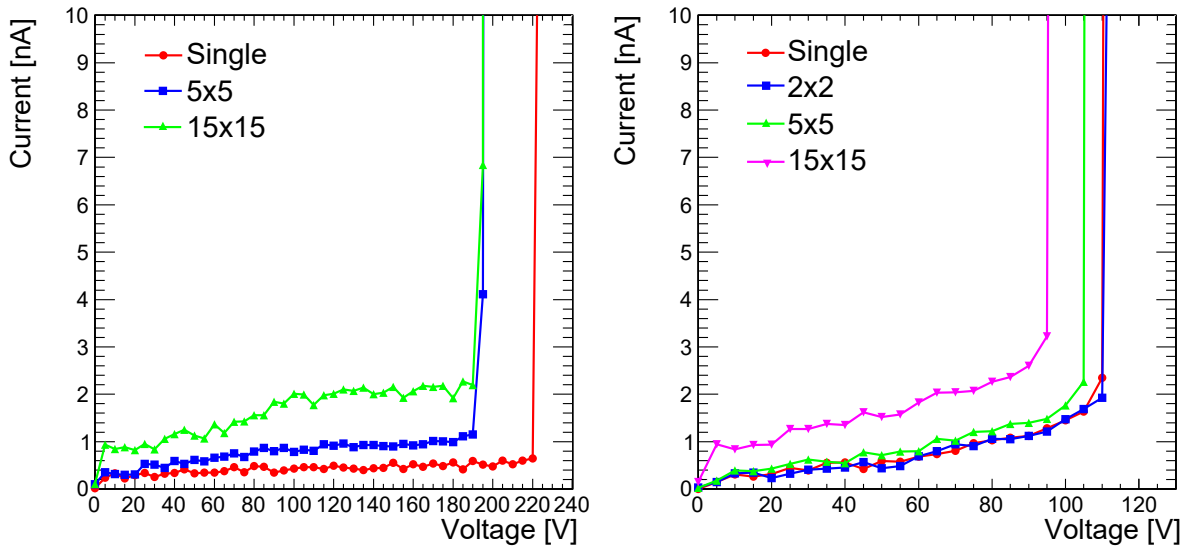

Figure 6.3: Comparison of IV-curves of single pad sensors, 5×5, and 15×15 measurements "Type 3.1" (left) and IV-curves of single pad sensors, 2×2, 5×5, and 15×15 of "Type 3.2" (right).

IV-measurements of a single pad sensor, a 2×2, a 5×5, and a 15×15 arrays were performed, shown in Figure 6.3. Up to 30-50 V, the thin highly-doped p-type multiplication layer was slowly depleted, then within a few volts, the remaining high-resistivity bulk was fully depleting. Before irradiation, the current was at the sub-nA level after full depletion for the single pad, the 2×2 arrays, and the 5×5 array. The current never reached a plateau and kept increasing due to the charge multiplication, before it reached a hard break down at about 220 V for "Type 3.1" or 110 V for "Type 3.2", shown in Figure 6.3. The difference in the gain layer is caused the difference in the V_{BD}. The deeper and higher doped multiplication layer of "Type 3.2" amplified the charges from the leakage current more, therefore generated a higher current and caused an earlier breakdown.

The measurements of single pads were compared to measurements of 2×2, 5×5, and 15×15 arrays, shown in Figure 6.3. For "Type 3.1", no 2×2 array was measured because no array of the same wafer as the other arrays was available. For the measurements of "Type 3.1", sensors of wafer 8 (W8) were measured. A shift in the V_{BD} of the from the single pad measurement, with 245 V, to the measurement of the 5×5 array, with 220 V, and the 15×15 array, with also 220 V, was observed. The V_{BD} is not readable in Figure 6.3, because it was zoomed in to make the difference in the current levels visible. For "Type 3.2", here sensors of wafer 18 (W18), the V_{BD} shows a similar shift to the arrays of "Type 3.1". However, no shift from the single pad to the 2×2 V_{BD} is shown, with both breaking down at 130 V. The shift of the V_{BD} from the 2×2 array to the 5×5 array is smaller than for the arrays of "Type 3.1", with a V_{BD} of 125 V. The final V_{BD} of the 15×15 array is at 120 V. Also, for the sensors of "Type 3.2" the V_{BD} is not shown in Figure 6.3, because it was zoomed in to make the difference in the current levels visible.

6.4 Homogeneity Measurements

Additional, homogeneity studies, yield studies, and demonstrations of the functionality of large sensors were performed. For the homogeneity studies, 5×5, and 15×15 arrays of unirradiated "Type 3.1", and "Type 3.2" were measured. The 5×5, and 15×15 arrays measured were all featured with an inter-pad gap of 95 µm, and a slim edge of 500 µm.

The homogeneity was evaluated for several aspects. The first is the V_{BD} of a single array. As an example of the homogeneous behaviour, the 15×15 array of "Type 3.2", from wafer 18, is shown in Figure 6.4. The mean of the breakdown voltage was $\overline{V_{\mathrm{BD,\,W18}}} = 125.4$ V with a standard deviation of $\sigma_{\mathrm{VBD,\,W18}} = 0.4$ V. The small fluctuation in V_{BD}, which is expressed in the standard deviation, but also shown in the visual representation in the bottom right plot in Figure 6.4, shows the homogeneous behaviour of unirradiated sensors of "Type 3.2".

Another aspect for the evaluation of the homogeneity was the currents of the individual pads of the array. The current was taken at 80 % of the V_{BD}, with an average current of 2.49 nA with a standard deviation of 0.04 nA. The fluctuations were dominantly caused by an increase in the currents towards the edges. This increase in the currents was an

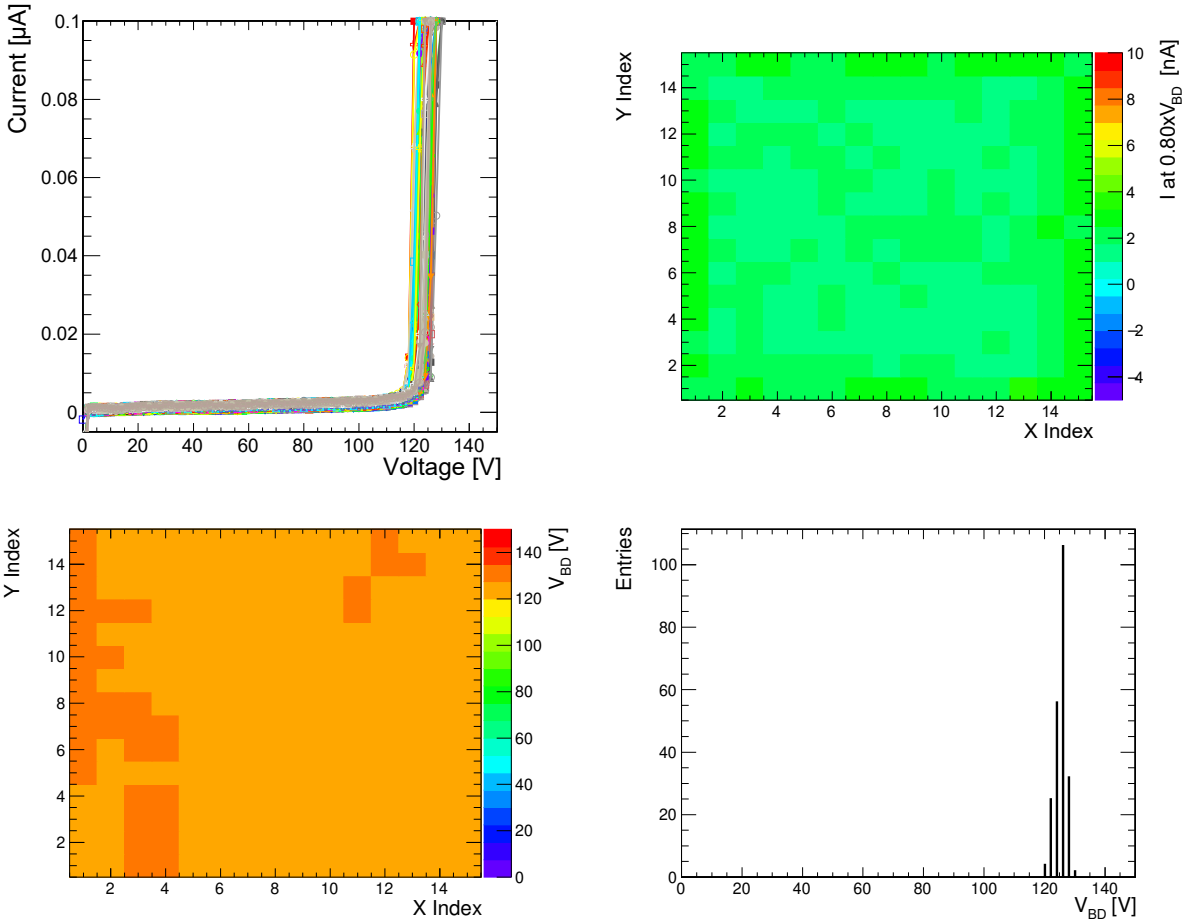

Figure 6.4: On the top left, the IV-curves of all pads of the 15×15 array of wafer 18 with an inter-pad gap of 95 µm, and a slim edge of 500 µm of set P2 are shown. The top right plot is a 2D plot of the currents at 80 % of the breakdown voltage. The bottom left plot shows the breakdown voltage of the sensor as a 2D plot and the bottom right plot shows a histogram of the breakdown voltage.

artefact from the measurement configuration since the guard ring and neighbouring pads were floating for all array measurements. Thereby its direct neighbours influenced the measured pad. The effect was not observes this distinct for measurements with a probe-card, where all pads and the guard ring were contacted and measured at the same time. Therefore, the increased currents were an artefact from the measurement method used during this thesis.

Conclusively, the sensor measurements showed a good homogeneity in terms of V_{BD} and current level. This behaviour was representative for the other measured 15×15 arrays of "Type 3.2". The homogeneity in the V_{BD} and the current is essential to ensure a uniform response across the entire sensor. Additionally, the sensors are only suitable for the

HGTD, when all pads showed a reasonable high V_{BD} to provide full depletion.

As an example for the homogeneity behaviour of the 15×15 arrays of "Type 3.1" a sensor of wafer 8 was chosen, shown in Figure 6.5. The behaviour was representative of the other good sensors tested for "Type 3.1". The breakdown voltage showed a similar behaviour to the sensors for "Type 3.2", but at a higher breakdown voltage, since the mean breakdown voltage was $\overline{V_{\mathrm{BD,\ W8}}} = 192.65$ V with a standard deviation of $\sigma_{\mathrm{VBD,\ W8}} = 0.06$ V. The current showed the same behaviour to the sensors of "Type 3.2", with pads with increased currents towards the edge as an artefact from the measurement technique. The average current over the sensor at 80 % of the breakdown voltage was 3.52 nA with a standard deviation of 0.05 nA.

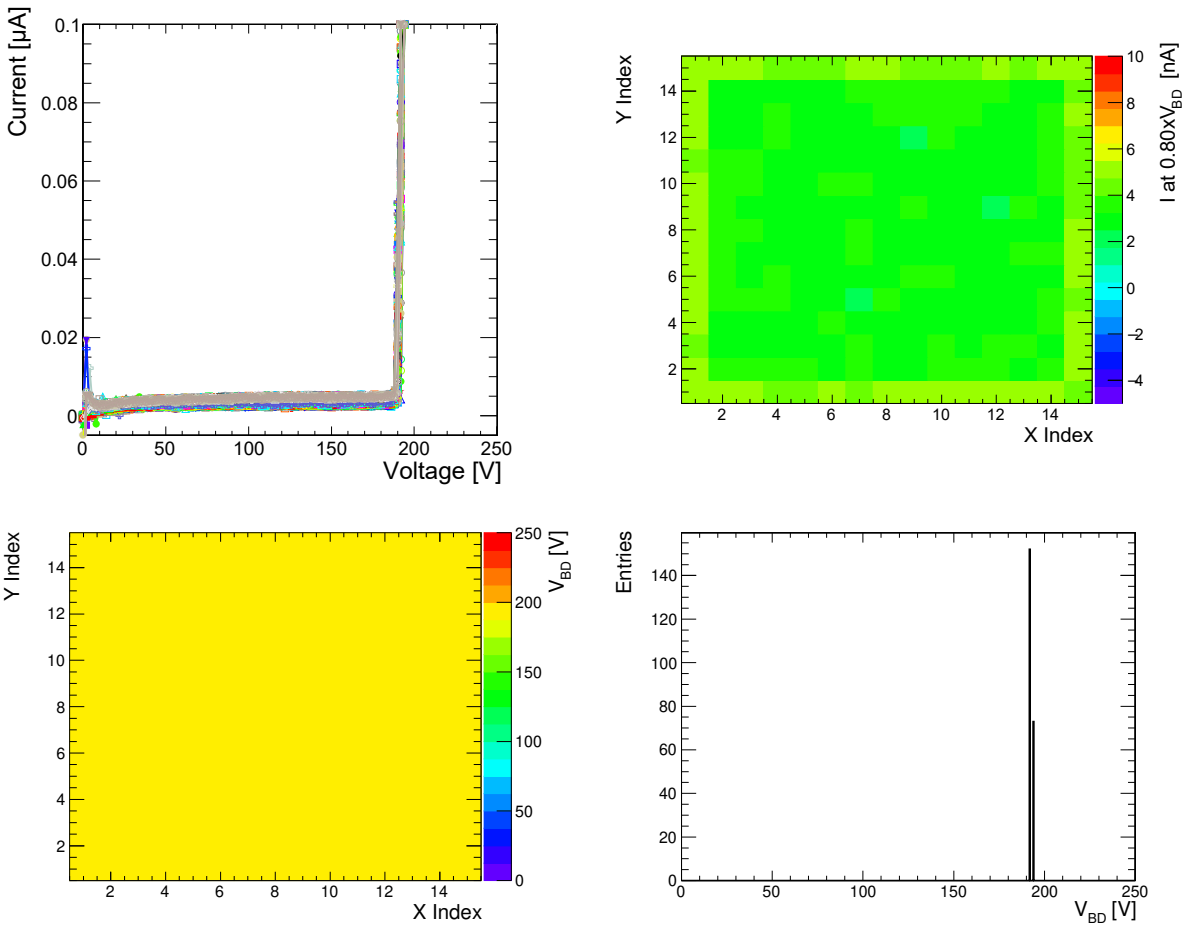

Figure 6.5: The complete analyses of the measurement of W18-LG15x15-SE5-IP9-P3 sensor. On the top left, the IV-curves of all pads of the sensor are shown. The top-right plot is a 2D plot of the currents at 80 % of the V_{BD}. The bottom left plot shows the V_{BD} of the sensor as a 2D plot, and the bottom right plot shows a histogram of the V_{BD}.

Also, the homogeneity of the whole test batch of the “Type 3.2“ and “Type 3.1“ sensors was tested. The average breakdown voltage over all tested “Type 3.2“ sensors was at $\overline{V_{\text{BD, Type 3.2}}} = 127\,\text{V}$ with a standard deviation of $\sigma_{\text{VBD, Type 3.2}} = 5\,\text{V}$. For the “Type 3.1“ sensors, the average breakdown voltage was $\overline{V_{\text{BD, Type 3.1}}} = 200\,\text{V}$ with a standard deviation of $\sigma_{\text{VBD, Type 3.1}} = 8\,\text{V}$.

The current behaviour was the other aspect. Here, the shown behaviour of the example sensors was representative for the other good sensors tested of the 15×15 arrays of “Type 3.2“ and “Type 3.1“. They all showed increased currents towards the edge with an average current of around 4 nA and a standard deviation of 1 nA for “Type 3.2“ and 5 nA and a standard deviation of 2 nA for “Type 3.1“.

6.5 Yield

One of the aspects studied was the yield of the arrays, which indicated the quality of the sensors provided by the supplier and the feasibility of large sensors. For this purpose, the yield for the 5×5 and 15×15 arrays of “Type 3.2“ and “Type 3.1“was determined. The results are summarised in Table 6.1. Two different aspects were evaluated. The yield of individual pads in arrays. A pad is labelled as bad if the individual pad breaks down before a voltage of 90 % of the mean V_{BD} was reached. As shown in Table 6.1, for the 5×5 arrays all pads in the arrays performed well for “Type 3.2“ and “Type 3.1“. For the 15×15 arrays of “Type 3.2“ 99.83 % pads were good and for the “Type 3.1“ 99.93 % were good.

The second aspect was the full-array yield. The sensor array was labelled as bad if at least one pad was bad. This strict demand on the quality of the sensor arrays was based on the assumption for production that the sensor connection to the readout via bump-bonds could not exclude specific pads due to the mass production aspect for HGTD. Therefore, only perfect sensors with all pads with a reasonably high breakdown could be used for the HGTD. For the 5×5 arrays of “Type 3.2“ and “Type 3.1“, both measured sensors performed well with 100 % good sensors each. For the 15×15 arrays of “Type 3.2“ 78.57 % of the sensors performed good, and for “Type 3.1 “ 84.62 % of the sensors performed good, in terms of breakdown voltage.

Two of the 28 tested 15×15 sensors were produced without under-bump metallisation (UBM). Those were two sensors of wafer 18 (W18), but they demonstrated no significant

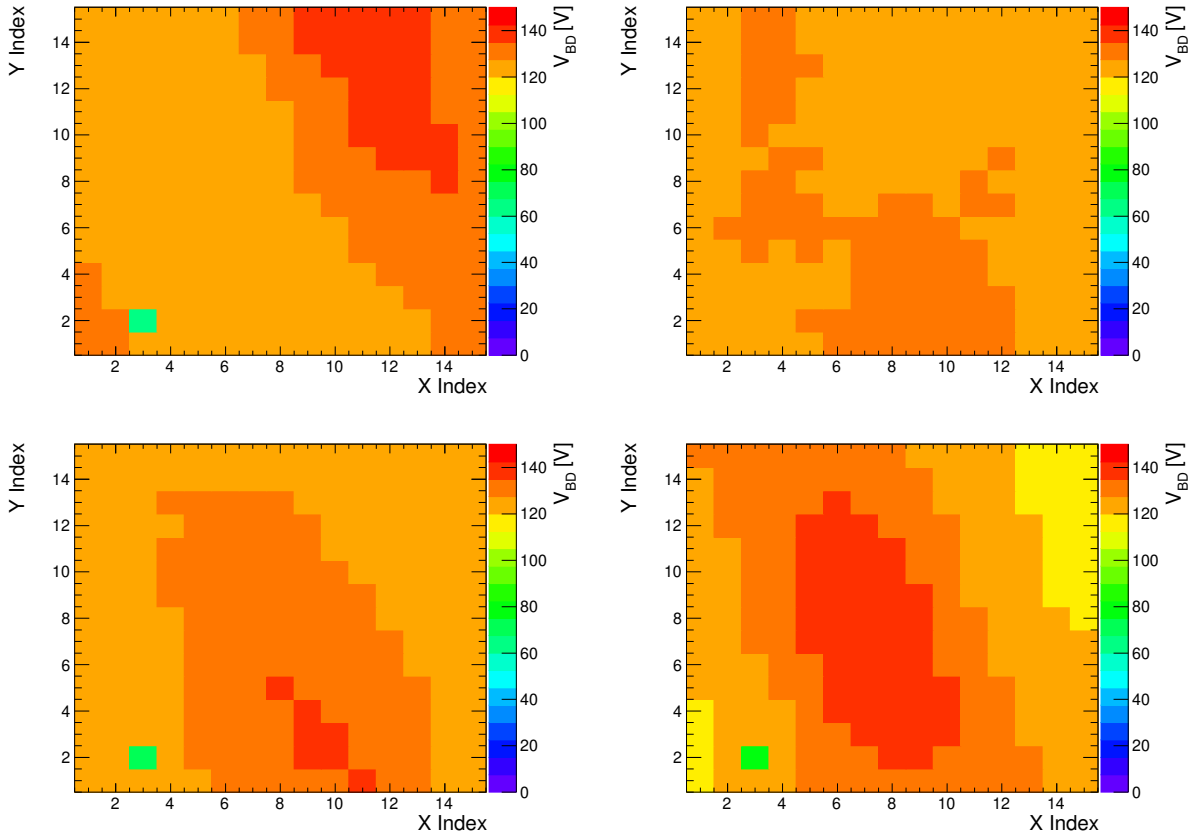

Figure 6.6: 2D maps of four of the measured 15×15 arrays of "Type 3.2"of set P1. Three out of the four tested sensors, show the same pad (X3-Y2) with an early breakdown. Top left W11, top right W12, bottom left W13, bottom right W14.

different behaviour to the sensors with UBM in V_{BD}, current level or production quality. One feature noticed during the measurements of 15×15 arrays of "Type 3.2" was one pad with an early breakdown at the same position for sensors, which were all at the identical position of the mask of the P1 sets. The pattern is shown in Figure 6.6. This one bad pad is believed to be caused by the production process. During the implementation of the multiplication layer, a presumed error in the masking is the most probable cause for this pattern. Subsequent from this assumption, the data was updated excluding the P1 sets, listed in Table 6.1. Without the P1 sets, the number of tested 15×15 arrays decreased from 28 to 23, but the fraction of perfect sensors increased from 78.57 % to 91.30 %.

Overall, a good fraction of good sensors based on low currents and uniform breakdown voltage was observed. The current levels were low, with an average of 3.85 nA and a standard deviation of 1.22 nA. For the measured sensors, a high proportion of good large sensors was observed, and the general feasibility of large sensors like the 15×15 arrays

was demonstrated.

Type	3.2			3.1	
Sensor	5×5	15×15 all	15×15 w/o P1	5×5	15×15
Number of Sensors tested	1	28	23	6	26
Pads tested	25	6300	5175	150	5850
Number of perfect sensors	1	22	21	6	22
Number of good pads	25	6289	5166	150	5819
Fraction of perfect sensors [%]	100 ± 5.56	78.57 ± 7.61	91.30 ± 6.27	100 ± 1.22	84.62 ± 7.11
Fraction of good pads [%]	100 ± 0.13	99.83 ± 0.06	99.83 ± 0.06	100 ± 0.01	99.47 ± 0.11

Table 6.1: Table of the summarised results on the array testing for HPK of "Type 3.2", with an added column for the sensors without the P1 sets, since a presumed production error in this set influenced the sensor performance.

6.6 Measurements on the Influence of Inter-Pad Gap and Slim Edge on the V_{BD}

A set of 14 2×2 arrays of "Type 3.2" were measured to test whether variations of the SE and IP gap showed an effect on the sensor performance. The measurements were performed with five needles. One needle contacting the guard ring and the other four contacted one pad each.

The set contains one PIN-diode, which was not considered in the evaluation. Additionally, five sensors have an SE5-IP9 without UBM and one with UBM. The remaining sensors were produced with UBM, one each: SE3-IP9, SE2-IP9, SE5-IP7, SE5-IP5, SE5-IP3, SE3-IP7 and SE3-IP5.

Every sensor was measured as described before, and then the average overall measured pads was calculated, resulting in

$$\overline{V_{\mathrm{BD}}} = \frac{1}{N \cdot 4} \sum_{\mathrm{i}=1}^{N} \sum_{\mathrm{j}=1}^{4} V_{\mathrm{BD,i,j}} = 115.96 \text{ V}. \tag{6.1}$$

The average breakdown voltage $\overline{V_{\mathrm{BD}}}$ was calculated over the breakdown voltage V_{BD} for the number of pads j per sensor i, which were for the 2×2 arrays 4 per sensor, and the number of sensors N. For the uncertainty, the standard deviation was calculated. Analogue, the average breakdown voltage was determined, separated by the sensor parameter SE and IP. The measurements were performed in steps of 5 V. To improve the accuracy, the measured values were linearly interpolated, and the x-axis value where the interpolation intersects with 1 µA was selected as the V_{BD}. The summarised results are shown in Table 6.2. There, a slight decrease in the V_{BD} with a decreased IP is noticeable: From $V_{\mathrm{BD,\,IP9}} = (116.56 \pm 0.41)$ V to $V_{\mathrm{BD,\,IP3}} = (110.00 \pm 1.32)$ V. However, there seems to be no significant dependence of the V_{BD} on the SE configuration. Nonetheless, based on the small sample size, this has to be re-evaluated after more measurements were performed.

	Number Sensors N	Average V_{BD} [V]	Std. Dev. of Mean [V]
All	13	115.96	0.39
SE5	9	115.88	0.49
SE3	3	115.83	0.56
SE2	1	118.75	1.25

	Number Sensors N	Average V_{BD} [V]	Std. Dev. of Mean [V]
IP9	8	116.56	0.41
IP7	2	117.5	0.95
IP5	2	115	0.98
IP3	1	110	1.32

Table 6.2: Table of V_{BD} of the set of the 2×2 arrays of wafer 12. The Sensors are separated on the left by the SE and on the right by the nominal IP-gap.

6.7 Measurements on Irradiated Sensors

For the measurements on irradiated sensors, 2×2 arrays of "Type 3.2" were used. The sensors were irradiated with a fluence of $1.5 \cdot 10^{15}$ $\mathrm{n_{eq}/cm^2}$. The sensors were irradiated at the JSI TRIGA-Mark-III reactor in Ljubljana. For the irradiated sensors, the measurements were performed cooled, since the leakage current increased with irradiation but could be reduced by cooling, as explained in Section 4.4.

6.7.1 Comparison of Irradiated and Unirradiated Sensors

In Figure 6.7 the sum of the current of four pads and the guard ring of an unirradiated and an irradiated 2×2 arrays are shown. The compliance current for the unirradiated sensor was set to 0.5 µA. For the irradiated sensor, the compliance current was set to 10 µA, because of the increased current level. For the measurements of the unirradiated, as well as for the irradiated sensors, a large increase in the current for an increased bias voltages was shown, partially due to the increased gain.In standard silicon sensors without gain,

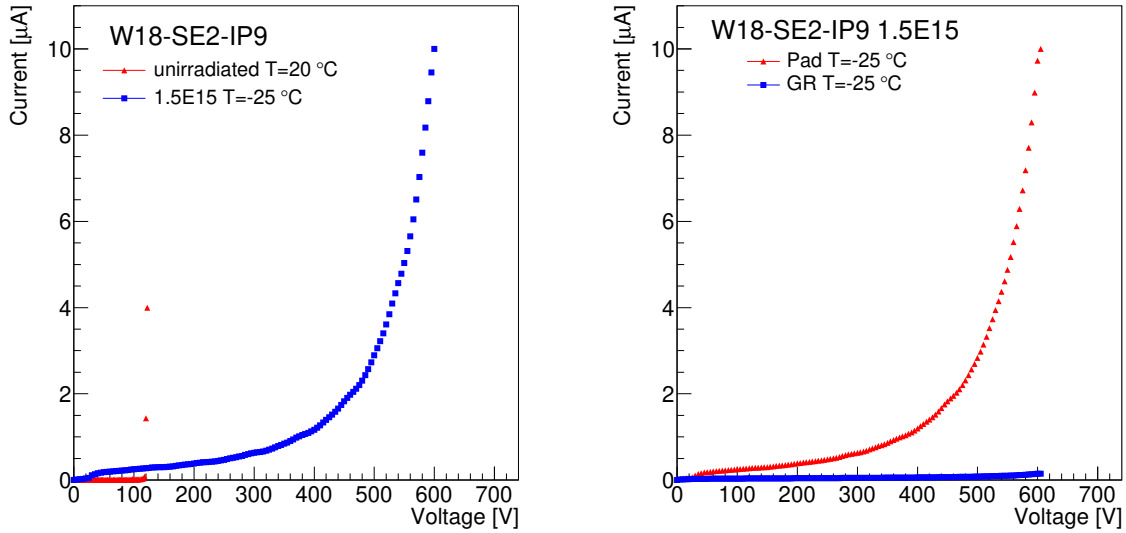

Figure 6.7: Comparison of IV-curve of the unirradiated 2×2 array W18-LG2x2-SE2-IP9-P2 and the irradiated 2×2 array W18-LG2x2-SE2-IP9-P1 with a irradiation fluence of $1.5 \cdot 10^{15}$ $n_{eq}cm^{-2}$ (left). For both measurements, the sum of the currents of the four pads and the guard ring were measured. Also, the IV-curves of the individual currents for the four pads and the guard ring (right).

the leakage current originates from the volume generation current caused by radiation-induced defects and increases linearly with fluence, as explained in Chapter 4. However, for LGADs the situation is more complicated due to the gain and its fluence evolution. The multiplication layer leads to an increase of the leakage current, which is given by the product of the volume generation current and the gain factor. As the gain decreases with irradiation, the leakage current does not necessarily increase monotonously with fluence at the same, since only one fluence was measured for the irradiated sensors this could not be investigated closer.

The unirradiated sensor broke down much earlier, at 120 V, than the irradiated sensor, at 560 V. Here the breakdown definition for the unirradiated sensor was kept at the voltage at which the sensor reaches 1 µA. For the irradiated sensor, the breakdown definition was changed to 5 µA per pad and four pads were measured together. Therefore the breakdown voltage was defined at the voltage where the sensor reaches 20 µA. The change in the V_{BD} was was related to the reduced gain due to radiation damage. Additionally, the current level of the guard ring was measured and compared to the currents of the pad, shown in Figure 6.7. The current at 80 % of the V_{BD} of the pad is at 2.31 µA and for the guard ring 0.07 µA. Additionally, the current for the guard ring never rose above

0.15 µA. Therefore the guard ring current was neglectable for measurements with all four pads measured after irradiation.

6.7.2 Comparison between Probe-station Measurements and Measurements in the Climate Chamber

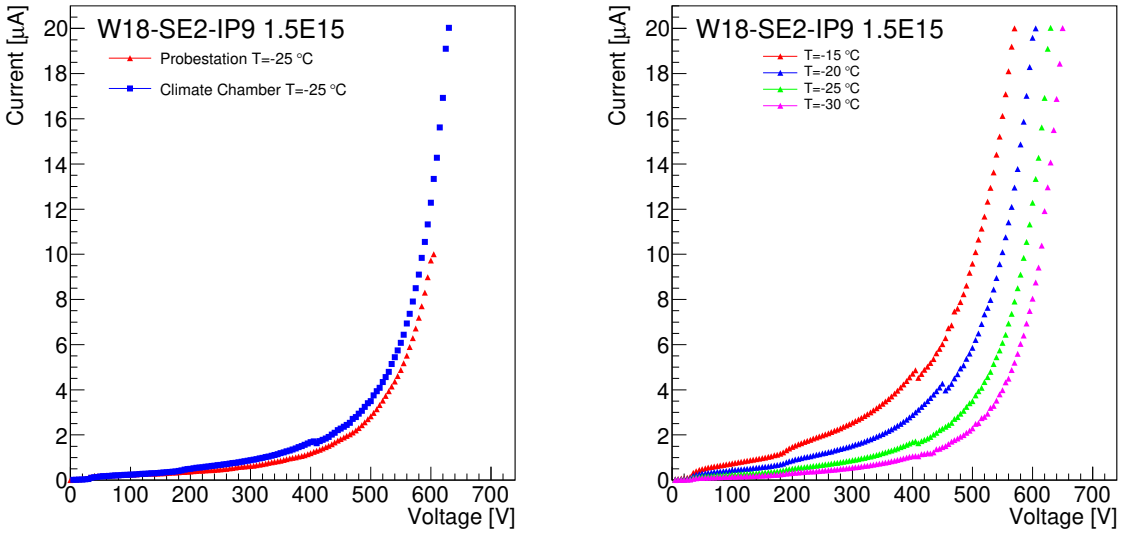

Figure 6.8: IV-curves of the 2×2 arrays W18-LG2x2-SE2-IP9-P1. Comparison between the measurement on the on the probe-station and in the climate chamber at -25°C (left) and four different temperature measurements on the probe-station (right). The currents were measured for all four pads and the guard ring.

For the irradiated sensors, measurements on the probe-station were performed as well as measurements in a climate chamber. In the climate chamber, the sensors measured were mounted on a TCT-PCB with the pads and the guard ring wire bonded to the signal outputs. Therefore, both measurements were compared for the combined currents of the four pads and the guard ring. The results are shown in Figure 6.8.

The current levels for both measurements agree within 0.3 µA, but the probe-station measurement seemed to have been performed at a slightly lower temperature than the measurement in the climate chamber. The temperature difference can be calculated by [48]:

$$I(T) \propto T^2 \cdot \exp\left(\frac{-E_{\text{eff}}}{2k_{\text{B}}T}\right) \tag{6.2}$$

$$\frac{I(T)}{I_0(T)} = \left(\frac{T}{T_0}\right)^2 \cdot \exp\left(\frac{E_{\text{eff}}}{2k_{\text{B}}}\left(\frac{1}{T_0} - \frac{1}{T_0}\right)\right) \tag{6.3}$$

with the Boltzmann-constant k_B, and the effective bandgap E_{eff} in silicon with a value of 1.21 eV, the current for the climate chamber I_0 and the temperature of the probe-station T_0 with -25 °C. The current of the probe-station is I and the temperature for the protestation measurement T. From the calculation, a temperature of $T = -27.8$ °C for the probe-station measurement could be determined, at 500 V with a current of 3.5 µA measurement for the climate chamber and 2.83 µA for the probe-station. Since the changing temperature influences the gain, the result is not entirely accurate, but a good approximation. The results seem reasonable because the chuck in the probe-station was always cooled a few degrees below the desired temperature for the reason that the temperature sensor would read a higher temperature than the set one. It was believed, this was due to a worse cooling performance of the chiller than set nominal. Based on the measurement, the thermo-conductive connection of the measured sensor in the probe-station should be investigated, and the temperature sensor should be recalibrated. Another possible reason could be self-heating of the sensor on the PCB in the climate chamber since the thermal constant to the cooling medium was worse than on the cold chuck.

6.7.3 Measurements on the Temperature Dependence of the Current of Irradiated Sensors

Additional measurements on the temperature dependence of the irradiated sensor were performed in the climate chamber. Four temperatures were measured: -15 °C, -20 °C, -25 °C, and -30 °C. The resulting IV-curves are shown in Figure 6.8. With decreasing temperature, the leakage current decreased, and the breakdown shifted slightly. The current at 80 % of the breakdown voltage decreased from 6.3 µA at -15 °C to 2.8 µA at -30 °C.

In the IV-curves measured at -15 °C and -20 °C a small kink is shown at approximately 75 % of the V_{BD}. It was investigated, whether it was correlated to fluctuations in temperature or relative humidity, but no indication for that could be found in the data. This kind of kink also appears in other measurements and is still under investigation.

6.7.4 Measurements on the Influence of Annealing on the Current Level of Irradiated Sensors

For the irradiated sensors of “Type 3.2“ four different IP-gaps were measured before and after annealing: 30 µm, 50 µm, 70 µm, and 95 µm.

As an example the IV-curves of 2×2 arrays W18-LG2x2-SE2-IP9-P1 are shown with

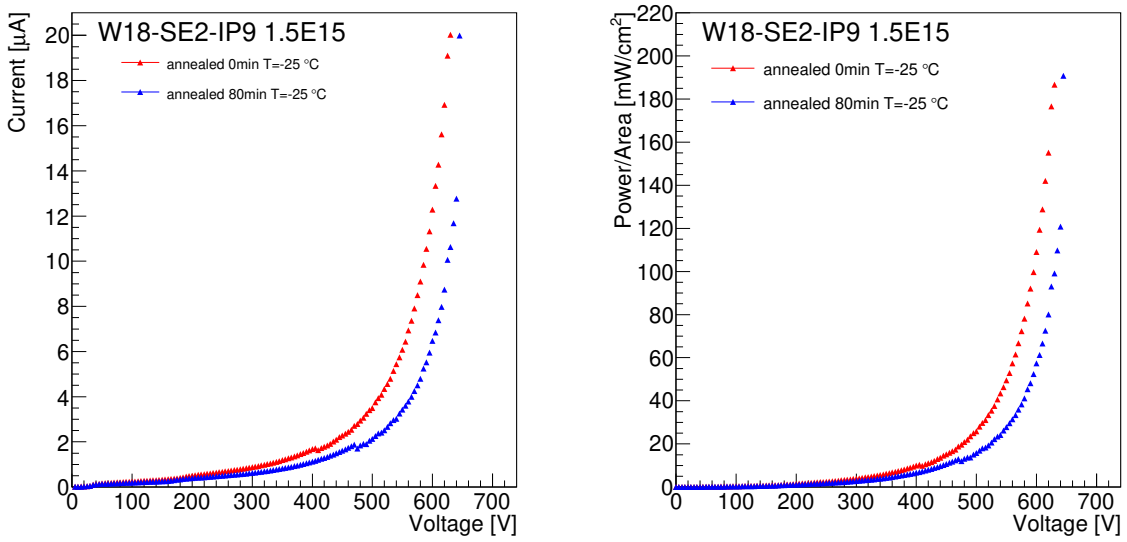

Figure 6.9: IV-curves of the 2×2 arrays W18-LG2x2-SE2-IP9-P1 measured at -25 °C before and after annealing. The current was measured for all four pads and the guard ring.

an irradiation fluence of $1.5 \cdot 10^{15}$ n_{eq}/cm^2 before and after annealing, shown in Figure 6.9. The measurements with the annealed sensors were performed after annealing for 80 min at 60 °C. 80 min simulate hundreds of years at -30 °C, and tens of days at room temperature. This roughly corresponds to one year of LHC operation with periods at room temperature during maintenance.

By annealing, as mentioned in Chapter 4.4, the leakage current decreases. This is reflected in the measurements in Figure 6.9. The current decreased at 80 % of the V_{BD} from 3.29 µA to 2.52 µA after annealing, while the V_{BD} was only slightly affected and shifted from 650 V to 645 V.

This satisfies the requirements set for the HGTD in terms of current per pad and bias voltage, listed in Table 5.1. Additionally, the power density (power/area) was derived. The IV-curve and the power dissipation for the sensor W18-LG2x2-SE2-IP9-P1 are shown in Figure 6.9. The power density increased with the bias voltage, but decreased from 24 mW/cm² to 16 mW/cm² after annealing at 80 % of the V_{BD}. The power dissipation could be minimised by operating the sensors at low temperatures and bias voltages.

The behaviour of the sensor W18-LG2x2-SE2-IP9-P1 is representative for the other sensors of the measured set of "Type 3.2". For the W14-LG2x2-SE5-IP3 sensor, shown in

Figure 6.10, the current level before and after annealing was already higher than for the other sensors at the same temperature. However, the current level decreased after annealing from 6 µA to 1.8 µA at 80 % of the V_{BD}. The correlated power dissipation is shown in Figure 6.11. The breakdown was also earlier than for the other sensors. The earlier breakdown and the higher current may be caused by a slightly lower radiation dose than the other sensors. Therefore a higher percentage of the gain layer is still intact. This hypothesis is further investigated in Chapter 7.

The W18-LG2x2-SE5-IP5 sensor, shown in Figure 6.10, had a lower current level at higher voltages than the other sensor, with 6 µA before and 3 µA after annealing at 80 % of the V_{BD}. The correlated power dissipation is shown in Figure 6.11. The V_{BD} was higher than for the other sensors, with 715 V after annealing. That could be explained with a higher radiation dose on the sensor than for the other sensors. Thereby the multiplication layer was affected more by the radiation, and a smaller gain factor amplified the leakage current. This is further investigated in Chapter 7.

The W18-LG2x2-SE5-IP7 sensor was only measured before annealing. During the annealing process, the wire-bonds connecting the sensor to the PCB were damaged, but with a replacement of the wire-bonds, the sensor would be fully functional again. The IV-curve and power dissipation before annealing showed the same behaviour as the example sensor, with the power dissipation shown in Figure 6.11. It also broke down at 600 V and had a current level of approximately 3 µA at 500 V.

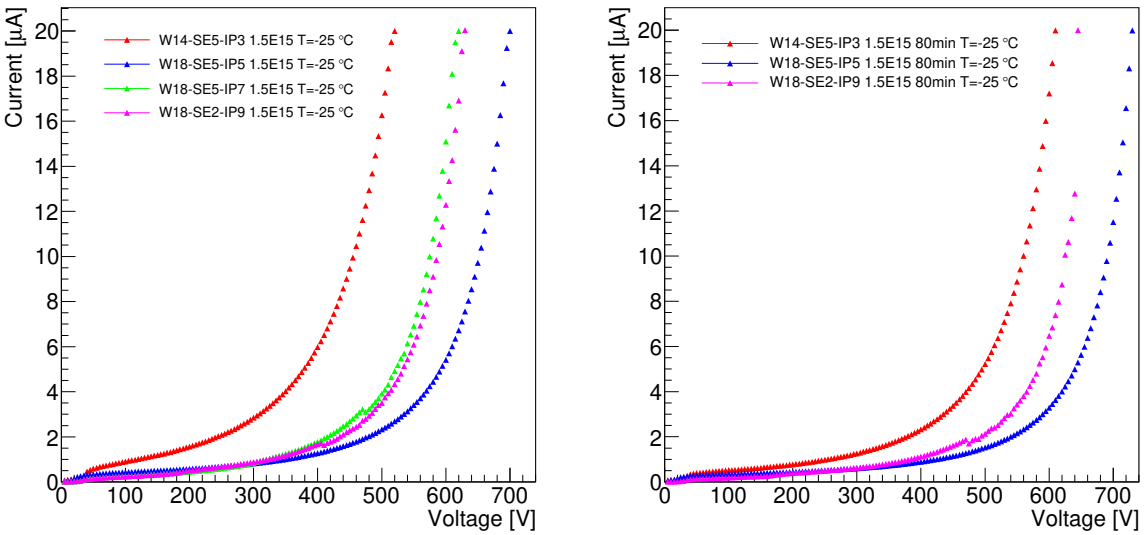

Figure 6.10: For all measured irradiated sensors the IV-curves before (left) and after annealing (right) for 80 min at 60 °C.

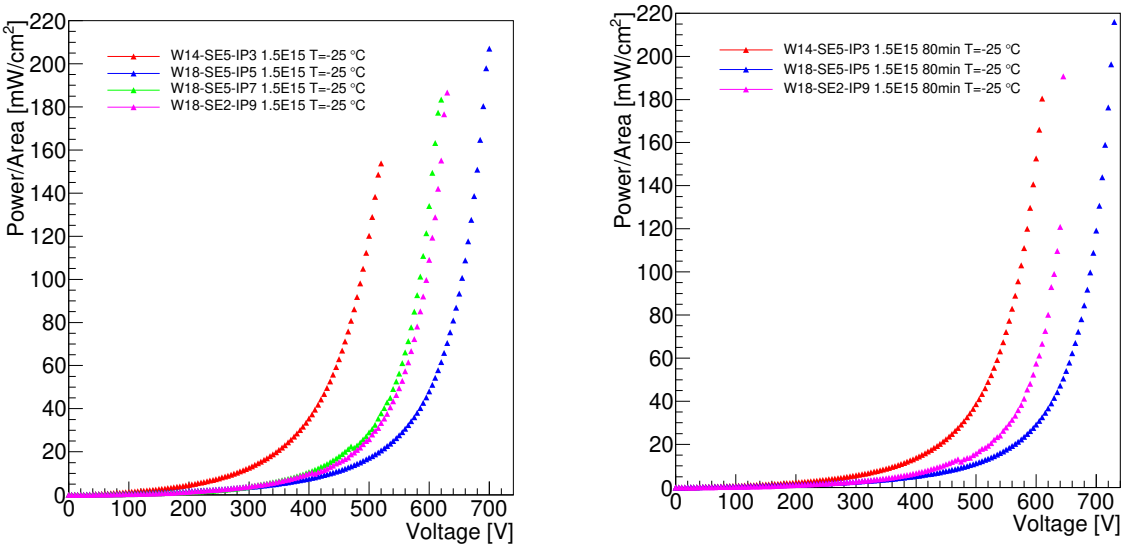

Figure 6.11: For all measured irradiated sensors the Power dissipation before (left) and after annealing (right) for 80 min at 60 °C.

7 Sensor Testing Methodology and Results: Transient Current Technique

A characterisation technique called Transient Current Technique (TCT) is wildly used to study the effects of signal formation and radiation damage in silicon. The main goals for the measurement with the TCT were the characterization of the no-gain gap between the pads of an LGAD array ($IP_{50\%}$) and thereby obtaining information on the fill-factor for the HGTD, since the nominal values quoted by the vendor does not reflect the electric field configuration of the sensors. For this reason, the values of the no-gain region between the pads were measured. It also allowed to gain information on the collected charge in the LGAD sensor and thereby obtained information about the gain factor caused by the multiplication layer. Both aspects were additionally tested under the aspect of irradiation and the caused radiation damage.

In the TCT set-up, a focused short-pulse laser was used to mimic the crossing of particles and thereby caused the injection of a localised cloud of electron-hole-pairs inside a detector. In the sensor, the charge drifted under the influence of an electric field to the electrodes. A transient current signal was generated, whose shape was related to the electric field profile, as explained in Chapter 4. By studying the induced current and charge, information about fill-factor and geometric aspects could be obtained. The fill-factor is the fraction of sensitive area of the detector. For the HGTD a fill-factor of 90% was intended [5], which would correspond to a $IP_{50\%}$ of around 70 µm for a pad size of 1.3 mm ×1.3 mm.

7.1 Experimental Set-up

The TCT set-up, shown in Figure 7.1, provided a light tight environment which prevented the influences of photo-current on the measurements by placing the measurement set-up inside a metal box with a removable lid.

Inside the box, the laser injection set-up was installed, with a laser-optic to focus the laser beam. It was fixed on top of a stage that moved along the z-axis, e.g. the longitudinal direction. x- and y-stages moved the sensor in front of the laser beam. The sensor was glued to a printed circuit board (PCB) via conductive double-sided tape. The single pads and the guard-ring were wire-bonded to connectors for signal extraction or ground lines. The PCB was placed in a holder, that was fixed onto a Peltier element for cooling. The Peltier element itself was cooled with a chiller. To power the sensor, a high voltage was provided by a Keithley 2410. The signal of two pads was passed to an oscilloscope of the type Tektronix DPO 4104 with 1 GHz, that was read out by a computer via USB, shown in Figure 7.1. No amplifier was used since the signal was high enough to be recorded by the oscilloscope.

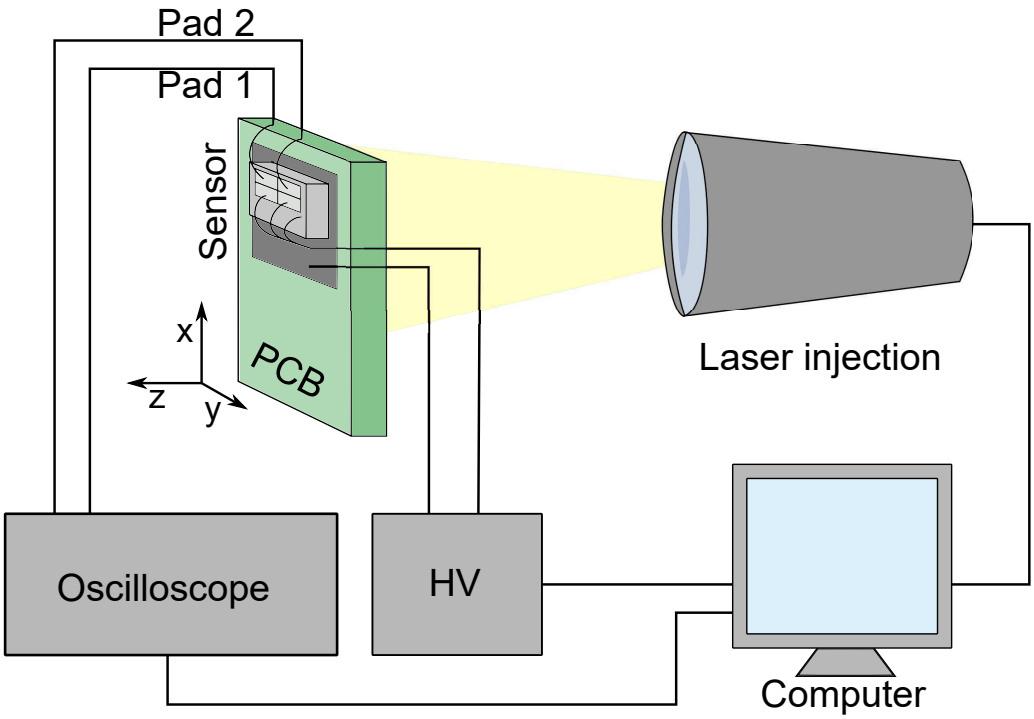

Figure 7.1: A schematic drawing of the TCT set-up, with respect to the wiring of the PCB.

The pulsed laser of 1060 nm wavelength was designed for use in Transient Current Technique (TCT) applications. Based on the absorption of light in silicon, the 1060 nm laser was selected, which has absorption depth of around 1 mm in silicon [49]. The laser deposits charges in the silicon like a passing MIP along its trajectory. The deposited charge depends on the penetration depth d. Here, 50 µm silicon were used. The deposited charge also depends on the laser settings. The laser combines a laser diode and a laser driver in a single unit, which enabled current pulses of around 300 ps to feed a fast laser diode. The laser had a symmetrical pulse without a low-intensity tail. The current passed to the diode was required to pass a certain threshold before it was fed to the laser diode. As the threshold increased, the width of the current above threshold narrowed. The threshold setting was realised with the DAC, controlled via USB. The maximum range of the DAC is at the voltage of 3.3 V, which corresponds in the default configuration of the software to 100% and means that the threshold is set as high as possible (3300 mV = 100%). For the measurements, the laser was set to a threshold of 1.435 V corresponding to 43.5 % and was operated at a frequency of 1 kHz. The deposited charge in a PIN-diode, which is a typical silicon sensor without a multiplication layer, was 5 fC. This could be translated to approximately 10 MIPs, passing through the sensor volume.

The laser injection into the sensor could be performed from the front opening in the Al or from the rear. The $IP_{50\%}$ measurements were performed from the rear opening, to examine the behaviour in the inter pad region. However, the space for the rear measurements was limited by the measurement set-up, because of the PCB on which the sensor was glued. The PCB provided a 2 mm diameter hole for the laser injection.

7.2 Testing Procedure

The oscilloscope measured the induced current as a voltage over the internal resistance R of 50 Ω. With the resistance:

$$I = \frac{U}{R} \tag{7.1}$$

An example signal for sensor W7-LG2x2-SE5-IP3-P2 is shown in Figure 7.2. The signal was ∼10 ns long and was only contained in the first peak, shown in Figure 7.2. After the signal oscillations occurred, which were caused by long wire bonds connecting the pad and the circuit board and thereby causing reflections due to impedance mismatch. To

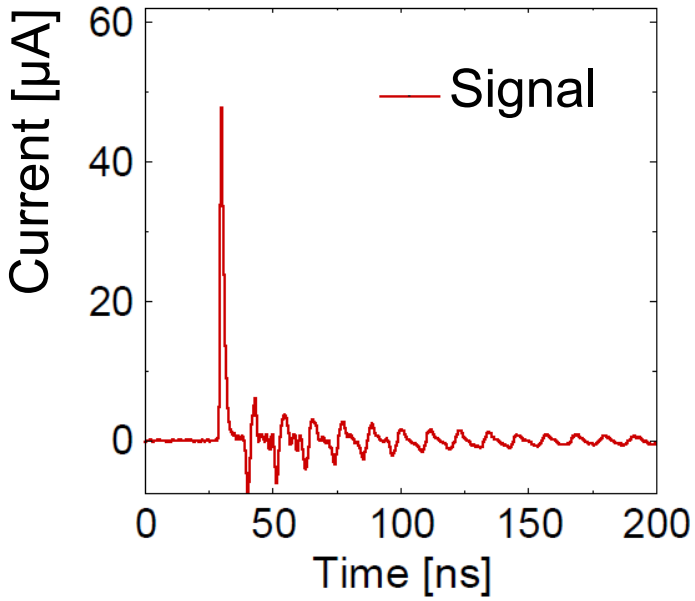

Figure 7.2: Example of a signal of sensor W7-LG2x2-SE5-IP3-P2, induced by a laser pulse, in µA.

receive the collected charge Q, the current was integrated over the time t:

$$\int_0^t I \mathrm{d}t' = Q \tag{7.2}$$

The signal was integrated over the first pulse, from 25 ns to 35 ns to obtain information about the LGAD signal, without the oscillations.

With the information about the collected charge obtained, measurements on the geometrical structure of the sensor were performed. Starting with scans over the x- and y-axis to determine the position of the sensor. In Figure 7.3 the xy-measurement of the not metallised strip on backside of a 2×2 sensor is shown. The scan over the position was first performed with a defocused laser, because the position for the focus scan had to be determined. Afterwards, the laser was focused, and the measurement was repeated.

A charge measurement determined the focus of the laser, by scanning over the junction of the opening on the backside and the backside metallisation. The measurement was fitted for every z-position with an error-function. The focus point is the z-position, at which the sigma of the function was the smallest, close to 7.3 µm. Then, a scan was performed over the no-gain gap between the pads. The measurement was performed over 400 µm in 5 µm steps along the x-axis for different voltages. The voltage level and steps were adjusted to

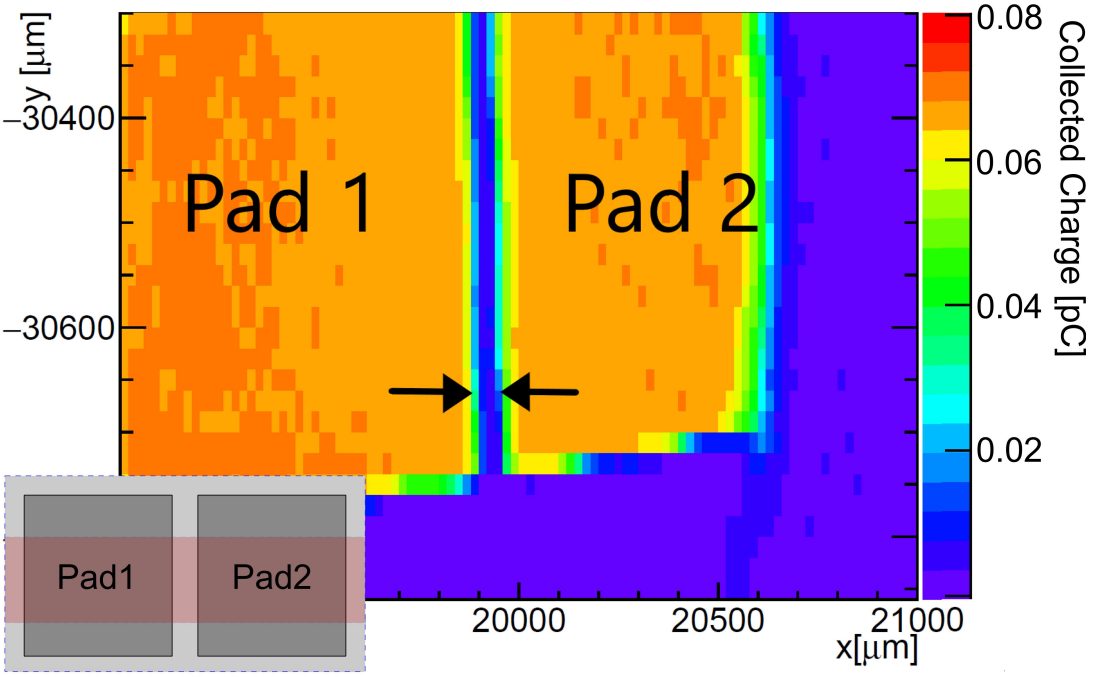

Figure 7.3: xy-scan over the no-gain gap between the pads region for the sensor W7-LG2x2-SE5-IP3-P2.

the measured sensor type. For each voltage step, the charge of the x-axis was projected in a 1D plot, as shown in Figure 7.4. The resulting curves for the two pads were then individually fitted with an error-function:

$$fit_1 = -h_1 \cdot \mathrm{erf}\left(\frac{x_1 - e_1}{\sigma_1}\right) \tag{7.3}$$

$$fit_2 = h_2 \cdot \mathrm{erf}\left(\frac{x_2 - e_2}{\sigma_2}\right), \tag{7.4}$$

with the error function erf, the fit parameter of the expected edge position e, the fit parameter of the Gaussian standard deviation σ and the fit parameter of the height h. After fitting the two pads, the effective no-gain gap between the pads was defined as the distance at the 50%-50% level of the two curves ($\mathrm{IP}_{50\%}$).

The fit shown in Figure 7.4 is not perfect. Towards the junction of the multiplication layer and the no-gain gap, an additional step is visible for both pads. This was caused by the signal generated in the no-gain gap, which was collected by the electrode. To include this effect, additional functions would have to be added for the fit. To avoid the effect of the no-gain gap, the curves were fitted just to around the 50%-point of the maximum. This affected the fitted value of the edge position by only 0.32 µm.

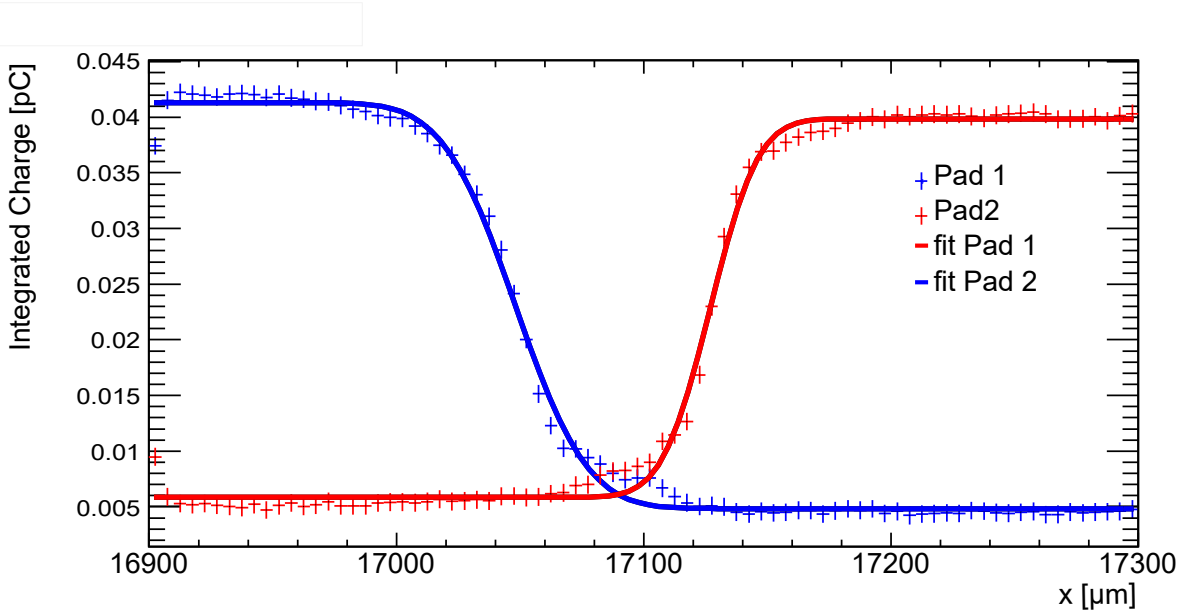

Figure 7.4: Projection of the charge for a voltage of 170 V over the no-gain gap of the sensor W7-LG2x2-SE5-IP3-P2.

7.3 Sensor Studies

For the measurements on the collected charge and the $IP_{50\%}$, several sensors were examined of "Type 3.1" and "Type 3.2". An overview of the sensors and measurements performed is given in Table 7.1.

7.3.1 Systematic Uncertainties

To determine the systematic error on the measurements, a reproducibility study was run. For this purpose, the sensor W7-LG2x2-SE5-IP3-P2 was measured ten times without interruption at the same voltage for the $IP_{50\%}$. The error was calculated for the charge measurements and the $IP_{50\%}$. Out of the ten measurements the standard deviation of the $IP_{50\%}$ was calculated to $\sigma_{IP_{50\%},\text{cont}} = 0.4$ µm and for the charge $\sigma_{Q,cont} = 0.9$ fC. This gives the systematic uncertainty for measurements during which the sample was not removed from the mount, such as the voltage dependency measurements for a sensor.

Another measurement series was run to determine the systematic error for the charge measurements and measurements on the $IP_{50\%}$ for different measurement runs. For this purpose, the same sensor as before, the W7-LG2x2-SE5-IP3-P2, was measured 5 times after taking the sensor out of the set-up and re-installing it. The standard deviation of

Sensor	Type	Irradiation [$n_{eq}cm^{-2}$]	Measurements
PIN		-	Voltage Dependency
W7-LG2x2-SE5-IP3-P2	3.1	-	Reproducibility Voltage Dependency
W7-LG2x2-SE5-IP5-P2	3.1	-	Voltage Dependency
W7-LG2x2-SE2-IP9-P2	3.1	-	Voltage Dependency
W18-LG2x2-SE5-IP3-P2	3.2	-	Temperature Relative Humidity Voltage Dependency
W18-LG2x2-SE5-IP5-P2	3.2	-	Voltage Dependency
W18-LG2x2-SE5-IP7-P2	3.2	-	Voltage Dependency
W18-LG2x2-SE2-IP9-P2	3.2	-	Voltage Dependency
W14-LG2x2-SE5-IP3-P1	3.2	$1.5 \cdot 10^{15}$	Voltage Dependency
W18-LG2x2-SE5-IP5-P1	3.2	$1.5 \cdot 10^{15}$	Voltage Dependency
W18-LG2x2-SE5-IP7-P1	3.2	$1.5 \cdot 10^{15}$	Voltage Dependency
W18-LG2x2-SE2-IP9-P1	3.2	$1.5 \cdot 10^{15}$	Voltage Dependency

Table 7.1: Overview over the sensors and the performed measurements.

the $IP_{50\%}$ is $\sigma_{IP_{50\%},\text{run}} = 5$ µm and for the charge $\sigma_{Q,run} = 4$ fC. This error was added for measurements comparing different sensor measurement runs to each other.

The systematic uncertainties for the comparison of runs are about an order of magnitude larger than the systematic uncertainties for one run. A possible reason may lie in the geometrical aspects of the sensor. Since the sensor was removed and re-installed in the set-up, it could have been installed with a slight inclination, which would affect the $IP_{50\%}$ measurement. Also, the laser was turned off for the duration of the re-instalment, which may caused fluctuation in the laser performance. Additionally, by opening the TCT-box for the re-instalment of the sensor, the relative humidity and the temperature were changed. To determine the influence of the environmental conditions, further measurements were performed.

7.3.2 Temperature and Relative Humidity

Measurements were performed to determine whether the temperature or the relative humidity in the TCT set-up had an influence on the measured $IP_{50\%}$ or the collected charge.

The influence of the temperature on the $IP_{50\%}$ was tested. For this purpose, the W18-LG2x2-SE5-IP3-P2 sensor was used. The sensor was placed in the TCT set-up and not touched throughout the temperature testing, therefore as a systematic uncertainty

$\sigma_{\mathrm{IP}_{50\%},\mathrm{cont}} = 0.39$ µm was applied. During the whole testing procedure, a constant relative humidity of 3.7% was measured. The measurements were performed first without cooling, at 24.9 °C. Followed by several measurements with different cooling settings at 5 °C, -5 °C, and -20 °C. The temperatures were measured via a temperature sensor on the backside of the mount and by comparing the leakage current to previously measured IV-curves of the sensors. Afterwards, the sensor was heated up and measured again at room temperature at 24 °C. The measured, collected charge and the $\mathrm{IP}_{50\%}$ values are shown in Figure 7.5, in dependence on the applied bias voltages and temperature.

For the charge measurement as well as for the $\mathrm{IP}_{50\%}$, the measurements at room temperature, before and after cooling, show a reasonable agreement with a similar charge collected and $\mathrm{IP}_{50\%}$ values. The charge measurement showed an increase in gain and therefore charge with increased applied voltage. At the same time, the $\mathrm{IP}_{50\%}$ decreased. For lower temperatures, the charge and gain were higher, compared to the measurements at the same voltage at a higher temperature. For the measurement at -20 °C compared to the one at 24 °C, the charge nearly doubles at every voltage step. Meanwhile, the $\mathrm{IP}_{50\%}$ increased with the decrease in the temperature. This is the most visible at 75 V, where the measurement at -13.5 °C had an $\mathrm{IP}_{50\%}$ of (100.8 ± 0.8) µm and the measurements at 24.9 °C had an $\mathrm{IP}_{50\%}$ of (93.8 ± 0.9) µm. Here the error gives the combined error of systematic and statistical error. Another effect, noticeable for the measurements was that the cooled sensors broke down at a lower voltage and therefore were not measured up to the same voltage as the warm sensors, which is also described in Chapter 6.

Another environmental parameter, whose influence on the charge and the $\mathrm{IP}_{50\%}$ values was studied, was the relative humidity in the box of the TCT set-up. The W18-LG2x2-SE5-IP3 was measured at 100 V at a temperature of 24.9 °C, which was monitored during the measurement. For the measurement, the sensor was not touched during the whole process, therefore the systematic error of $\sigma_{Q,cont} = 0.9$ fC for the charge and $\sigma_{\mathrm{IP}_{50\%},\mathrm{cont}} = 0.39$ µm for the $\mathrm{IP}_{50\%}$ was applied. For the measurement, the box was flushed with dry air to the minimal relative humidity. Afterwards, the lid was lifted for 20 seconds, secured back on and afterwards waited for 5 minutes to ensure a homogeneous distribution of the humidity in the box. Then the measurement was performed. The resulting measurements are shown in Figure 7.6. The measured charge and $\mathrm{IP}_{50\%}$ were not significantly influenced by relative humidity.

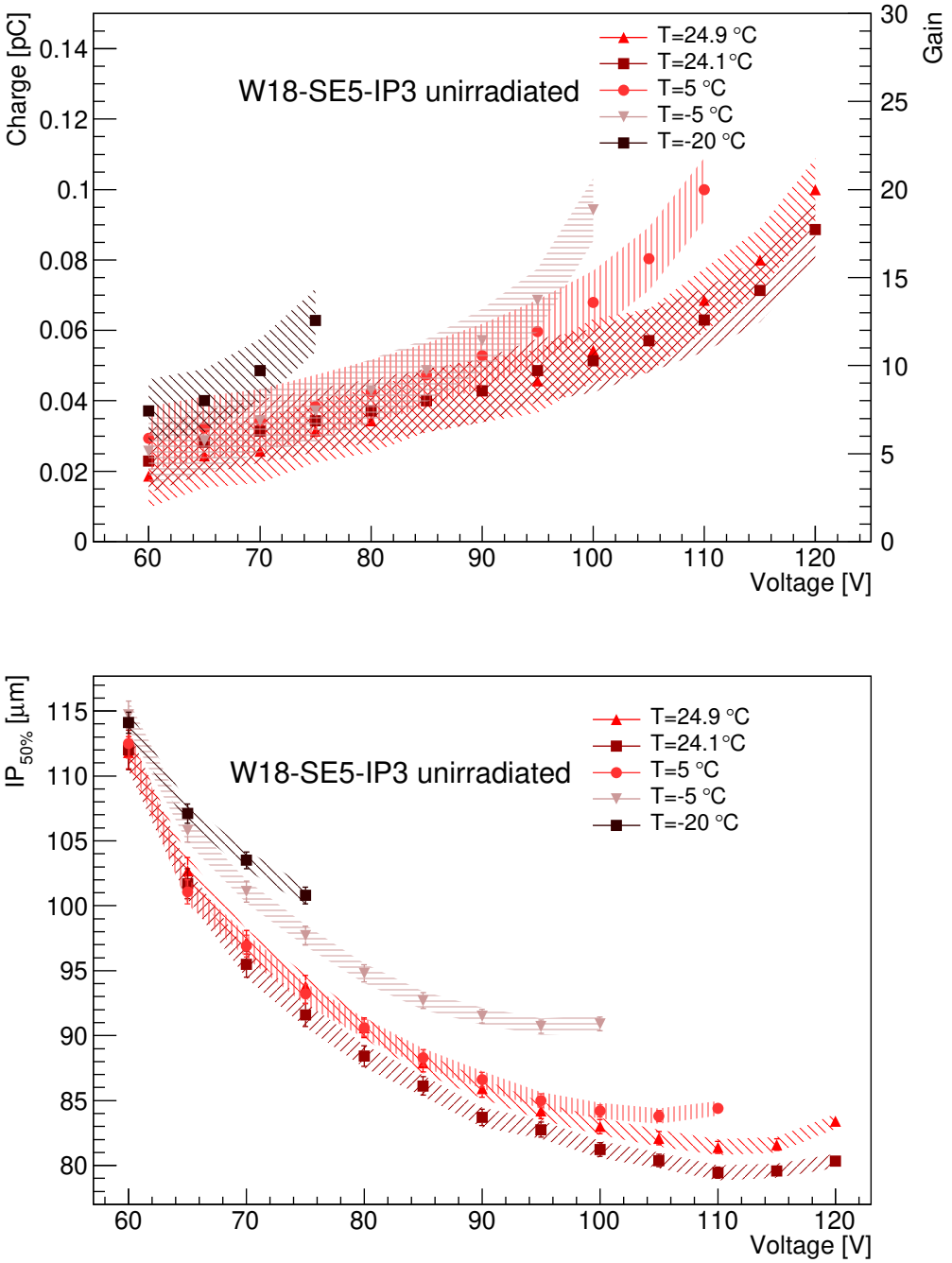

Figure 7.5: Measurements of the collected charge (top) and the $IP_{50\%}$ (bottom) of the sensor W8-LG2x2-SE5-IP3-P2 in dependence of temperature and voltage. The error bar gives the statistical error and the colour band give the square root of the quadratic sum of the systematic and the statistical error. For the systematic error $\sigma_{IP_{50\%},cont} = 0.39$ µm was taken, since the sensor was measured without interruption in the set-up. For visibility, the $\sigma_{IP_{50\%},run}$ are not shown here.

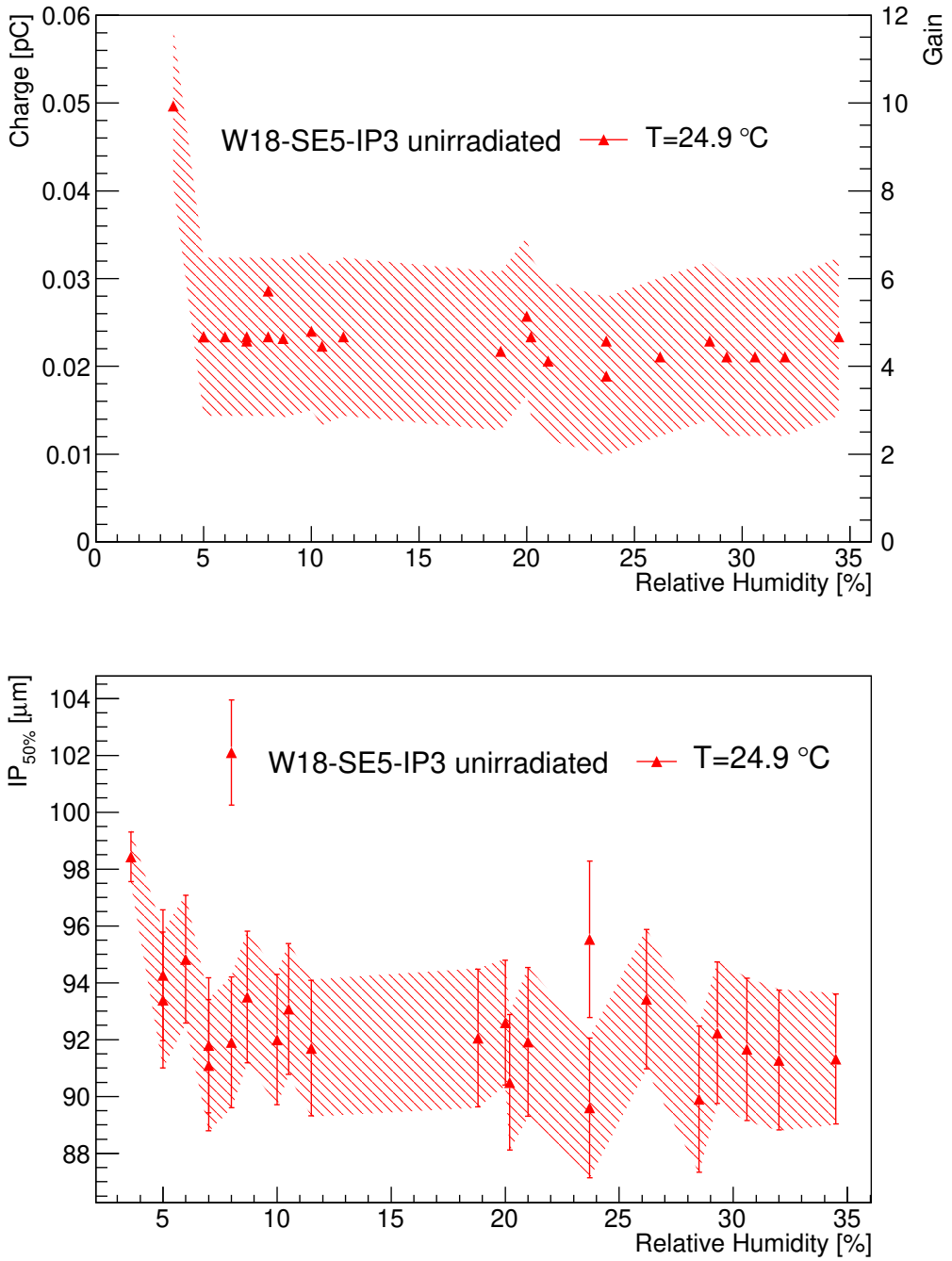

Figure 7.6: Measurements of the collected charge (top) and the $IP_{50\%}$ (bottom) of the sensor W8-LG2x2-SE5-IP3-P2 in dependence of the relative humidity at 170 V. The error bar gives the statistical error and the colour band give the square root of the quadratic sum of the systematic and the statistical error. For the systematic error $\sigma_{IP_{50\%},cont} = 0.39$ µm was taken, since the sensor was measured without interruption in the set-up. For visibility, the $\sigma_{IP_{50\%},run}$ are not shown here.

7.3.3 Voltage Dependence and different IP Parameters for $IP_{50\%}$ and Collected Charge Q

For the measurements on the charge and the $IP_{50\%}$, a voltage dependence was expected, since they depend on the shape of and strength of the electrical field lines in the sensor volume, which respectively depend on the applied voltage. Additionally, the influence of irradiation for sensors of "Type 3.2" with a fluence of 1.5×10^{15} $n_{eq}cm^{-2}$ on the charge and the $IP_{50\%}$ was examined. The fluence corresponds to the radiation level which is expected close to the end of the lifetime of the sensors and it was studied whether the fill-factor was affected by the irradiation.

The measurements on the collected charge and the $IP_{50\%}$ measurements were performed at room temperature for the unirradiated sensors. The sensors of "Type 3.2" were measured from 60 V to 120 V and the sensors of "Type 3.1" were measured at from 100 V to 240 V which was determined by the previous IV-measurements as a safe voltage range for the sensor.

To obtain the gain, the initial induced charge by the laser had to be determined with a PIN-diode, which is plotted in Figure 7.7. The charge measured was 5 fC and not significantly influenced by the voltage as expected, since no multiplication layer is present. The voltage level has to be high enough to deplete the sensor volume. With this, the equivalent number of MIPs passing could be determined. The induced single for a passing MIP corresponded to about 0.5 fC [50]. Therefore the induced signal in a PIN diode without multiplication layer corresponded to 10 MIPS passing.

With the initial induced charges known, the gain G of the LGAD sensors could be calculated with

$$\frac{Q_{\mathrm{LGAD}}}{Q_{\mathrm{PIN}}} = G. \tag{7.5}$$

Here Q_{LGAD} is the charge of the measured LGAD sensor and Q_{PIN} is the charge of the PIN-diode.

The collected charge, as well as the correlated gain, are shown in Figure 7.7. The error for the measured charge was determined by determining the RMS of the charge over an area with no sensitive area present, which resulted in an error of 0.4 fC. The error is so small that it is not visible in the shown Figure 7.7. For all unirradiated sensors

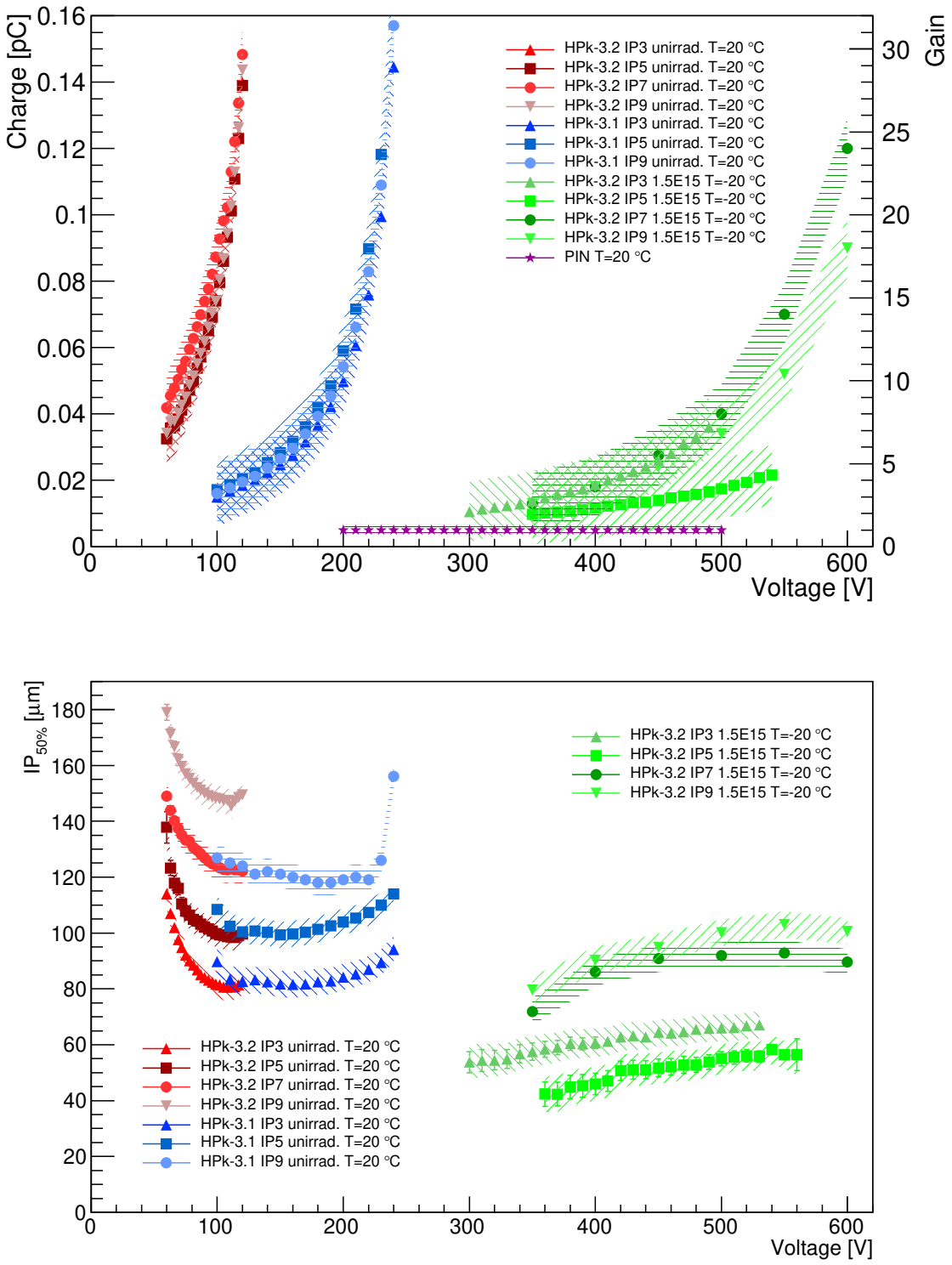

Figure 7.7: Summarised results of the measurements of the collected charge (top) and the $IP_{50\%}$ (bottom) of the sensors of "Type 3.1" and "Type 3.2" in dependence on the voltage. The error bar gives the statistical error and the colour band gives the combined statistical and systematic error $\sigma_{IP_{50\%},run}$.

of “Type 3.2“ the charge and gain are similar with a collected charge of around 0.04 pC at 100 V and a substantial increase with voltage to about 0.16 pC to 110 V, which was expected since the multiplication layer configuration is the same. The same behaviour is visible for the sensors of “Type 3.1“. They start with a collected charge of about 0.02 pC at 100 V, which is only half the charge collected by the “Type 3.2“ sensors. This is expected since the multiplication layer is less strongly doped in the “Type 3.1“ than in the “Type 3.2“. The charge then sharply increases with increased voltage up to 0.16 pC at 240 V, which translates into a gain of 32.

The same measurements were performed for irradiated sensors of “Type 3.2“. They were irradiated with a fluence of 1.5×10^{15} $n_{eq}cm^{-2}$. The irradiated sensors were cooled during the measurement to -20 °C. The on-sensor temperature was extracted by the leakage current to the measured IV-curves at different temperatures in Chapter 6. As explained in Chapter 6, the breakdown voltage for irradiated sensors increases because the gain decreases and thereby also the collected charge measured decreases. Therefore, the sensors were measured at higher voltages to obtain a signal that can be distinguished from the background. For the irradiated sensors of “Type 3.2“, the sensors with an IP3, IP7 and IP9 show a similar behaviour in their collected charge with about 0.01 pC at 350 V and again a strong increase in the collected charge to about 0.04 pC at 500 V. The sensor with the IP5 shows a weak increase in the collected charge from 0.01 pC at 350 V to 0.02 pC at 550 V. A higher radiation fluence could explain such a significantly different behaviour. This could also explain the much lower measured $IP_{50\%}$ for the sensor shown previously.

For the $IP_{50\%}$, all sensors for “Type 3.2“ showed a larger $IP_{50\%}$ at 60 V, which decreases strongly with increased voltage, up to 100 V. For further increased voltages, a slight increase in the $IP_{50\%}$ is visible. The sensors for “Type 3.1“ show a less strong decrease of the $IP_{50\%}$ from 100 V with increasing voltage, but a much stronger increase towards the end of the voltage interval.

The decrease in the $IP_{50\%}$ was most probable caused by the change of the electric field lines in the sensor volume through the applied bias voltage. For LGAD sensors, especially the JTE is affected, as explained in Chapter 5. Higher bias voltages cause the field lines to approach a more ideal configuration, which explains the decrease in the $IP_{50\%}$ for higher voltages. The slight increase towards higher bias voltages is still under investigation. A possible reason, especially with respect to the measurements of “Type 3.1“ is the proximity of the applied voltage to the V_{BD}.

The $IP_{50\%}$ measurements of the unirradiated sensors of "Type 3.1" matched quite well with the ones of "Type 3.1". It is worth mentioning, that the "Type 3.1" sensor with an IP9 showed $IP_{50\%}$ values, which matched with the $IP_{50\%}$ values for the "Type 3.2" with an IP7. The behaviour was reproducible on repeated measurements. No "Type 3.1" IP7 sensor was available for comparative measurements. Further measurements with different IP7 and IP9 sensors should be performed to understand this behaviour.

Compared to the unirradiated sensors, the irradiated $IP_{50\%}$ of "Type 3.2" decreased significantly, down to 45 µm. This was most probable caused by the reduction of the acceptor density in the multiplication layer, therefore a reduced influence on the field lines by the JTE. However, in contrast to the unirradiated sensors, the irradiated sensors showed an increase in the $IP_{50\%}$ with increasing voltage. This behaviour needs further studies and detailed simulation of the field in irradiated sensors.

The lowest measured $IP_{50\%}$ for all unirradiated sensors is about 80 µm, which corresponds to a fill-factor of 88.5 %.

Both unirradiated and irradiated sensors showed a much larger $IP_{50\%}$ than the nominal IP given by the supplier, visualised in Figure 7.8. The $IP_{50\%}$p is plotted against the nominal IP gap for the unirradiated sensors of "Type 3.2" at 100 V and sensors of "Type 3.1" at 200 V and of the irradiated sensors of "Type 3.2" at 550 V. As discussed above, the difference was most likely caused by the JTE and its influence on the shape of the electric field lines in the sensor volume. Additionally, the decrease of the $IP_{50\%}$ from unirradiated to irradiated sensor for "Type 3.2" is visible. A decree of 15 µm to 45 µm is shown.

Another aspect was the influence of annealing on the charge collection and the $IP_{50\%}$ in the irradiated sensors. The annealing was studied because it affected the radiation damage, which was especially crucial for the multiplication layer since already small changes would change the gain. The charge of the two measured annealed sensors, before and after annealing, are shown. In Figure 7.9, the measurements for the sensor W14-LG2x2-SE5-IP3-P1 are shown and in Figure 7.10 the measurements for the sensor W18-LG2x2-SE5-IP5-P1. Annealing was performed for 80 min at 60 °C.

The sensors W14-LG2x2-SE5-IP3-P1 7.9 and W18-LG2x2-SE5-IP5-P1 7.10 were measured. For the sensor W14-LG2x2-SE5-IP3-P1 a slight decreased in the collected charge

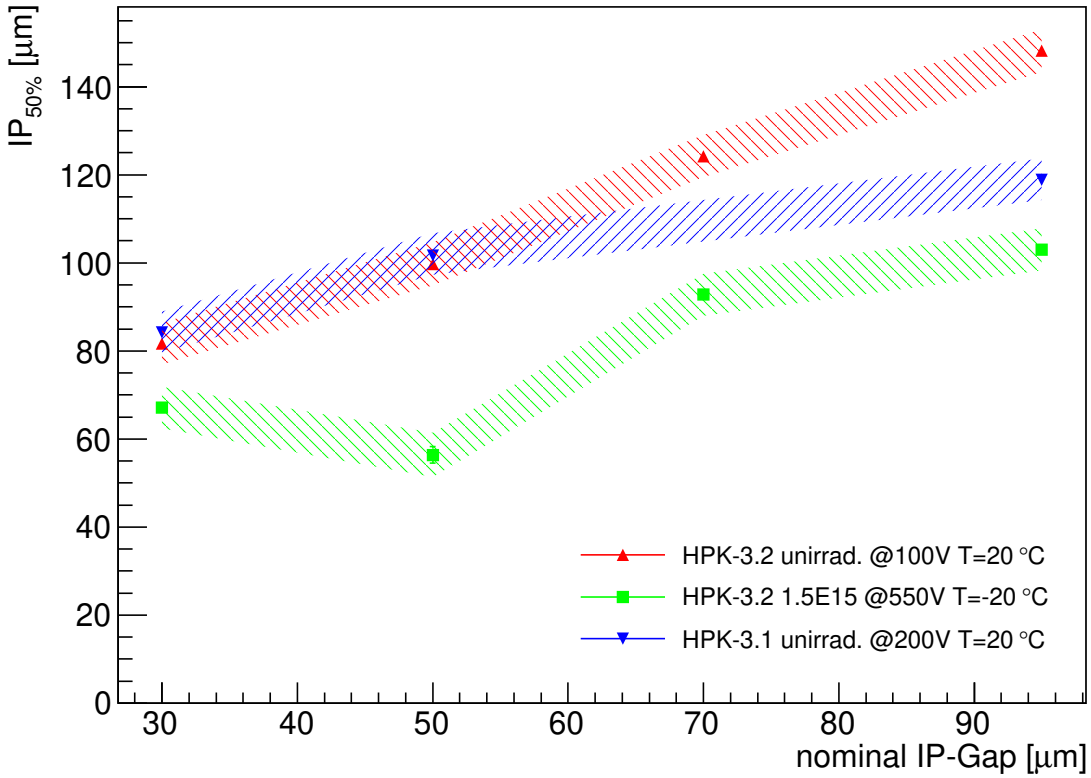

Figure 7.8: Measurements on the $IP_{50\%}$ compared to the nominal IP-gap for a set of unirradiated sensors of "Type 3.1" and "Type 3.2" and a set of sensors of "Type 3.2" irradiated with a fluence of $1.5 \cdot 10^{15}$ $n_{eq}cm^{-2}$. The unirradiated sensors are shown at 100 V for "Type 3.2" , 200 V for "Type 3.1" and the irradiated sensors of "Type 3.2" at 550 V. The error bar gives the statistical error and the colour band gives the combined statistical and systematic error $\sigma_{IP_{50\%},run}$.

was observed from 0.035 pC before annealing to 0.025 pC after annealing, at 480 V. However, the breakdown voltage was increased significantly, wherefore the sensor could be measured to up to 690 V after annealing. Also, after annealing, the $IP_{50\%}$ decreased by about 5 µm, but the statistical error for the fit increases because of the smaller collected charges. The same behaviour was observed for the sensor W18-LG2x2-SE5-IP5-P1, with a decrease in the collected charge from 0.0213 pC to 0.008 pC at 540 V, which translates to a gain of 1.6. This confirms the assumption of a higher radiation dose on the sensor because the damage was influenced by annealing and the gain was nearly completely lost. The $IP_{50\%}$ measurements showed an unstable behaviour after annealing. A decrease in the $IP_{50\%}$ was observed, but not significant, since for this sensor also the statistical error for the fit increases because of the smaller collected charges.

In conclusion, the annealing did not influence the collected charge strongly, but the performance is slightly better before annealing in terms of smaller required voltage for a given gain. There was an indication that annealing increases the operation point to higher voltages at a given gain. Further studies, for different annealing times, are required to see a more detailed impact of annealing.

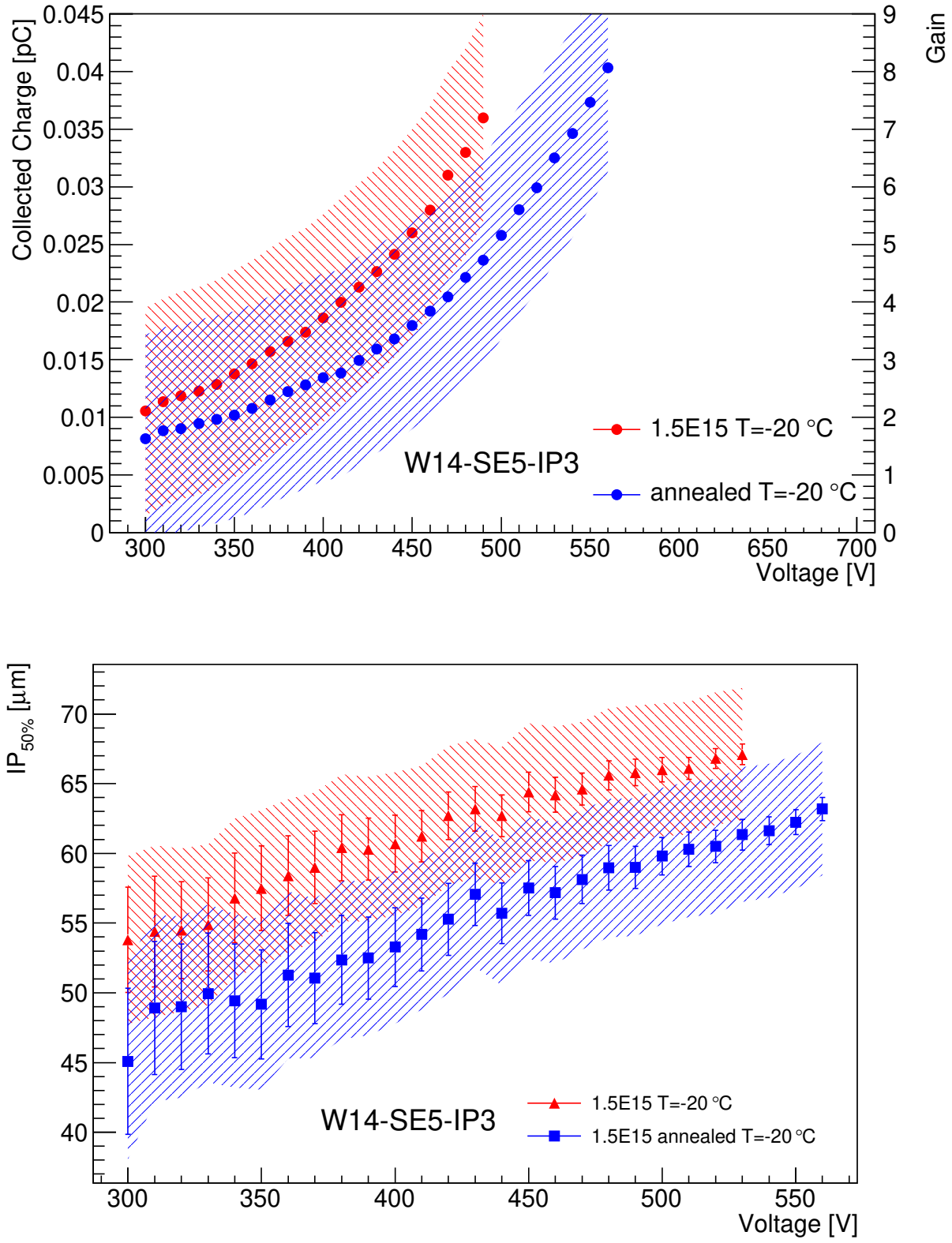

Figure 7.9: Comparison between the measurements on the 2×2 array W14-LG2x2-SE5-IP3-P1, irradiated with a fluence of $1.5 \cdot 10^{15}$ $n_{eq}cm^{-2}$, before and after annealing. Annealing was performed for 80 minutes at 60 °C. The error bar gives the statistical error and the colour band gives the combined statistical and systematic error $\sigma_{IP_{50\%},run}$.

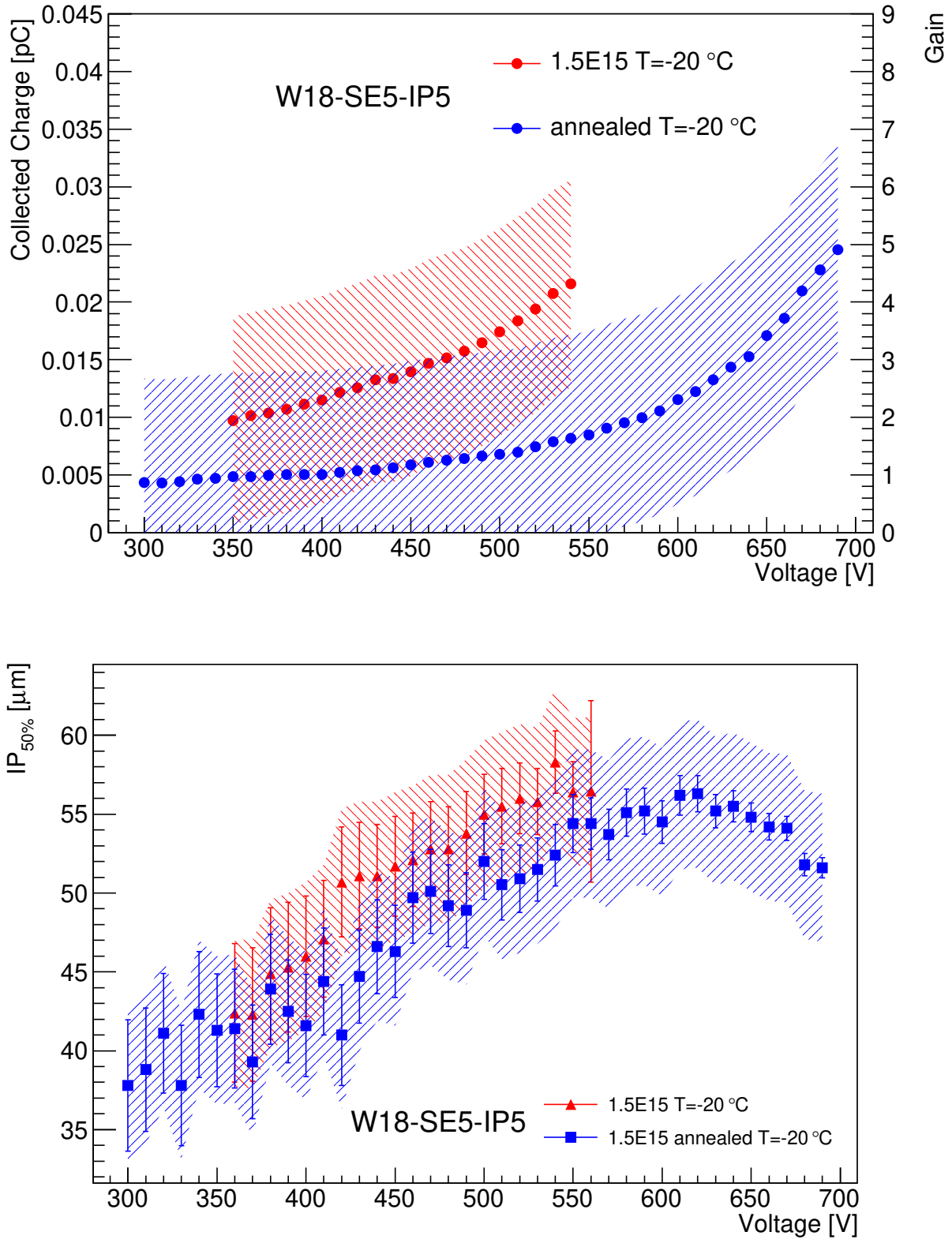

Figure 7.10: Comparison between the measurements on the 2×2 array W18-LG2x2-SE5-IP5-P1, irradiated with a fluence of $1.5 \cdot 10^{15}$ $n_{eq}cm^{-2}$, before and after annealing. Annealing was performed for 80 minutes at 60 °C. The error bar gives the statistical error and the colour band gives the combined statistical and systematic error $\sigma_{IP_{50\%},run}$.

8 Conclusion and Outlook

For the characterisation of Low Gain Avalanche Detectors for the High Granularity Timing Detector two different types of sensors from Hamamatsu Photonics were studies: The sensors of "Type 3.1" with a lower doping concentration and shallower multiplication layer and the sensors of "Type 3.2" with a higher doping concentration and deeper multiplication layer. The sensors were characterised with two measurement techniques, which were IV characterisations and the Transient Current Technique. In this thesis the measurements were performed to characterise five aspects of the sensors: Homogeneity, yield, demonstration of large sensors, fill-factor, and radiation hardness.

8.1 Current-Voltage Curves

For the sensors of "Type 3.2" before irradiation, the 15×15 array measurements showed an overall good quality with roughly (91.30 ± 6.27) % of good sensors, excluding the P1 sets, which were believed to have one systematic bad performing pad due to a masking issue in the production. The average breakdown voltage was at 128 V with a standard deviation of 5 V and the average current at 80 % of the breakdown voltage was 3.85 nA with a standard deviation of 1.22 nA. For sensors of "Type 3.1" before irradiation, the fraction of good sensors is (84.62 ± 7.11) % with an average breakdown voltage of 200.33 V and a standard deviation of 8.29 V. The current level measured at 80% of the breakdown voltage was 3.85 nA with a standard deviation of 1.6 nA. All tested arrays show increased currents towards the edge due to floating guard rings. Apart from this, the arrays show a good homogeneity over the sensor and the feasibility of the production of large sensors could be demonstrated by the good fraction of sensors.

To determine effects of radiation damage, measurements on 2×2 arrays of "Type 3.2", irradiated with a fluence of $1.5 \cdot 10^{15}$ $n_{eq}cm^{-2}$, were performed. The leakage currents increased strongly for the irradiated sensors to the order of few µA. However, the sensors of "Type 3.2" satisfy the requirement of the ALTIROC, which can handle a maximal current of 5 µA per pad, up to the highest voltage measured ($\approx 600\ V$). From this the power

density was derived. The power could be minimised by operating the sensors at an as low as possible temperature and bias voltage. A large beneficial effect of annealing could be observed on the leakage current.

Additionally, measurements on the V_{BD} dependency on the IP and SE parameters were performed. For the SE no significant influence on the V_{BD} could be determined, but for decreasing IP a slight decrease in the V_{BD} was observed.

8.2 Transient Current Technique

In the laboratory the sensors were tested with an infrared laser of 1060 nm wavelength. The laser was configured to an intensity that induces a signal of 0.5 fC in a 50 µm PIN-diode. The light was injected through the sensor's rear opening of the metallisation and scanned from one pad to the other. The two profiles of the pulse maximum were fitted with an error function and the distance between the pads is evaluated and the charge plateau is determined. The measured effective distance between the neighbouring pads can be estimated as the distance where charge collection efficiency drops to 50% on first pad and rises to 50% on the neighbour (50%-50% point), which is labelled as the $\mathrm{IP}_{50\%}$.

The collected charge, which strongly depends on the laser configuration, and gain were determined for unirradiated sensors of "Type 3.1", "Type 3.2" and irradiated sensors of "Type 3.2". For all sensors the collected charge depends on the doping concentration of the sensor, the voltage and the irradiation fluence. The collected charge for sensors of "Type 3.2" is 0.1 pC at 100 V which corresponds to a gain of 20. For sensors of "Type 3.1" the same charge and gain is reached at 210 V. After irradiation with a fluence of $1.5 \cdot 10^{15}$ $\mathrm{n_{eq}cm^{-2}}$ the gain of the sensors of "Type 3.2" showed the expected decrease due to lower acceptor concentrations in the multiplication layer, with about 0.02 pC at 450 V. The collected charge for irradiated sensors can be increased to 0.1 pC at around 560 V, given the breakdown does not occur before the voltage is reached. For the IP5 sensor of "Type 3.2", the collected charge just reaches 0.02 pC at maximum operation voltage, which also indicates a higher radiation fluence. After annealing, there seems to be a decrease of acceptors in the gain layer, which causes a reduced collected charge.

The $\mathrm{IP}_{50\%}$ scans for all sensors showed a strong dependency on the applied voltage. The lowest measured value per type (roughly 80 µm for "Type 3.1" at 170 V and "Type 3.2" at 100 V) are about 50 µm higher than the nominal IP value quoted by the vendor and cor-

respond to a fill-factor of 88.5%. "Type 3.2" shows a decrease in $IP_{50\%}$ of about 10 µm on average after irradiation with a fluence of $1.5 \cdot 10^{15}$ $n_{eq}cm^{-2}$. For the sensor with an IP5, the $IP_{50\%}$ shows a decreases of 45 µm, which is believed to be caused by a higher radiation dose than the other sensors. After annealing for 80 min at 60 °C, there seems to be a decrease of initial acceptors in the gain layer with annealing, which causes a decrease in the $IP_{50\%}$. However, the decrease in the $IP_{50\%}$ is not significant.

This shows that given a good voltage stability a certain gain can be reached, also after irradiation. Further investigations on the voltage stability and dependence of the gain at more fluence steps are planned.

8.3 Outlook

The presented LGAD sensors are prototypes and newer designs address the problems in the multiplication layer concentration and radiation hardness.

The doping concentration of the multiplication layer is planned to be tuned further in the future by a few %, compared to the "Type 3.2" sensors, to reach higher breakdown voltages and thereby establish the drift field. Additionally, for future testing 15×15 arrays with different IP and SE are planned to be produced as well as sensors of the full size of 30×15. Additionally, further studies for different irradiation fluences are planned in the near future, as well as $IP_{50\%}$ measurements on irradiated sensors of "Type 3.1".

Extensive irradiation campaigns are performed to demonstrate the radiation hardness of the sensor. Furthermore, the transient current technique is used to investigate the development of the depletion zone in more detail. Also, the time resolution is studied in measurements with β-sources and at test beam campaigns. Future efforts include more detailed simulations of the electrical field of the sensor to gain further insight into the no-gain region and the effects of the JTE and test beam measurements of the IP region to complement of the laboratory measurements with studies using MIPs.

The planned time line of the HGTD is that in 2020 the final prototypes will be produced and tested. A market survey will be conducted in 2020, based on the understanding of the design issues solved in 2019. Then a pre-production run will follow in 2021. The installation in ATLAS is planned for long shut down 3 in 2024-2026.

Bibliography

[1] F. Englert, R. Brout, *Broken Symmetry and the Mass of Gauge Vector Mesons*, Phys. Rev. Lett. **13**, 321 (1964)

[2] P. W. Higgs, *Broken Symmetries and the Masses of Gauge Bosons*, Phys. Rev. Lett. **13**, 508 (1964)

[3] G. S. Guralnik, C. R. Hagen, T. W. B. Kibble, *Global Conservation Laws and Massless Particles*, Phys. Rev. Lett. **13**, 585 (1964)

[4] L. R. Evans, *The Large Hadron Collider (LHC)*, Eur. Phys. J. C **34**, S11 (2004)

[5] ATLAS Collaboration, *Technical Proposal: A High-Granularity Timing Detector for the ATLAS Phase-II Upgrade*, Technical Report CERN-LHCC-2018-023. LHCC-P-012, CERN, Geneva (2018)

[6] S. L. Glashow, *Partial-symmetries of weak interactions*, Nucl. Phys. **22**, 579 (1961)

[7] S. Weinberg, *A Model of Leptons*, Phys. Rev. Lett. **19**, 1264 (1967)

[8] A. Salam, *Elementary Particle Physics: Relativistic Groups and Analyticity*, in *8-th Nobel Symposium*, page 367, Almquvist and Wiksell, Stockholm (1968)

[9] G. 't Hooft, *Renormalizable Lagrangians For Massive Yang-Mills Fields*, Nucl. Phys. B **35**, 167 (1971)

[10] G. 't Hooft, M. Veltmann, *Regularization And Renormalization Of Gauge Fields*, Nucl. Phys. B **44**, 189 (1972)

[11] M. Tanabashi, et al. (Particle Data Group), *Review of Particle Physics*, Phys. Rev. D **98**, 030001 (2018)

[12] O. Brüning et al., *LHC Design Report*, CERN Yellow Reports: Monographs, CERN, Geneva (2004)

[13] L. Evans, P. Bryant, *LHC Machine*, JINST **3**, S08001 (2008)

[14] O. Brüning, et al., *Large Hadron Collider Design Report*, CERN (Series), European Organization for Nuclear Research (2004)

[15] ATLAS Collaboration, *The ATLAS Experiment at the CERN Large Hadron Collider*, JINST **3**, S08003 (2008)

[16] ATLAS Collaboration, *ATLAS Technical Proposal for a General-Purpose pp Experiment at the Large Hadron Collider at CERN*, CERN/LHCC/94-43, LHCC/P2, (unpublished) (1994)

[17] ATLAS Collaboration, *ATLAS inner detector: Technical design report. Vol. 1*, Tech .Rep., CERN, Geneva (1997)

[18] ATLAS Collaboration, *ATLAS inner detector: Technical design report. Vol. 2* (1997)

[19] M. Lehmacher, *b-Tagging Algorithms and their Performance at ATLAS* **(ATL-PHYS-PROC-2008-052. ATL-COM-PHYS-2008-152)** (2008)

[20] ATLAS Collaboration, *Performance of b-jet identification in the ATLAS experiment*, JINST **11**, P04008 (2016)

[21] A. L. Rosa, *The ATLAS Insertable B-Layer: from construction to operation*, JINST **11(12)**, C12036 (2016)

[22] ATLAS Collaboration, *ATLAS Insertable B-Layer Technical Design Report*, Technical Report CERN-LHCC-2010-013. ATLAS-TDR-19 (2010)

[23] ATLAS Collaboration, *Operation and performance of the ATLAS semiconductor tracker*, JINST **9(08)**, P08009 (2014)

[24] ATLAS Collaboration, *ATLAS liquid-argon calorimeter: Technical Design Report*, Tech .Rep., CERN, Geneva (1996)

[25] S. Berglund, et al., *The ATLAS Tile Calorimeter digitizer*, JINST **3(01)**, P01004 (2008)

[26] ATLAS Collaboration, *ATLAS muon spectrometer: Technical Design Report* (1997)

[27] G. Apollinari, et al., *High-Luminosity Large Hadron Collider (HL-LHC): Technical Design Report V. 0.1*, CERN Yellow Reports: Monographs, CERN, Geneva (2017)

[28] S. Ramo, *Currents Induced by Electron Motion*, Proceedings of the IRE **27(9)**, 584 (1939)

[29] W. Shockley, *Currents to Conductors Induced by a Moving Point Charge*, J. Appl. Phys. **9(10)**, 635 (1938)

[30] V. Mittal, S. Verma, R.C. ans Gupta, *Introduction to nuclear ans Particle Physics*, PHI Learning Pvt. Ltd. (2018)

[31] M. Kumakhov, F. Komarov, *Energy Loss and Ion Ranges in Solids*, Gordon and Breach Science Publishers (1981)

[32] L. Rossi, et al., *Pixel Detectors: From Fundamentals to Applications*, Particle Acceleration and Detection, Springer (2006)

[33] R. Mann, *An Introduction to Particle Physics and the Standard Model*, Taylor & Francis (2010)

[34] C. Sah, R. N. Noyce, W. Shockley, *Carrier Generation and Recombination in P-N Junctions and P-N Junction Characteristics*, Proceedings of the IRE **45(9)**, 1228 (1957)

[35] CMS Collaboration, *Measurement of the bulk leakage current of silicon sensors of the CMS preshower after an integrated luminosity of 6.17 fb^{-1}, at $\sqrt{s}$ = 7 TeV*, JINST **8**, P02004 (2013)

[36] M. Moll, *Radiation damage in silicon particle detectors: Microscopic defects and macroscopic properties*, Ph.D. thesis, Hamburg U. (1999)

[37] G. Lindström, *Radiation damage in silicon detectors*, Nucl. Phys. A **512(1)**, 30 (2003)

[38] R. Wunstorf, *Systematische Untersuchungen zur Strahlenresistenz von Silizium-Detektoren für die Verwendung in Hochenergiephysik-Experimenten*, Ph.D. thesis (1992), presented on Oct 1992

[39] G. Kramberger, et al., *Determination of effective trapping times for electrons and holes in irradiated silicon*, Nucl. Phys. A **476(3)**, 645 (2002), proc. of the 3rd Int. Conf. on Radiation Effects on Semiconductor Materials, Detectors and Devices

[40] G. Kramberger, et al., *Annealing studies of effective trapping times in silicon detectors*, Nucl. Phys. A **571(3)**, 608 (2007)

[41] G. Pellegrini, et al., *Technology developments and first measurements of Low Gain Avalanche Detectors (LGAD) for high energy physics applications*, Nucl. Instrum. Meth. A **765**, 12 (2014)

[42] H. F.-W. Sadrozinski, A. Seiden, N. Cartiglia, *4D tracking with ultra-fast silicon detectors*, Reports on Progress in Physics **81**, 026101 (2017)

[43] G. Kramberger, et al., *Radiation Hardness of Thin Low Gain Avalanche Detectors*, Nucl. Instrum. Meth. A **891** (2017)

[44] G. Kramberger, private communication

[45] G. Kramberger, et al., *Radiation hardness of thin Low Gain Avalanche Detectors*, Nucl. Instrum. Meth. A **891**, 68 (2018)

[46] G. Kramberger, *Solid State Detectors for High Radiation Environments*, Landolt Börnstein page 210 (2011)

[47] M. Moll, *Displacement Damage in Silicon Detectors for High Energy Physics*, IEEE Transactions on Nuclear Science **65(8)**, 1561 (2018)

[48] A. Chilingarov, *Temperature dependence of the current generated in Si bulk*, JINST **8(10)**, P10003 (2013)

[49] A. Ronzhin, *Silicon timing response to different laser light* (2017)

[50] S. Seidel, *Silicon strip and pixel detectors for particle physics experiments*, Physics Reports (2019)

Acknowledgements

I would like to thank Arnulf Quadt and Jörn Große-Knetter not only for their good and professional care, but also for taking over the opinions of my work.

Furthermore, I would like to thank Jörn Lange for the additional support, the many good advice and for the test reading of this work.
Likewise, my thanks go to Tobias, whom I have tormented with countless questions with more or less computer science regarding topics, but also the rest of the hardware subgroup. I'd also like to thank Tim and Helge for bonding my sensors, without whom this work would not have been possible.

Thanks to my parents, grandparents and siblings, who not only made it possible for me to study but also always supported me. Janne especially. Likewise, I could always count on the support, help and advice of my friend, Julian. I would like to thank Ricarda for reading my work and putting up with my insufferable spelling. Moreover, I thank all my other friends who have always been there for me and were always a huge help.

Erklärung nach §12(9) der Prüfungsordnung für den Bachelor-Studiengang Physik und den Master-Studiengang Physik an der Universität Göttingen:

Hiermit versichere ich, dass ich die vorliegende Abschlussarbeit selbstständig verfasst und keine anderen als die angegebenen Quellen und Hilfsmittel benutzt habe. Weiterhin versichere ich dass alle Ausführungen, die anderen Schriften wörtlich oder sinngemäß entnommen wurden, kenntlich gemacht sind und die Arbeit in gleicher oder ähnlicher Fassung noch nicht Bestandteil einer Studien- oder Prüfungsleistung war.

Die digitale Version stimmt mit der schriftlichen überein.

Göttingen, den 30. Januar 2020

(Marike Schwickardi)